| | |
|---|---|
| **Title** | 化学合成したI-III-IV-VI族四元化合物ナノ結晶を用いたナノ構造熱電材料の作製 |
| **Author(s)** | DWIVEDI, PRATIBHA |
| **Citation** | |
| **Issue Date** | 2020-09 |
| **Type** | Thesis or Dissertation |
| **Text version** | ETD |
| **URL** | http://hdl.handle.net/10119/17008 |
| **Rights** | |
| **Description** | Supervisor:前之園　信也，先端科学技術研究科，博士 |

# Nanostructured Thermoelectric Materials Fabricated from Chemically Synthesized I-III-IV-VI Quaternary Compound Nanocrystals

**by**

## PRATIBHA DWIVEDI

**Submitted to**

**Japan Advanced Institute of Science and Technology**

**In partial fulfillment of the requirements**

**For the degree of**

**Doctor of Philosophy**

***Supervisor*: Professor Dr. Shinya Maenosono**

***School of Materials Science***

***Japan Advanced Institute of Science and Technology***

**September 2020**

Referee-in-chief: **Professor Dr. Shinya Maenosono**
*Japan Advanced Institute of Science and Technology*

Referees: **Professor Dr. Mikio Koyano**
*Japan Advanced Institute of Science and Technology*

**Professor Dr. Hiroshi Mizuta**
*Japan Advanced Institute of Science and Technology*

**Associate Professor Dr. Toshiaki Taniike**
*Japan Advanced Institute of Science and Technology*

**Associate Professor Dr. Masashi Akabori**
*Japan Advanced Institute of Science and Technology*

**Professor Dr. Teruyuki Ikeda**
*Ibaraki University*

# Abstract

Thermoelectric (TE) technology has acquired a lot of attention due to the ever-growing demand for energy conversion. The research finding on TE materials is hot topic. However, majority of the high efficiency TE materials contains toxic and rare elements such as Se and Te that are not feasible for real application. To investigate the sustainable TE materials with high efficiency, quaternary copper-metal-tin-sulfide based compounds emerged as promising TE material was selected because it consists of environmental friendly, earth abundant and relatively low-cost elements. This dissertation surrounds on the research work of quaternary copper sulfide-based nanocrystals as building block for TE materials, synthesized by chemical methods. The nanobulk material fabrication approaches, characterizations and TE properties in combination with the methodology to improve the TE figure of merit are all presented in this research work.

Chapter 1 provides the general introduction of the TE materials. This chapter includes the basic concepts of TE's, conventional TE materials, synthesis, effective methodologies to enhance the thermoelectric efficiency, background about the quaternary copper-sulfide based material and its potential as well as challenges for being selected as TE materials. In this research we decided to counter the high lattice thermal conductivity ($\kappa_{\mathrm{lat}}$) through not only all-scale hierarchical architechuring but also introducing the copper-aluminium-tin-sulfide based material for the first time in thermoelectrics due to predictions of these system to possess very low $\kappa_{\mathrm{lat}}$. High power factor (*PF*) and low $\kappa_{\mathrm{lat}}$ was not sufficient for $Cu_3AlSnS_5$ (CATS) system to acquire high *ZT* value. The shortcomings of the CATS system were systematically countered with the gradual substitution of Al by Ga, and by introducing nanoinclusions of $Cu_2SnS_3$ (CTS). We are the first to investigate the $I_3$-II/III-IV-$VI_{5-y}$ (I=Cu; II=Zn; III=Al/Ga; IV=Sn; VI=S; $y$ is to maintain electrical neutrality of the system) based TE materials. Various methodologies available for the nanocrystals synthesis have been discussed and out of all the one pot chemical method was shortlisted for this research due to their unprecedented control on the reaction reproducibility as well as scalability. In other words, this chapter represents the challenges associated with present TE materials have been postulated in combination with a brief outlook about the scope of this research, as one of the plausible solutions.

Chapter 2 describes the synthesis of Cu-Zn-Sn-S nanocrystals using one pot chemical method. After ligand exchange, the nanocrystals were pelletized using pulse electric current sintering (PECS) technique to yield $Cu_3ZnSnS_{5-y}$ nanobulk material. To lower the $\kappa_{\mathrm{lat}}$, a gradual substitution of Zn with Al was performed in the $Cu_3ZnSnS_{5-y}$ system to yield $Cu_3Zn_{1-x}Al_xSnS_{5-y}$ ($x$ = 0.25, 0.5, 0.75, and 1). Complete substitution of Zn by Al substantially decreased the $\kappa_{\mathrm{lat}}$ and dramatically increased $\sigma$ of the material. *ZT* value of 0.39 at 658 K was achieved for the $Cu_3ZnSnS_{5-y}$ material. However, the *ZT* value could not be significantly enhanced with complete Al substitution, which could be primarily attributed to the $\kappa_{\mathrm{car}}$. These results highlight the production of $Cu_3Zn_{1-x}Al_xSnS_{5-y}$ TE materials and unveil the scope for improvement of $ZT$ values by altering transport properties.

The Chapter 3 demonstrate a methodology for curtailing the $\kappa_{\mathrm{car}}$ of the CATS nanobulk TE materials without compromising the already suppressed $\kappa_{\mathrm{lat}}$. This chapter presents the effect of Ga substitution in $Cu_3Al_{1-x}Ga_xSnS_5$ nanobulk materials on the transport properties of the materials has been systematically examined. The $ZT$ value of the $Cu_3Al_{1-x}Ga_xSnS_5$ nanobulk at $x = 0.5$ was found to be more than twice ($ZT = 0.26$) than the pristine CATS nanobulk at 665 K, primarily because of the significant reduction in $\kappa_{\mathrm{car}}$. Correlation among transport parameters and material structural characteristics of the $Cu_3Al_{1-x}Ga_xSnS_5$ nanobulks ($0.25 \leq x \leq 1$) revealed that a larger fraction of zincblende (ZB) phase leads to a higher $PF$.

The Chapter 4 examines the ability of CTS nanocrystals as nanoinclusions in the CATS system for reducing the $\kappa_{\mathrm{car}}$ without negatively impacting the $\kappa_{\mathrm{lat}}$. The doping content of CTS gradually varied from 0.1 wt%, 1 wt%, 3 wt%, 5 wt% and 10 wt% in CATS. The fabricated nanobulk TE material shows, interestingly, wurtzite (WZ) as a major crystalline phase from 1 wt% CTS content onwards; which increases with the increase in CTS nanoinclusions. A correlation has been observed between the type and content of major crystallographic phase and the thermoelectric performance of the fabricated nanobulk TE materials. Greater content of WZ phase has been associated with the lower $ZT$ value. The results direct the attention towards the role of interface between the nanoinclusion and primary matrix in deciding the fate of, especially, $\sigma$. The 0.1 wt% CTS nanoinclusions leads provided better trade-off between $\sigma$ and $S$ without compromising $\kappa$ and thus improved the $ZT$ value 3× than neat CATS system. The 0.1 wt% CTS containing sample possess greater ZB phase content than any other pellets under consideration and prevail the importance of symmetric crystal structure content in deciding the fate of TE properties.

Chapter 5 disseminates the general summary and conclusions followed by the future prospects of the research presented in this dissertation. The results highlight the importance of co-ordination between the material crystalline structural traits and $ZT$ value of $I_3$-III-IV-$VI_5$ based TE materials without using rare and/or highly toxic elements. This research provides an important insight in understanding the behavior of ZB-/WZ-rich nanobulk TE materials. The correlation observed among material structural traits that apart from nanostructuring, the greater content of more-ordered crystalline phase plays an important in regulating the transport characteristics. On the other hand, the mechanistic details for understanding the reasons which affects inherently the content and the distribution of ZB/WZ phase fraction in the material in association with their respective electrical and thermal transport properties represents a challenging yet interesting future outlook.

**Keywords**: Thermoelectric, Quaternary Copper Sulfides, Crystallographic Phases, One Pot Chemical Synthesis, Nanocrystals

# Table of Contents

# Acknowledgements

It is a pleasure to convey my gratitude to all who contributed in the successful completion of this dissertation in my humble acknowledgment.

Firstly, I would like to show my sincere gratitude to my supervisor Professor Shinya Maenosono for accepting me in the doctoral course in his laboratory and his recommendation for the MEXT scholarship. I would like to thank him for providing several opportunities to present my research work at various platforms, domestic as well as in international conferences. It has been a learning experience and happy to extract the best out of my tenure to achieve all the objectives.

I would like to express my gratitude to Professor Kazuaki Matsumura as my second supervisor. He has been always kind to me and has motivated me for pursuing my research proposal through his approvals with short yet nice conversations.

My heartiest thanks to Professor Mikio Koyano as a minor research supervisor and allowing me to pursue my minor research project at the Cardiff University. He has always motivated me to pursue my research ideas-detailed out in the proposal. He has asked several time quite intriguing questions and inspired me to learn more about thermoelectric materials. I am grateful for his support in using the PPMS machine for experiments. I would like to express my gratitude to the Assistant Professor Masanobu Miyata for his help in the Hall measurements for my samples. I appreciate his kind guidance in analyzing the Hall measurements data and explaining the physics behind the experimental observations. He has also contributed greatly in enriching my knowledge about thermoelectric materials.

I would like to express my deep gratitude to Mr. Takeo Akatsuka, Mr. Hiroshi Takida and Mr. Korefumi Kubota from Nippon Shokubai for their tremendous help in operating the machine to make pellets using pulsed electric current sintering (PECS) technique. I would like to thank Dr. Michihiro Ohta from AIST for the consistent support in operating the machine for thermoelectric properties measurements of my samples. I also express my gratitude to Dr. Koichi Higashimine from the Center for Nano Materials and Technology of JAIST for his prompt help in the observation of STEM-HAADF images of my samples reported in this dissertation.

I want to thank last but not the least, our former and current lab members for providing a memorable experience at JAIST, which includes, Mr. Yujin Wang, Mr. Takeshi Nakada, Mr. Masahito Hatsukano, Dr. Wei Zhou, Mrs. Chiko Shijimaya, Mr. Shujie Fei, Mr. Ryoichi Kitaura, Dr. Maninder Singh, Dr. Priyank Mohan, Ms. Annelies Mannak, Assistant Professor Dr. Mari Takahashi, Mr. Kimihiro Numano, Mr. The Son, Mr. Junpeng Liu and Ms. He Sizun.

Finally, I want to say many thanks to my brother Dr. Sumant Dwivedi for his invaluable timely guidance and all the family members for their continuous support and endless affection for me. Thank you for all for your understanding and support during this challenging phase of my life.

**Pratibha Dwivedi**

# Chapter 1

## General Introduction

## 1.1 Background of Thermoelectrics

Importance of fire has been realized from the very early stages of the mankind history and in civilization development efficient use of fire (or heat) plays an important role. However, in the late nineteenth century that the nature of heat was understood; thanks to the first law of the thermodynamics, it is known that the heat is a form of energy, and follows the energy conservation law.[1] Temperature is an intensive variable for heat energy, while the entropy exists as the corresponding extensive variable. Except for reversible processes, such as the Carnot cycle, entropy will continue to increase, representing that the heat energy cannot be completely converted into work. This is known as the second law of thermodynamics.[1]

According to the second law of thermodynamics, the more the work done, the more the heat increases. With the recent developments in electronic or semiconductor technology, many electronic devices have been produced, complied, and used to perform numerous tasks, which finally generate an enormous amount of unusable heat.[2] Thus, heat management has become a serious subject these days and necessitates deep understanding of the thermal conduction process in solids. Thermal conduction is a predominant process of heat flow in solids, when compared with radiation and convection and is facilitated by conduction electrons in combination with the lattice vibrations (phonons).[3] It is known that electrons can carry electrical current as well, so that there exists a finite coupling between the thermal current and the electrical current. These are known as the thermoelectric (TE) phenomena.[4] By making full use of the TE phenomena in semiconductors, it is feasible to convert electric power into heat, and vice versa. Such a technology is called thermoelectrics. Thermoelectrics yields direct conversion between heat and electricity and vice versa. This technology enables the shortest conversion route between the two forms of energy and eliminate the need for a working gas, turbine and alternator used in traditional electricity generation or a compressor in traditional cooling.[5] In this system, devices without any moving parts can be constructed which provides superior reliability as well as silent operation and without any considerable maintenance.

The Seebeck effect is the first reported physical effect of direct conversion of TE energy, founded by German scientist Thomas Johann Seebeck in 1821.[6] In his experiment, two different metal wires were connected end to end to form a loop, when one of the junction is heated and the other was kept cold as shown in Figure 1.1 (a), a magnetic field generated around the loop. Thereafter, in 1823, Hans Christian Oersted provided the physical interpretation.[7] The observed phenomenon was ascribed to the temperature gradient which creates a potential difference between the junctions of different materials lead to generate a circuit current that causes a magnetic field around the wire. Thus, the concept of thermoelectricity is proposed. Thomas Johann Seebeck was the first person to well-document this phenomenon observed through experiments and therefore named as the Seebeck effect.

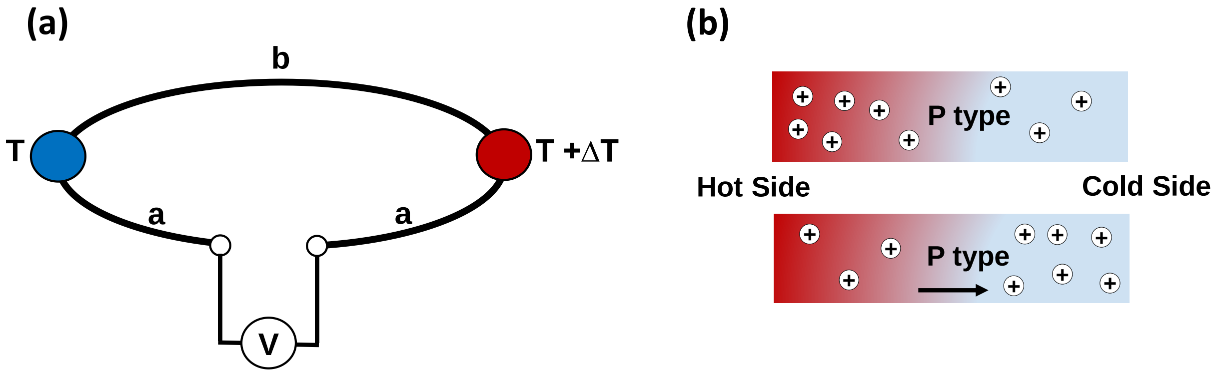

**Figure 1.1.** (a) Schematic basic thermocouple; (b) Illustration for explaining the Seebeck effect principle.

The potential difference can be expressed in the equation 1.1 as following:

$$S = \frac{\Delta V}{\Delta T} \tag{1.1}$$

Where $S$ is Seebeck coefficient (V/K), $\Delta V$ is potential difference (V), $\Delta T$ is temperature gradient (K). The principle can be explained by the illustration as shown in Figure 1.1 (b).

In 1834, France scientist Jean-Charles-Athanase Peltier discovered the reverse process of the Seebeck effect and named as Peliter effect. Peltier effect was observed when an electric current flow produced in a loop connecting two different conductors, one junction became hot and another become cold.[8] With the progression of time, in 1854, William Thomson, also called Lord Kelvin related these two important effects by thermodynamics theory and predicted another effect which had been proved by experiment in 1867, known as Thomson effect.[9] The behavior of a TE circuit is dependent on the Seebeck, Peltier, and Thomson coefficients. An understanding of these thermodynamic phenomena allows for the discovery and development of different materials systems that possess good TE properties as well as increases the potential for technological applications.

A TE converter is a heat engine and like all heat engine obeys the law of thermodynamics. In 1911, Edmund Altenkirc analyzed the TE energy conversion efficiency and contributed a theory to calculate it by considering the simplest TE generator (Figure 1.2) consisting of a single thermocouple with thermoelements fabricated from *n*-type and *p*-type semiconductors as shown in the Figure 1.2.[10] The efficiency of the TE generator is given by following equation:

$$\eta = \frac{Energy\ supplied\ to\ load}{Heat\ absorbed\ at\ hot\ junction} \tag{1.2}$$

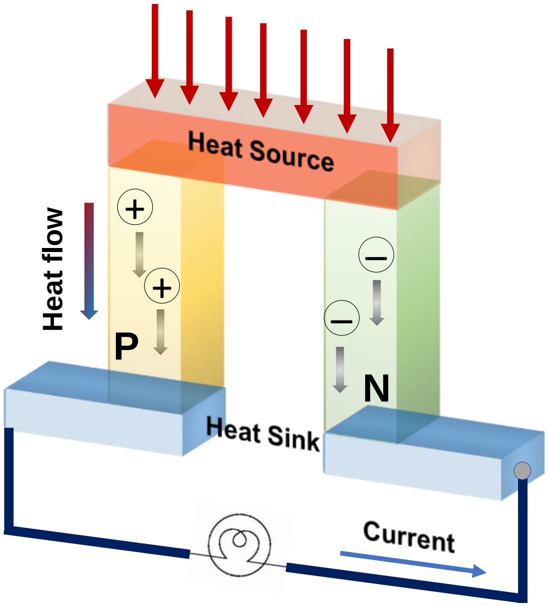

**Figure 1.2.** TE generator designed on the Seebeck effect.

Furthermore, he pointed out that a high TE conversion efficiency should improve the absolute *S* and electrical conductivity and meanwhile should possess low the thermal conductivity. Based on these characteristics, Abram Fedorovich Ioffe quantified the expression explicitly and defined the maximum efficiency ($\eta_{\max}$) of the TE generator through following equation as a product of Carnot efficiency, which is certainly less than unity.[11]

$$\eta_{\max} = \frac{T_{\mathrm{H}} - T_{\mathrm{C}}}{T_{\mathrm{H}}} \times \frac{\sqrt{1 + Z\bar{T}} - 1}{\sqrt{1 + Z\bar{T}} + \frac{T_{\mathrm{C}}}{T_{\mathrm{H}}}} \tag{1.3}$$

$T_{\mathrm{H}}$ and $T_{\mathrm{C}}$ represent the temperature of hot and cold junction respectively.

$$\bar{T} = \frac{T_{\mathrm{H}} + T_{\mathrm{C}}}{2} \tag{1.4}$$

The figure-of-merit ($ZT$) can be written as follows[11]:

$$ZT = \frac{S^2\sigma}{\kappa}T \tag{1.5}$$

where $\sigma$ is the electrical conductivity ($\mathrm{S\cdot m^{-1}}$); $T$ is the temperature (K); $\kappa$ is the thermal conductivity ($\mathrm{W\cdot m^{-1}\cdot K^{-1}}$). The dimensionless $ZT$ value is an important parameter for judging a TE material. Higher the $ZT$ value better is the TE material. For a long time, researches on TE materials have focused on methodologies to improve $ZT$ value of materials. A high performance TE material should have high power factor ($PF = S^2\sigma$) and low $\kappa$. However, $S$, $\sigma$ and $\kappa$ are interrelated to each other in a reverse manner.

The Seebeck coefficient can be expressed for metals and highly degenerate semiconductors,[12] using simple transport model can be written as follows:

$$S = \frac{8\pi^2 {k_\mathrm{B}}^2}{3eh^2} m^* T \left(\frac{\pi}{3p}\right)^{\frac{2}{3}} \tag{1.6}$$

Where $k_\mathrm{B}$, $e$, $m^*$, $h$ and $p$ are Boltzmann constant, elementary charge, effective mass of the carrier, Planck’s constant and carrier concentration, respectively.

Using the Boltzmann transport theory[13], the following general expression has been derived for electrical conductivity $\sigma$ (or resistivity ($\rho$))

$$\frac{1}{\rho} = \sigma = pe\mu \tag{1.7}$$

Where, $\mu$ is the charge carrier mobility and can be written as:

$$\mu = \frac{e\tau}{m^*} \tag{1.8}$$

Here $\tau$ is the average time between collisions or relaxation time.

In metals, which have a partially filled conduction band, $p$ does not vary much with temperature.[14] However, $\tau$ decreases with the increase in temperature, mostly as $T^{-1}$, due to the more frequent electron-phonon collisions. Overall, $\sigma$ of metals decreases with increasing temperature. In semiconductors, increasing temperature excites carriers into the conduction band where their population $p$ increases exponentially.[14] This increase dominates the temperature dependence of $\sigma$ which increases exponentially with temperature. This picture is generally valid but in reality, the temperature dependence of all the factors is extremely complex and depends on a myriad of aspects.

Thermal conduction is a process which involves the exchange of thermal energy by means of excitations on the atomic scale.[15] Conduction, described by the physical quantity thermal conductivity $\kappa$, is by far the most important mechanism in solids and we will therefore describe it in detail. Thermal conduction may be further split into different contributions based on which excitations take part in the heat transport: $\kappa_{\mathrm{lat}}$ for phonons (lattice waves) and $\kappa_{\mathrm{car}}$ for charge carriers.[16] The net expression for the $\kappa$ can be written as follows:

$$\kappa = \kappa_{\mathrm{lat}} + \kappa_{\mathrm{car}} \tag{1.9}$$

From the kinetic theory we may obtain the following equation for lattice thermal conductivity ($\kappa_{\mathrm{lat}}$)[17]:

$$\kappa_{\mathrm{lat}} = \frac{1}{3} C_{\mathrm{v}} v l \tag{1.10}$$

where $C_{\mathrm{v}}$ is the volumetric heat capacity associated with the excitation, $v$ is the velocity with which it propagates, and $l$ is its mean free path.

At high temperatures, the dominant scattering mechanism are phonon-phonon interactions in the so-called Umklapp process which occurs when the resulting wave vector of two colliding phonons exceeds the first Brillouin zone, effectively reflecting the resulting phonon.[18] On the contrary, at low temperatures, the phonon wave vectors are not large enough for Umklapp processes to occur and obstruct the heat flow. The magnitude of phonon-phonon scattering is depended on the grain size and increases with the decrease in grain size.[19] The temperature dependence of $\kappa_{\text{lat}}$ mostly mimics the heat capacity, which follows the $T^3$ law.[20]

In the development of TE materials, one of the first approaches include minimization of heat transport by identifying materials with crystal structures yielding intrinsically low $\kappa_{\text{lat}}$. To further reduce $\kappa_{\text{lat}}$, additional point defects acquaints with the fluctuations in mass, size and interatomic coupling forces and can be created through alloying, partial atomic substitution or the addition of elements in proper lattice sites, such as filling structural voids with ‘‘rattling’’ atoms.[21]

The second contribution to thermal conductivity is the electronic part $\kappa_{\text{car}}$. Unlike the lattice part, $\kappa_{\text{car}}$ only contributes when the material conducts electricity. It is the main mechanism of heat transfer in metals and plays a very critical role in optimizing TE properties of materials.

$$\kappa_{\text{car}} = \frac{\pi^2}{3}\left(\frac{k_{\mathbf{B}}}{e}\right)^2 \sigma T = L\sigma T \tag{1.11}$$

The above expression is known as the Wiedemann-Franz law which links the electronic part of thermal conductivity $\kappa_{\text{car}}$ and the electrical conductivity $\sigma$ via the absolute temperature and the Lorenz number ($L$). Its value for free electrons system is $L = 2.44 \times 10^{-8}$ W·Ω·K$^{-2}$.[22]

From the view point of model TE materials to effectively combat the $\kappa$ is known as phonon glass and an electron crystal, or “PGEC”, a concept introduced by Slack in 1990.[23] In PGEC system, the TE material needs to act as a crystal, with respect to electrons, and as a glass, with respect to phonons, simultaneously. Some “clathrate” and “skutterudite” compounds do behave similar to PGEC concept but certainly cannot be classified as PGEC materials.[24] In most cases of the materials behaving like PGEC, many factors has been ascribed apart from material's crystallinity in the reduction of the $\kappa$.

## 1.2 Methodologies for Improving *ZT* value

The methodologies to modulate the *ZT* values lies in the efforts to tune the materials transport and structural features. Several techniques have been considered as modern concepts to enhance the TE material performance. Nanostructuring and all scale hierarchical architecturing has been evolved with time as one of the most successful strategy to effectively mitigate the $\kappa_{\mathrm{lat}}$, as shown with illustration in Figure 1.3 (a) and (b).[25]

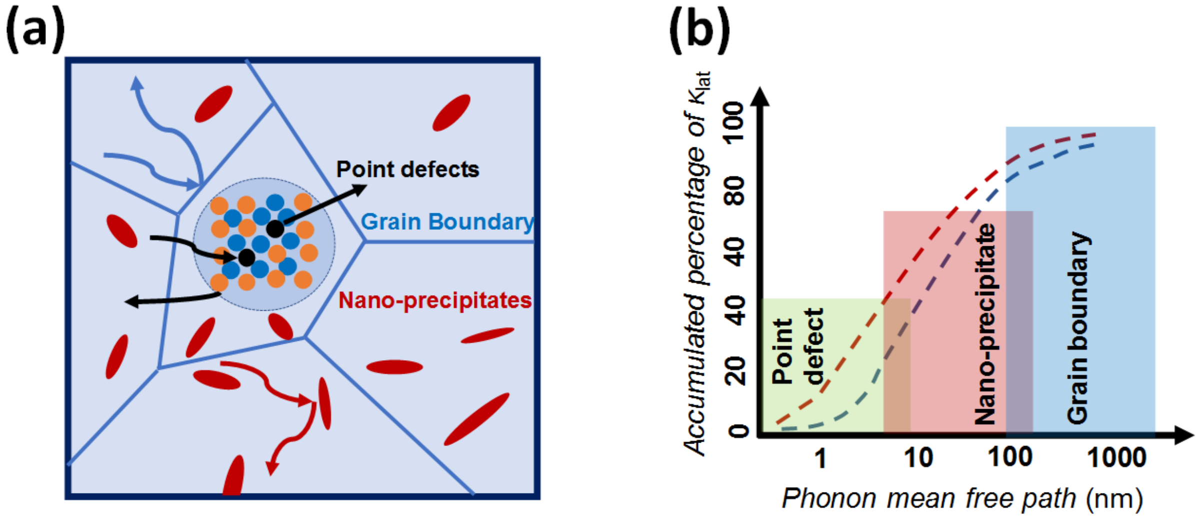

**Figure 1.3.** (a) Diagram schematically describes all-scale hierarchical architecture to scatter phonon; (b) accumulated contributions to reduce lattice thermal conductivity with respect of phonon mean free path in PbTe.[27]

There are two kinds of nanostructured TE materials. The first type consists of a single phase and it is defined by an assembly of nanosized particles or grains.[26] The second type is a system comprising a major bulk phase containing a minor second phase embedded in the matrix. The second phase is existing in the nanoscale dimensions, while the matrix could possess multi-level dimensionality.[25] However, the phonon propagation within the second phase is rather unpredictable, making it challenging to design a proper system and needs a lot of optimization experimentations. An array of investigations, both experimentally as well as theoretical, have been conducted to establish the large reduction in the $\kappa_{\mathrm{lat}}$ in bulk nanostructured materials as a methodology to improve the $ZT$ value. An exemplary example for nanostructuring has been introduced through PbX (X = S, Se and Te) based chalcogenides materials has been successfully tested for enhancing the $ZT$ value.[27-30] Our research group has acquired expertise in nanostructuring and all-scale hierarchical architechturing synthetic methodologies and have been proven in a range of Cu-S based chalcogenide/chalcopyrite TE materials.[31-35]

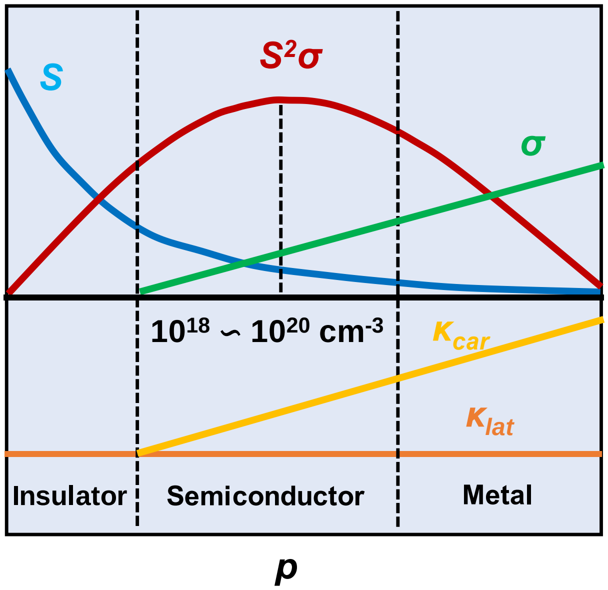

**Figure 1.4.** Interdependence of $S$, $\sigma$, $\kappa_{\mathrm{lat}}$ and $\kappa_{\mathrm{car}}$ on $p$.

Beyond nanostructuring, the elemental substitution, doping and playing around complex crystal structuring keeps on igniting minds as a methodology to enhance TE transport properties. The doping/elemental substitution are known to affect primarily either-or combination of the $p$, $\mu$, $m^*$ which ultimately contributes towards the $S$ or $PF$ resurgence.[36-38] It was pointed out that most of the TE materials are heavily doped semiconductors exist with optimal carrier concentration in the range of $10^{18}$-$10^{20}$ cm$^{-3}$, as shown in the Figure 1.4.[11] The $p$ can be tuned by introducing electronically active extrinsic impurities, adjusting the material stoichiometry and/or exploiting the intrinsic defect chemistry of the material. Such compositional and defect adjustment can be performed during synthesis or through post-synthesis processes.[39,40] Moreover, electronically active additives can be introduced through compounds with suitable electronic band alignment, either by blending or using heterostructures containing both materials.[39] A range of examples exist to exemplify the success of doping or bulk elemental substitution in TE materials performance. For instance, Duann *et al*. carried out experiments to optimize the electrical and thermal transport properties of the $Bi_2Te_{2.7}Se_{0.3}$ by Ga-doping and improved the $ZT$ value by over 25% to reach 0.82 at 400 K.[41] While, Kim et al. studied the effect of Pb, Ag, and Cu doping on the TE properties of p-type $Bi_{0.52}Sb_{1.48}Te_3$. It was found that the concentration of holes, as majority charge carriers, could be precisely changed by controlling doping of Pb, Ag, and Cu in a low temperature range leading to the enhancement of $ZT$ value, close to unity, in the temperature range of 300-400 K.[42] The effect of doping is prevalent at higher temperatures as well. For instance, Wu *et al*. doped 3% of Na in $(PbTe)_{0.8}(PbS)_{0.2}$ and enhanced $ZT$ value to record value of 2.3 at 923 K.[43] Duann *et al*. showed that the oxidation state, atom size and electronegativity plays an important role in deciding the fate of $p$, $m^*$ and density of states in the resulting material. Moreover, alloying with atoms of similar electric potentials but with different masses can scatter phonons effectively, where scattering is due to difference in mass and/or bond stiffness. The greater mass difference contributes significantly in the $\kappa_{\text{lat}}$ reduction.[41] Furthermore, the complex crystal structuring is known to curtail the $\kappa$ as well as for modulating band-gap engineering.[17,44] For instance, the point defects resulted in crystal lattice through single doping or cross substitution delays the phonon propagation through effect scattering by crystal structure mismatch between host/dopant.[45] Crystal structure brings a lot of complexity in TE materials properties understanding and needs to be investigated in a systematic manner.

## 1.3 Typical Materials for Thermoelectric Applications

According to the optimal working temperature, TE materials can be broadly divided into three ranges < 400 K, 400 K-900 K and > 900 K. The most widely used TE materials, in order of increasing operating temperature, are bismuth telluride ($Bi_2Te_3$); lead telluride (PbTe); and silicon germanium (SiGe)-based TE materials.[46-48] The retrospect analysis of temperature range most relevant to TE materials history, it was found that the low- and middle- temperature range are the most explored and has maximum potential for waste heat utilization.[49,50] Despite the fact that a lot of high-performance TE materials includes $Bi_2Te_3$ and PbTe based materials but the development trajectory of the TE materials exhibits a trend of pursuing low-cost and earth-abundant constituents for material for crediting technology sustainability.[39,51] Let's have a brief overview for representative state-of-the-art TE materials from low-, middle- and, high-temperature ranges along with their challenges and opportunities as follows:

### *1.3.1 State-of-the-art Thermoelectric Materials and Their Challenges*

The (waste) heat available from the room temperature to 473 K can be best utilized with $Bi_2Te_3$-based materials, discovered seven-decades ago and have been commercialized as well.[46] In terms of material's performance, *ZT* values for $Bi_2Te_3$ have been improved from unity to over twice using the super lattices and quantum dots.[52,53] Excellent performance does represent $Bi_2Te_3$-based TE materials as undaunted but to widen the applications temperature range has stimulated the materials scientist and began an era of renaissance of new TE materials exploration.

In 1950's PbTe has been recognized as a very promising compound for power generation in intermediate-temperature range.[54-56] PbTe possesses several outstanding features that are typical requirements for TE's, such as high $S$ due to its complicated electronic band structures, superior $\sigma$ from high-symmetry cubic crystal structure in combination with the low thermal conductivity caused by strong anharmonicity due to the Pb.[55,57,58] In 1960s, due to the technological limits, the $\kappa$ of PbTe was overestimated, thus the maximum *ZT* values underestimated and recorded ~0.7–0.8.[59,60] After laser flash method was provided to determine thermal diffusivity, the *ZT* values in both n-type PbTe were recognized to be as high as ∼1.4.[30] To obtain *p*-type PbTe, alkali metal in group-IA (Na, K) used as an acceptor dopant in Pb site and produce hole carrier ($p = 3\text{–}40 \times 10^{19}\ \text{cm}^{-3}$).[61,62] In *n*-type PbTe, elements such as I and Cl (doping on Te site), Sb, Bi, Al, Ga, and In (doping on Pb sites) are usually chosen as donor dopants, and the electron carrier density in superior *n*-type PbTe is in the range of $4\text{–}40 \times 10^{18}\ \text{cm}^{-3}$.[63-65] The *ZT* values of *p*-type PbTe-based materials boosted from ~1.0 to ~2.5, and the *ZT* values in *n*-type PbTe reach ~1.8-2.2.[66]

The quest of TE materials for very high temperature applications (over 1000 °C) converged in 1960's on SiGe alloy. Neither Si nor Ge is a good TE material, as their $\kappa_{lat}$ is very large (150 $W \cdot m^{-1} \cdot K^{-1}$ for Si and 63 $W \cdot m^{-1} \cdot K^{-1}$ for Ge).[67,68] The $\kappa_{lat}$ can be substantially reduced by alloy formation between the two elements due to the increased phonon–phonon and phonon–electron scattering.[69] Bulk $Si_{80}Ge_{20}$ acquired $ZT$ values of 0.5 with $\kappa$ less than 10 $W \cdot m^{-1} \cdot K^{-1}$.[48] A 40% $PF$ enhancement in $Si_{80}Ge_{20}$ bulk nanocomposites has been reported, attributed to the enhanced phonon-phonon and phonon-electron scattering resulting $ZT$ values as high as 1.3 for *n*-type and 0.95 for *p*-type modules have been measured.[70-72] SiGe devices can operate at temperatures up to 1300 K without significant degradation. The high TE efficiency in SiGe alloy can be controlled with precise doping with phosphorous (*n*-type) or boron (*p*-type).[48] Despite excellent TE performance, the high cost Ge discourages practical applications.

$V_2$-$VI_3$ compounds (based mainly on $Bi_2Te_3$), IV-VI compounds (based on PbTe) have been exploited widely. Despite of their outstanding TE performance, their applicability is limited due to multiple reasons, such as constituting toxic, rare and expensive elements; challenging processing and so on. For an instance, without a doubt, a lot of high-performance TE materials consists Te but the earth-crust abundance of Te is just one-fourth of Au, which is a rare precious element.[73] Therefore, the dwindling limited reserves of these expensive elements accompanying environment hazards hinders the large-scale use of these materials in TE generators; and thereby levitates the trajectory towards the development of relatively earth abundant, less toxic elements containing TE materials.

### 1.3.2 Copper-Sulfide Based Thermoelectric Materials

Materials scientists are constantly exploring an extensive range of cost effective and eco-friendly TE materials which can be synthesized in bulk form. As discussed earlier, over third of waste heat is wasted in the middle-range temperature ranges (~400 °C), same as for $Bi_2Te_3$ and PbTe-based TE materials. One of the strong TE material candidate includes copper based chalcogenides (S, Se, Te) *i.e.* binary superionic conductors (such as $Cu_2Se$, $Cu_2S$, $Cu_2Se_{0.7}Te_{0.3}$), ternary ($Cu_2SnSe_3$, $Cu_2SnS_3$ etc.) and quaternary semiconductors ($Cu_2ZnSnSe_4$, $Cu_2ZnSnS_4$ (CZTS)) which consist of relatively non-toxic, eco-friendly as well as earth-crust ubiquitous elements.[34,39,74-78] Compared to the traditional telluride-based TE materials, the elements in the composition of $Cu_2ZnSnS_4$ are in very high abundance-the natural reserves of copper, zinc, tin are 630, 250, and 5.2 million tons, on the other hand, the natural reserves for tellurium are only 0.022 million tons.[73] In last decade, close attention has been paid on the investigation of TE properties of typically wide band gap copper zinc tin sulfur/selenide (CZTS/Se) materials due to their complex crystal structure. Due to their complex structure, the $\kappa$ of quaternary-copper-chalcogenides are much less (from 2.95 $W{\cdot}m^{-1}{\cdot}K^{-1}$ at 300 K to 0.97 $W{\cdot}m^{-1}{\cdot}K^{-1}$ at 700 K) compared to many other conventional TE materials.[79] $Cu_2ZnSnS_4$ is an interesting TE material and holds low $\kappa$, fairly good $S$ but fairly low $\sigma$. The reported $ZT$ values for undoped $Cu_2ZnSnS_4$ remain quite low, ranging from $4.6 \times 10^{-5}$ at 300 K to 0.026 at 700 K.[79] In an attempt to improve the $\sigma$ for enhancing the $PF$, the Cu-doped $Cu_2ZnSnS_4$ synthesized by one-pot method resulted $Cu_{2.19}Zn_{0.80}Sn_{0.75}S_{3.53}$ possessing $ZT$ value of 0.14 at 700 K.[79] Wei *et al*. reported the Cu-Sn-S doped with Zn to result $Cu_2Sn_{0.85}Zn_{0.15}S_3$ exhibited the highest $ZT$ value (0.37 at 670 K).[80] Instigating the empirical developments for enhancing the $ZT$ value within the Cu-S based I-II-IV-VI materials, Suekuni and co-workers reported that $Cu_{26}V_2Ge_6S_{32}$ (colusite) had a $ZT$ value of 0.73 at 663 K.[81] By this time, several Cu-S TE materials exceeded the *ZT* value of unity, which includes $Cu_{11}MnSb_4S_{13}$ tetrahedrite (*ZT* = 1.13 at 575 K), $Cu_{10.5}Ni_{1.0}Zn_{0.5}Sb_4S_{13}$ tetrahedrite (*ZT* = 1.03 at 575 K), and $Cu_{26}Ta_2Sn_{5.5}S_{32}$ colusite (*ZT* ~1 at 670 K), had been reported from different groups.[82-84] Besides this, several groups began exploring Cu-S based quaternary compounds composed with doping with transition metal or group IIIA element. Shen *et al.* have systematically studied the Zn-doped CTS as TE materials, synthesized by direct reaction at high temperature followed by spark plasma sintering (SPS) at 773 K. As a result, $Cu_2Sn_{0.9}Zn_{0.1}S_3$ exhibited *ZT* = 0.58 at 723 K.[85] Tan *et al.* studied In-doped CTS bulk materials were prepared by the mechanical alloying combined with SPS to result $Cu_2Sn_{0.9}In_{0.1}S_3$, displayed *ZT* value 0.56 at 773 K.[86] Zhao *et al.* also studied the Co-doped CTS, which synthesized by direct reaction at high temperature followed by SPS. The sample of $Cu_2Sn_{0.8}Co_{0.2}S_3$ showed *ZT* = 0.85 at 723 K.[87] The same group also reported a *ZT* of ~0.75 has been achieved in the Fe doped sample $Cu_2Sn_{0.85}Fe_{0.15}S_3$ at 723 K.[88] Xu *et al.* reported a relatively high *ZT* up to 0.56 in the $Cu_2Sn_{0.9}Ni_{0.1}S_3$ sample at 723 K.[89] Zhang *et al.* investigated the Mn doped CTS, a high *ZT* ~0.68 at 723 K was obtained.[90] Development in the nanostructuring realized the *ZT* value enhancement from 0.37 to 0.64 at 670 K, through blending of $Cu_2Sn_{1-x}Zn_xS_3$ compounds possessing varying level of Zn/Sn content.[91] These studies have contributed tremendously towards improving the *ZT* value, but the approach has turned out to be largely hit-and-trial and acquired saturation in the further development. In other words, overexploitation of the existing system challenges the new possibilities of TE material’s development and thereby demands synthesis of newer system without compromising the material sustainability features.

Recently, Li *et al*. using *ab-initio* calculation predicted Cu-M-Sn-S (M = group IIIA element; or I-III-IV-VI) as a potential TE material with substantially low $\kappa_{\mathrm{lat}}$ and high *PF*.[92] Notably, wurtzite (WZ) $Cu_3InSnS_5$ (CITS) nanocrystals, which belong to the $I_3$-III-IV-$VI_5$ family (a new generation of copper-based quaternary semiconductor), have been synthesized by Pan and co-workers for solar cell applications.[93] However, for the CITS, the scarcity of indium greatly restricts the development and application of this group of $I_3$-III-IV-$VI_5$ as prospective TE materials. To lower the cost and develop new compounds within the group of $I_3$-III-IV-$VI_5$, Al has been utilized instead of In and the resulting $Cu_3AlSnS_5$ (CATS) nanocrystals were evaluated for photoresponsive properties.[94] This new class of quaternary compounds represents an opportunity to understand their TE behavior. In current research, in order to investigate potential TE materials derived from relatively earth-abundant and less toxic elements; CATS system has been selected as the base material for the study. Through nanostructuring, substitution and doping strategies in CATS system the material's transport properties and subsequently TE performance have been investigated. There are several transition metals exhibiting +3 oxidation state and have not been considered as an alternative to IIIA element due to the magnetic characters (*e.g.* Fe)[88] and multivalent states of transition metals, which can exhibit inadvertent effects on transition metals and restricts/complicates the inferences.

## 1.4 Thermoelectric Materials Synthesis

Without any doubt, nanostructuring is one of the integral requirements for the development of high-performance TE materials. TE nanoparticles can be produced by several processes, which can be broadly rationalized as top-down or mechanical, and bottom-up methods. Top-down approaches produce nanoparticles by disintegration of extended solids, harnessing the compositional (including doping) and structural engineering of starting bulk materials.[95, 96] Particularly, grinding is one of the most prevalent and industrialized nanoparticle production technologies due to its moderate cost, simplicity and versatility. As drawbacks, top-down methods are energy-intense and possess lack of precise control over the nanoparticle size, shape and thereby subsequent material transport properties.

The bottom-up method is widely used to construct desired structure and involves the assembly of atoms or molecules into nanostructured arrays due to attractive forces.[97] The bottom-up processes encompass chemical synthesis, producing a controlled deposition and materials growth. The associated chemical synthesis can be achieved through reactions between the solid, liquid and/or gaseous reactants. There are several kinds of chemical methods to synthesize the nanoparticles such as solvothermal, hot-injection and one-pot synthesis methodology.[97-100] The TE measurement demands a large amount of sample to be pelletized and therefore the technique employed should be able to yield nanoparticles in large amount with excellent reproducibility. Out of these synthesis techniques, the one-pot synthesis represents an appropriate option for the large-scale nanoparticle synthesis. In the one-pot synthesis, a solution of precursors in a flask are subjected to the thermal decomposition leading to the reaction between the constituents, controlled by diffusion, followed by nucleation and growth yielding nanoparticles.[100] Reaction temperature, ratio between the reactants and time plays an important role in tuning size, phase and morphology of particles.[101]

Scientists have attempted to synthesized bulk as well as nanobulk $Cu_2ZnSnS_4$-based compounds as TE materials and introduced several strategies to improve the $ZT$ values. In quaternary nanocrystals the stoichiometric control is intricate due to the tendency of forming a plurality of compositional phases in initial reaction stages due to the difference in reactivity of the cationic precursors.[102] The precise phase and compositional engineering particularly fundamental to optimize TE properties. In this direction, nanoparticle-based bottom-up assembly technologies potentially offer an unprecedented level of control, of the phase and composition distribution within bulk nanomaterials. Even metastable phases not reached through any other method have been produced using solution processing techniques in nanometer size crystals.[103-105] In general, in bottom-up approach, it has been noticed that the substitution reactions are extremely powerful to adjust the nanoparticle composition as well as crystallographic phases. Based on the synthesis methods reported for other binary and ternary metal chalcogenide nanocrystals, similar approaches have been developed in recent years for CZTS and other quaternary Cu-M-Sn-S (M = metal) based materials.  Interestingly, in 2009, three groups reported quasi simultaneously the synthesis of CZTS nanocrystals: Guo *et al*. injected the S precursor solution (elemental sulfur in oleylamine (OAM)) into the hot solution of the metal precursors in OAM, while Riha *et al*. injected both the S/OAM and metal precursor solutions into hot trioctylphosphine oxide (TOPO).[106-108] The synthesis methodology by Steinhagen *et al*. differs from the others in the way that all precursors are mixed at room temperature in OAM and then heated to 280°C.[108] The mean particle sizes from these techniques in each cases are around 10 nm. The procedure by Steinhagen and coworkers provides better particle size, shape control. Thereafter, a series of attempts have been made to synthesize CZTS nanocrystals with varying experimental conditions and/or precursors to uncover a wide spectrum of particle characteristics in terms of particle size, shape, composition phase etc. For instance, in 2011, Li *et al*. synthesized the metastable WZ phase of CZTS by heating the metal chloride solution in 1-dodecanethiol (DDT), OAM, and oleic acid.[109] They hypothesized that DDT can play a significant role in obtaining the metastable WZ phase. It was found that the role of the surfactant (particularly long chain alkanethiols) is to stabilize intermediate products that aid the formation of WZ CZTS through assisted nucleation and growth of hexagonal $Cu_{1.94}S$ nanocrystals via templating process.[110] The heterostructured WZ-CZTS $Cu_{1.94}S$ nanocrystals eventually converted to wurtzite via cation diffusion.[111,112] Thus, the surfactants stabilize an intermediate that locks in the crystal structure. Moreover, later on, it was found that the template-based particle growth is largely dependent on the nuclei stoichiometry.[112] For example, in case of binary compounds, investigations on copper-based binary compounds found that CuS and $Cu_9S_5$ nucleus were the primary reason to form zincblende (ZB) or WZ structure, respectively.[110] To control the crystallite phase, cation substitution into the intermediate phase represents an interesting approach. Li *et al*., and Zhu *et al*. prepared WZ CZTS by diffusing Zn into WZ $Cu_2SnS_3$.[113,114] On the other hand, in terms of nanocrystals shape and size several methodologies have been employed for CZTS synthesis using elemental sulfur and OAM, leading to nanocrystals of faceted or spherical shape in a size range of 5 to 25 nm.[98] Shorter amines like ethylenediamine, used as a solvent and ligand, yielded small aggregated particles or wires.[109] While, employing thiourea as sulfur precursor in association with ethylene glycol as solvent results mostly large, aggregated particles (100-500 nm).[115-117] On the flip side, using OAM as ligand and solvent in combination with thiourea yielded smaller particles (length = 20 nm; width =15 nm).[118,119] It has been noticed that in the presence of an amine (OAM or trioctylamine) yields elongated shaped nanocrystals. Singh *et al*. studied the effect of thiols (long chain alkanethiol, DDT) in the presence/absence of amines on the formation of WZ CZTS nanocrystals, and observed that a combination of both compounds is necessary for the formation of nano-particles (rods) with narrow particle size distribution.[120] As can be seen from these few recent examples, a huge variety of possible elemental combinations in quaternary nanocrystals constitutes a very fertile playground for chemists and open ways for designing novel functional materials. The rapid progress in the development of chemical synthesis methods allows for controlling simultaneously the size, shape and composition of multinary nanocrystals.

Except for few reports for the one-pot synthesis of WZ $Cu_3MSnS_5$ (M = Al or In) compounds, representing a new generation of copper-based quaternary semiconductors, not much research has been done. First and foremost, although Feng *et al*. and Pan *et al*. succeeded to make $I_3$-III-IV-$VI_5$ nanoparticles but with poor particle size and shape control accompanied with an extensively long synthesis process.[93,94] Secondly, the *ab-initio* prediction about the I-IIIA-IV-VI based materials to possess the very low $\kappa_{lat}$ creates the opportunity to evaluate these materials for TE's.[92] And most important, this new class of compounds provides an opportunity for systematic investigation of material's transport properties through elemental substitution and/or doping as an attempt to clarify the material's structural properties and performance analysis. It is a big challenge and needs to be investigated.

## 1.5 Research Objective

The rising concerns over the waste heat and environmental protection drives scientists towards the development of sustainable TE materials. Despite of enormous growth in the TE's with high performance materials; the low earth-abundance and toxicity of the constituents hinders the large-scale applications with sustainability. In this renaissance era, in search of sustainable TE materials, copper-based quaternary $I_3$-III-IV-$VI_5$ compounds have been selected as a base model for this study. Therefore, the objective of this research is to prepare the nanostructured

TE materials fabricated from chemically synthesized I-III-IV-VI quaternary compound nanocrystals. Beginning with the nanostructuring in the chemically synthesized $I_3$-III-IV-$VI_5$, substitution reactions between Zn and Al and thereby between Al and Ga; followed by doping with $Cu_2SnS_3$ (CTS) strategies were employed as an attempt not only to synthesize new materials, but also to investigate their TE materials transport properties and their correlation with several material structural parameters. With these objectives, a series of nanocrystals have been prepared using one-pot synthesis methodology. The synthesized nanocrystals analysis in terms of the composition, particle shape, size, crystal phases type and strains and TE properties, establishes a database and a methodology to support the foundation library for the future practical use. The material's structural features such as particle shape and size were analyzed using transmission electron microscopy (TEM); and the amount and types of phases were determined by X-ray diffraction (XRD); while the particle compositions were investigated by scanning electron microscopy coupled with energy dispersive X-ray spectroscopy (SEM-EDS). On the other hand, the TE materials transport properties were determined using laser flash analysis and ZEM-3 analyzer. This research will address the following topics and their details have been discussed in the later chapters:

(1) Nanobulk TE materials fabricated from chemically synthesized $Cu_3Zn_{1-x}Al_xSnS_{5-y}$ nanocrystals, which served as building blocks.

(2) Effect of Gallium substitution in $Cu_3Al_{1-x}Ga_xSnS_5$ nanobulk materials on TE properties.

(3) Investigate the TE properties as an effect of CTS nanoinclusions in CATS system utilized as building blocks to fabricate nanobulk materials. The study has been attempted to evaluate the effect of blending nanoinclusions on the thermal and electrical transport properties.

(4) Assess the correlation between the material structural features such as crystal phase type, content etc. on the TE properties of CATS-CTS host-nanoinclusions samples.

The general introduction of the TE materials has been discussed in the Chapter 1. This chapter includes the basic concepts of TE's, conventional TE materials, synthesis, effective methodologies to vary transport properties. The challenges associated with present TE materials have been postulated in combination with a brief outlook about the scope of this research, as one of the plausible solution.

In Chapter 2, we chemically synthesized Cu-Zn-Sn-S nanocrystals and fabricated a $Cu_3ZnSnS_{5-y}$ TE material using nanocrystals as building blocks. $ZT$ value of 0.39 at 658 K was achieved for the $Cu_3ZnSnS_{5-y}$ material. We substituted Zn with Al in the $Cu_3ZnSnS_{5-y}$ system to form $Cu_3Zn_{1-x}Al_xSnS_{5-y}$ ($x$ = 0.25, 0.5, 0.75, and 1) to lower the $\kappa_{lat}$ of the resulting materials. Complete substitution of Al for Zn substantially decreased the $\kappa_{lat}$ and dramatically increased the $\sigma$ of the material. However, the $ZT$ value could not be significantly enhanced, which could be primarily attributed to the high $\kappa_{car}$. These results highlight the production of $Cu_3Zn_{1-x}Al_xSnS_{5-y}$ TE materials and unveil the scope for improvement of $ZT$ values by altering transport properties.

The Chapter 3 demonstrates the technique to curtail the $\kappa_{car}$ of the CATS nanobulk TE materials without compromising the already suppressed $\kappa_{lat}$. In this chapter, the effect of Ga substitution in $Cu_3Al_{1-x}Ga_xSnS_5$ nanobulk materials on the material transport properties of the materials has been systematically investigated. The $ZT$ value of the $Cu_3Al_{1-x}Ga_xSnS_5$ nanobulk at $x = 0.5$ was found to be more than twice ($ZT = 0.26$) than the pristine CATS nanobulk at 665 K, primarily because of the significant reduction in $\kappa_{car}$. A detailed analysis of the correlation among transport parameters, crystal structure and performance of the $Cu_3Al_{1-x}Ga_xSnS_5$ nanobulks ($0.25 \leq x \leq 1$) revealed that a larger fraction of ZB phase leads to a higher *PF*.

The Chapter 4 examines the ability of CTS nanocrystals as nanoinclusions in the CATS system for reducing the $\kappa_{\mathrm{car}}$ without negatively impact the $\kappa_{\mathrm{lat}}$. The doping content of CTS gradually varied from 0.1 wt%, 1 wt%, 3 wt%, 5 wt% and 10 wt% in CATS. The fabricated nanobulk TE material shows, interestingly, WZ as a major crystalline phase from 1 wt% CTS content onwards; which increases with the increase in CTS nanoinclusions. Furthermore, the dramatic increase in $S$ was found to be not sufficient for compensating the decrease in the $\sigma$ and thereby suppressed the *PF* greater than expected. The results direct the attention towards the role of interface between the nanoinclusion and primary matrix in deciding the fate of, especially, $\sigma$. The 0.1 wt% CTS nanoinclusions leads provided better trade-off between $\sigma$ and $S$ without compromising $\kappa$ and thus improved the *ZT* value up to 3× than the neat CATS system. The 0.1 wt% CTS containing sample possess greater ZB phase content than any other pellets under consideration and prevail the importance of symmetric crystal structure content in deciding the fate of TE properties.

Chapter 5 disseminates the general summary and conclusions followed by the future outlook of the research presented in this dissertation.

## References

(1) Atkins, P.; Paula, J. D. Equilibrium. *Physical Chemistry*; 6th Ed.; W. H. Freeman and Company: New York, **2006**; pp 28-116.

(2) IRENA, REthinking Energy **2017**: Accelerating the global energy transformation. International Renewable Energy Agency, Abu Dhabi. (Weblink: https://www.irena.org/-/media/Files/IRENA/Agency/Publication/2017/IRENA_REthinking_Energy_2017.pdf?la=en&hash=38EF7869A341CC05ADC76C9B56BE7556BA5826E2).

(3) Cahill, D. G.; Pohl, R. O. Lattice Vibrations and Heat Transport in Crystals and Glasses. *Ann. Rev. Phys. Chem*. **1988**, *39*, 93-121.

(4) Sootsman, J. R.; Chung, D. Y.; Kanatzidis. New and Old Concepts in Thermoelectric Materials. *Angew. Chem. Int. Ed*. **2009**, *48*, 8616-8639.

(5) Riffat, S. B.; Ma, X. Thermoelectrics: A Review of Present and Potential Applications. *Appl. Therm. Engg*. **2003**, *23*, 913-935.

(6) Seebeck, T.J. Magnetische Polarisation der Metalle und Erze durch Temperatur-Differenz. *Technical report*, Reports of the Royal Prussian Academy of Science, Berlin, **1823**.

(7) Thermodynamics and Thermoelectricity: *Continuum Theory and Modelling of Thermoelectric Elements*, 1st Ed.; Ed: Goupil, C. Wiley-VCH Verlag GmbH & Co. **2016**, pp 1-73.

(8) Herring. C. Theory of the Thermoelectric Power of Semiconductors. *Phys. Rev*. **1954**, *96*, 1163-1187.

(9) Thomson, W. Account of Researches in Thermoelectricity. *Proc. R. Soc*. London **1854**, *7*, 49-58.

(10) Altenkirch, E. Elektrothermische Kälteerzeugung und reversible elektrische Heizung. *Phys. Z.* **1911**, 12, 920-924.

(11) Ioffe, A. F. Semiconductor Thermoelements and Thermoelectric Cooling. Infosearch Ltd.: London, **1957**; pp 96-121.

(12) Bulusua, A.; Walker, D.G. Review of Electronic Transport Models for Thermoelectric Materials. *Superlattices and Microstructures* **2008**, *44*, 1-36.

(13) Singh, J. *Modern Physics for Engineers*: WILEY-VCH Verlag GmhH & Co. KGaA: Toronto; Appendix B, **2004**; pp 353-363.

(14) Kasap, S.; Cyril, K.; Ruda, H. E. Electrical Conduction in Metals and Semiconductors: *Handbook of Electronic and Photonic Materials*. Springer: Cham; **2017**; pp 19-45.

(15) Ziman, J. M. *Electrons and Phonons*. Oxford University Press, London, **1960**.

(16) *Thermoelectrics: Design and Materials*; 1st Ed.; Lee, H. S., Ed.; Wiley: Chichester, UK, **2017**; pp 230-250.

(17) *Thermal Conductivity: Theory Properties and Applications*; 1st Ed.; Tritt, T. M., Ed.; Kluwer Academic / Plenum Publishers: New York, **2004**; pp 105-122.

(18) Bude, J. Scattering Mechanisms for Semiconductor Transport Calculations: *Monte Carlo Device Simulation: Full Band and Beyond*; Hess, K., Ed.; Springer Science + Business Media LLC, New York, **1991**; pp 27-66.

(19) Wang, X.; Yang, Y.; Zhu, L. Effect of Grain Sizes and Shapes on Phonon Thermal Conductivity of Bulk Thermoelectric Materials. *J. Appl. Phys*. **2011**, *110*, 024312.

(20) Terasaki, I. Thermal Conductivity and Thermoelectric Power of Semiconductors. *Comprehensive Semiconductor Science Technology* **2011**, *1*, 326-358.

(21) Alboni, P. N.; Ji, X.; He, J.; Gothard, N.; Hubbard, J.; Tritt, T. M. Synthesis and Thermoelectric Properties of ''Nano-Engineered'' $CoSb_3$ Skutterudite Materials. *J. Elect. Mater*. **2007**, *36*, 711-715.

(22) Kumar, G. S.; Prasad, G.; Pohl, R. O. Review Experimental Determinations of the Lorenz Number. *J. Mater. Sci*. **1993**, *28*, 4261-4272.

(23) Cohn, J. L.; Nolas, G. S.; Fessatidis, V.; Metcalf, T. H.; Slack, G. A. Glass-Like Heat Conduction in High-Mobility Crystalline Semiconductors. *Phys. Rev. Lett*. **1999**, *82*, 779-782.

(24) Takabatake, T.; Suekuni, K.; Nakayama, T.; Kaneshita, E. Phonon-Glass Electron-Crystal Thermoelectric Clathrates: Experiments and Theory. *Rev. Modern Phys*. **2014**, *86*, 669-718.

(25) Biswas, K.; He, J.; Blum, I. D.; Wu, C. I.; Hogan, T. P.; Seidman, D. N.; Dravid, V. P.; Kanatzidis. High-Performance Bulk Thermoelectrics with All-Scale Hierarchical Architectures. *Nature* **2012**, *489*, 414-418.

(26) Snyder, G. J.; Toberer, E. S. Complex Thermoelectric Materials. *Nat. Mater*. **2008**, *7*, 105-114.

(27) Xiao, Y.; Zhao, L-. D. Charge and Phonon Transport in PbTe-based Thermoelectric Materials. *npj Quantum Mater*. **2018**, *3*, 55.

(28) Pei, Y.; LaLonde, A. D.; Heinz, N. A.; Snyder, G. J. High Thermoelectric Figure of Merit in PbTe Alloys Demonstrated in PbTe-CdTe. *Adv. Energy Mater*. **2012**, *2*, 670-675.

(29) Pei, Y.; Wang, H.; Snyder, G. J. Band Engineering of Thermoelectric Materials. *Adv. Mater*. **2012**, *24*, 6125-6135.

(30) LaLonde, A. D.; Pei, Y.; Snyder, G. J. Reevaluation of $PbTe_{1-x}I_x$ as High-Performance *n*-type Thermoelectric Material. *Energy Environ. Sci*. **2011**, *4*, 2090-2096.

(31) Plirdpring, T.; Kurosaki, K.; Kosuga, A.; Day, T.; Firdosy, Ravi, V.; Snyder, G. J.; Harnwunggmoung, A.; Sugahara, T.; Ohishi, Y.; Muta, H.; Yamanaka, S. Chalcopyrite $CuGaTe_2$: A High-Efficiency Bulk Thermoelectric Material. *Adv. Mater*. **2012**, *24*, 3622-3626.

(32) Singh, M.; Miyata, M.; Nishino, S.; Mott, D.; Koyano, M.; Maenosono, S. Chalcopyrite Nanoparticles as a Sustainable Thermoelectric Material. *Nanomaterials* **2015**, *5*, 1820-1830.

(33) Nomura, A.; Choi, S.; Ishimaru, M.; Kosuga, A.; Chasapis, T.; Ohno, S.; Snyder, G. J.; Ohishi, Y.; Muta, H.; Yamanaka, S.; Kurosaki, K. Chalcopyrite $ZnSnSb_2$: A Promising Thermoelectric Material. *Appl. Mater. Interf*. **2018**, *10*, 43682-43690.

(34) Liu, M-. L.; Huang, Q-. F.; Chen, L-. D.; Chen, I-. W. A Wide-Band-Gap *p*-type Thermoelectric Material Based on Quaternary Chalcogenides of $Cu_2ZnSnQ_4$ (Q = S, Se). *Appl. Phys. Lett*. **2009**, *94,* 202103.

(35) Zhang, J.; Liu, R.; Cheng, N.; Zhang, Y.; Yang, J.; Uher, C.; Shi, X.; Chen, L.; Zhang, W. High-Performance Pseudocubic Thermoelectric Materials from Non-cubic Chalcopyrite Compounds. *Adv. Mater*. **2014**, *26*, 3848-3853.

(36) Lu, Y.; Chen, S.; Wu, W.; Du, Z.; Chao, Y.; Cui, J. Enhanced Thermoelectric Performance of a Chalcopyrite Compound $CuIn_3Se_{5-x}Te_x$ ($x = 0{\sim}0.5$) Through Crystal Structure Engineering. *Sci. Rep*. **2017**, *7*, 40224.

(37) Mangelis, P.; Vaqueiro, P.; Powell, A. V. Improved Thermoelectric Performance Through Double Substitution in Shandite-Type Mixed-Metal Sulfides. *Appl. Energy Mater*. **2020**, *3*, 2168-2174.

(38) Xiao. C. *Synthesis and Optimization of Chalcogenides Quantum Dots Thermoelectric Materials*. Springer Thesis: Springer-Verlag Berlin Heidelberg **2016**. (DOI 10.1007/978-3-662-49617-6).

(39) Coughlan, C.; Ibanez, M.; Dobrozhan, O.; Singh, A.; Cabot, A.; Ryan, K. M. Compound Copper Chalcogenide Nanocrystals. *Chem. Rev*. **2017**, *117*, 5865-6109.

(40) Trizio, L. D.; Manna, L. Forging Colloidal Nanostructures via Cation Exchange Reactions. *Chem. Rev*. **2016**, *116*, 10852-10887.

(41) Duann, X.; Hu, K.; Ding, S.; Man, D.; Jin, H. Influence of Ga-Doping on the Thermoelectric Properties of $Bi_{(2-x)}Ga_xTe_{2.7}Se_{0.3}$ Alloy. *Pro. Nat. Sci.-Mater*. **2015**, *25*, 29-33.

(42) Kim, K.; Kim, G.; Kim, S.; Lee, K. H.; Lee, W. Clarification of Electronic and Thermal Transport Properties of Pb-, Ag-, and Cu-Doped *p*-type $Bi_{0.52}Sb_{1.48}Te_3$. *J. Alloy. Compd*. **2019**, *772*, 593-602.

(43) Wu, D.; Zhao, L-. D.; Tong, X.; Li, W.; Wu, L.; Tan, Q.; Pei, Y.; Huang, L.; Li, J-. F.; Zhu, Y.; Kanatzidis, M. G.; He, J. Superior Thermoelectric Performance in PbTe-PbS Pseudo-binary: Extremely Low Thermal Conductivity and Modulated Carrier Concentration. *Energy Environ. Sci*. **2015**, *8*, 2056-2068.

(44) Sun, Y.; Thompson, S. E.; Nishida, T. *Strain Effects in Semiconductors*: *Theory and Applications*; Springer: New York, USA, **2010**; pp 23-50.

(45) Wolf, M.; Hinterding, R.; Feldhoff, A. High Power Factor vs. High *ZT*-A Review of Thermoelectric Materials for High-Temperature Application. *Entropy* **2019**, *21*, 1058.

(46) Mamura, H.; Bhuiyana, M. R. A.; Korkmazb, F.; Nil, M. A Review on Bismuth Telluride ($Bi_2Te_3$) Nanostructure for Thermoelectric Applications. *Renew. Sust. Energ. Rev*. **2018**, *82*, 4159-4169.

(47) Hua, S. C. Design, Growth and Characterization of PbTe-Based Thermoelectric Materials. *Prog. Cryst. Growth Ch*. **2019**, *65*, 47-94.

(48) Pérez-Taborda, J. A.; Caballero-Calero, O.; Martín-González, M. Silicon-Germanium (SiGe) Nanostructures for Thermoelectric Devices: Recent Advances and New Approaches to High Thermoelectric Efficiency. *New Research on Silicon - Structure, Properties, Technology*; INTECH **2017**, 183-206. (DOI: 10.5772/67730).

(49) Zhang, X.; Zhao, L-. D. Thermoelectric materials: Energy Conversion Between Heat and Electricity. *J. Materiomics* **2015**, *1*, 92-105.

(50) Kishore, R. A.; Priya, S. A Review on Low-Grade Thermal Energy Harvesting: Materials, Methods and Devices. *Materials* **2018**, *11*, 1433.

(51) Freer, R.; Powell, A. V. Realising the Potential of Thermoelectric Technology: A Roadmap. *J. Mater. Chem. C*, **2020**, *8*, 441-463.

(52) Witting, I. T.; Chasapis, T. C.; Ricci, F.; Peters, M.; Heinz, N. A.; Hautier, G.; Snyder, G. J. The Thermoelectric Properties of Bismuth Telluride. *Adv. Electron. Mater*. **2019**, *5*, 1800904.

(53) Goldsmid, H. J. Bismuth Telluride and Its Alloys as Materials for Thermoelectric Generation. *Materials* **2014**, *7*, 2577-2592.

(54) Allgaier, R. S.; Scanlon, W. W. Mobility of Electrons and Holes in PbS, PbSe, and PbTe between Room Temperature and 4.2 °K. *Phys. Rev*. **1958**, *111*, 1029-1037.

(55) Gibbs, Z. M.; Kim, H.; Wang, H.; White, R. L.; Drymiotis, F.; Kaviany, M.; Snyder, G. J. *Appl. Phys. Lett*. **2013**, *103*, 262109.

(56) Zhao, L-. D.; He, J.; Hao, S.; Wu, C-. I.; Hogan, T. P.; Wolverton, C.; Dravid, V. P. Kanatzidis. Raising the Thermoelectric Performance of *p*‑Type PbS with Endotaxial Nanostructuring and Valence-Band Offset Engineering Using CdS and ZnS. *J. Am. Chem. Soc*. **2012**, *134*, 16327-16336.

(57) Allgaier, R. S.; Houston, B. B. Hall Coefficient Behavior and the Second Valence Band in Lead Telluride. *J. Appl. Phys*. **1966**, *37*, 302-309.

(58) Korkosz, R. J.; Chasapis, T. C.; Lo, S.; Doak, J. W.; Kim, Y. J.; Wu, C-., I.; Hatzikraniotis, E.; Hogan, T. P.; Seidman, D. N.; Wolverton, C.; Dravid, V. P.; Kanatzidis, M. G. High *ZT* in p‑Type $(PbTe)_{1-2x}(PbSe)_x(PbS)_x$ Thermoelectric Materials. *J. Am. Chem. Soc*. **2014**, *136*, 3225-3237.

(59) LaLonde, A. D.; Pei, Y.; Wang, H.; Snyder, G. J. Lead Telluride Alloy Thermoelectrics. *Mater. Today* **2011**, *14*, 526-532.

(60) Parker, W. J.; Jenkins, R. J.; Butler, C. P.; Abbott, G. L. Flash Method of Determining Thermal Diffusivity, Heat Capacity, and Thermal Conductivity. *J. Appl. Phys*. **1961**, *32*, 1679-1684.

(61) Gueguen, A.; Poudeu, P. F. P.; Pcionek, R.; Kong, H.; Uher, C.; Kanatzidis, M. G. Thermoelectric Properties of the Nanostructured $NaPb_{18-x}Sn_xMTe_{20}$ (M = Sb, Bi) Materials. *Mater. Res. Soc. Symp. Proc*. **2007**, *1044*, U08-05.

(62) Zhang, Q.; Cao, F.; Liu, W.; Lukas, K.; Yu, B.; Chen, S.; Opeil, C.; Broido, D.; Chen, G.; Ren, Z. Heavy Doping and Band Engineering by Potassium to Improve the Thermoelectric Figure of Merit in *p*-Type PbTe, PbSe, and $PbTe_{1-y}Se_y$. *J. Am. Chem. Soc*. **2012**, *134*, 10031-10038.

(63) Cohen, I.; Kaller, M.; Komisarchik, G.; Fuks, D.; Gelbstein. Enhancement of the Thermoelectric Properties of *n*-type PbTe by Na and Cl co-Doping. *J. Mater. Chem. C* **2015**, *3*, 9559-9564.

(64) Rawat, P. K.; Paul, B.; Banerji, P. Exploration of Zn Resonance Levels and Thermoelectric Properties in I‑Doped PbTe with ZnTe Nanostructures. *Appl. Mater. Interf*. **2014**, *6*, 3995-4004.

(65) Girard, S. N.; He, J.; Zhou, X.; Shoemaker, D.; Jaworski, C. M.; Uher, C.; Dravid, V. P.; Heremans, J. P.; Kanatzidis, M. G. High Performance Na-doped PbTe-PbS Thermoelectric Materials: Electronic Density of States Modification and Shape-Controlled Nanostructures. *J. Am. Chem. Soc*. **2011**, *133*, 16588-16597.

(66) Tan, G.; Shi, F.; Hao, S.; Zhao, L-. D.; Chi, H.; Zhang, X.; Uher, C.; Wolverton, C.; Dravid, V. P.; Kanatzidis. Non-Equilibrium Processing Leads to Record High Thermoelectric Figure of Merit in PbTe-SrTe. *Nature Commun*. **2016**, *7*, 12167.

(67) Steele, M. C.; Rosi, F. D. Thermal Conductivity and Thermoelectric Power of Germanium Silicon Alloys. *J. Appl. Phys*. **1958**, *29*, 1517-1520.

(68) Johnson, V. A.; Horovitz, K. L. Theory of Thermoelectric Power in Semiconductors with Applications to Germanium. *Phys. Rev*. **1953**, *92*, 226-232.

(69) Mingo, N.; Hauser, D.; Kobayashi, N. P.; Plissonnier, M.; Shakouri, A. "Nanoparticle-in-Alloy" Approach to Efficient Thermoelectrics: Silicides in SiGe. *Nano Lett*. **2009**, 9, 711-715.

(70) Zebarjadi, M.; Joshi, G.; Zhu, G.; Yu, B.; Minnich, A.; Lan, Y.; Wang, X.; Dresselhaus, M.; Ren, Z.; Chen, G. Power Factor Enhancement by Modulation Doping in Bulk Nanocomposites. *Nano Lett*. **2011**, *11*, 2225-2230.

(71) Joshi, G.; Lee, H.; Lan, Y.; Wang, X.; Zhu, G.; Wang, D.; Gould, R. W.; Cuff, D. C.; Tang. M. Y.; Dresselhaus, M. S.; Chen, G.; Ren, Z. Enhanced Thermoelectric Figure-of-Merit in Nanostructured *p*-type Silicon Germanium Bulk Alloys. *Nano Lett*. **2008**, *8*, 4670-4674.

(72) Wang, X. W.; Lee, H.; Lan, Y. C.; Zhu, H.; Joshi, G.; Wang, D. Z.; Yang, J.; Muto, A. J.; Tang, M. T.; Klatsky, J.; Song, S.; Dresselhaus, M. S.; Chen, G.; Ren, Z. F. Enhanced Thermoelectric Figure of Merit in Nanostructured *n*-type Silicon Germanium Bulk Alloy. *Appl. Phys. Lett*. **2008**, *93*, 193121.

(73) Fleischer, M. The Abundance and Distribution of the Chemical Elements in the Earth's Crust. *J. Chem. Educ*. **1954**, *31*, 446-455.

(74) Qiu, P.; Shi, X.; Chen, L. Cu-based Thermoelectric Materials. *Energy Storage Mater*. **2016**, *3*, 85-97.

(75) Ge, Z-. H.; Zhao, L-. D.; Wu, D.; Liu, D.; Liu, X.; Zhang, B-. P.; Li, J-. F.; He, J. Low-Cost, Abundant Binary Sulfides as Promising Thermoelectric Materials. *Mater. Today* **2016**, *19*, 227-239.

(76) Sharma, S. D.; Khasimsaheb, B.; Chen, Chen, Y. Y.; Neeleshawar, S. Enhanced Thermoelectric Performance of $Cu_2ZnSnS_4$ (CZTS) by Incorporating Ag Nanoparticles. *Ceram. Int*. **2019**, *45*, 2060-2068.

(77) Wang, B.; Xiang, H.; Nakayama, T.; Zhou, J.; Li, B. Theoretical Investigation on Thermoelectric Properties of Cu-Based Chalcopyrite Compounds. *Phys. Rev. B* **2017**, *95*, 035201.

(78) He, Y.; Day, T.; Zhang, T.; Liu, H.; Shi, X.; Chen, L.; Snyder, G. J. High Thermoelectric Performance in Non-Toxic Earth Abundant Copper Sulfide. *Adv. Mat*. **2014**, *26*, 3974-3978.

(79) Yang, H.; Jauregui, L. A.; Zhang, G.; Chen, Y. P.; Wu, Y. Nontoxic and Abundant Copper Zinc Tin Sulfide Nanocrystals for Potential High-Temperature Thermoelectric Energy Harvesting. *Nano Lett*. **2012**, *12*, 540-545.

(80) Zhou, W.; Shijimaya, C.; Takahashi, M.; Miyata, M.; Mott, D.; Koyano, M.; Ohta, M.; Akatsuka, T.; Ono, H.; Maenosono, S. Sustainable Thermoelectric Materials Fabricated by using $Cu_2Sn_{1-x}Zn_xS_3$ Nanoparticles as Building Blocks. *Appl. Phys. Lett*. **2017**, *111*, 263105.

(81) Suekuni, K.; Kim, F. S.; Nishiate, H.; Ohta, M.; Tanaka, H. I.; Takabatake, T. High-Performance Thermoelectric Minerals: Colusites $Cu_{26}V_2M_6S_{32}$ (M = Ge, Sn). *Appl. Phys. Lett*. **2014,** *105*, 132107.

(82) Heo, J.; Laurita, G.; Muir, S.; Subramanian, M. A.; Keszler, D. A. Enhanced Thermoelectric Performance of Synthetic Tetrahedrites. *Chem. Mater*. **2014**, *26*, 2047-2051.

(83) Lu, X.; Morelli, D. T.; Xia, Y.; Ozolins, V. Increasing the Thermoelectric Figure of Merit of Tetrahedrites by Co-Doping with Nickel and Zinc. *Chem. Mater*. **2015**, *27*, 408-413.

(84) Bouyrie, Y.; Ohta, M.; Suekuni, K.; Kikuchi, Y.; Jood, P.; Yamamoto, A.; Takabatake, T. Enhancement in the Thermoelectric Performance of Colusites $Cu_{26}A_2E_6S_{32}$ (A = Nb, Ta; E = Sn, Ge) Using E-site Non-Stoichiometry. *J. Mater. Chem. C* **2017**, *5*, 4174-4184.

(85) Shen, Y.; Li, C.; Huang, R.; Tian, R.; Ye, Y.; Pan, L.; Koumoto, K.; Zhang, R.; Wan, C.; Wang, Y. Eco-friendly *p*-type $Cu_2SnS_3$ Thermoelectric Material: Crystal Structure and Transport Properties. *Sci. Rep*. **2016**, *6*, 32501.

(86) Tan, Q.; Sun, W.; Li, Z.; Li, J-. F. Enhanced Thermoelectric Properties of Earth-Abundant $Cu_2SnS_3$ via In Doping Effect. *J. Alloy. Compd*. **2016**, *672*, 558-563.

(87) Zhao, H.; Xu, X.; Li, C.; Zhang, R.; Huang, R.; Lv, Y.; Li, D.; Hu, X.; Pan, L.; Wang, Y. Cobalt-Doping in $Cu_2SnS_3$: Enhanced Thermoelectric Performance by Synergy of Phase Transition and Band Structure Modification. *J. Mater. Chem. A* **2017**, *5*, 23267-23275.

(88) Zhao, L.; Chen, C.; Pan, L.; Hu, X. Magnetic Iron Doping in $Cu_2SnS_3$ Ceramics for Enhanced Thermoelectric Transport Properties. *J. Appl. Phys*. **2019**, *125*, 095107.

(89) Xu, X.; Zhao, H.; Hu, X.; Pan, L.; Chen, C.; Li, D.; Wang, Y. Synergistic Role of Ni-Doping in Electrical and Phonon Transport Properties of $Cu_2Sn_{1-x}Ni_xS_3$. *J. Alloy. Compd.* **2017**, *728*, 701-708.

(90) Zhang, Z.; Zhao, H.; Wang, Y.; Hu, X.; Lyu, Y.; Cheng, C.; Pan, L.; Lu, C. Role of Crystal Transformation on the Enhanced Thermoelectric Performance in Mn-Doped $Cu_2SnS_3$. *J. Alloy. Compd*. **2019**, *780*, 618-625.

(91) Zhou, W.; Dwivedi, P.; Shijimaya, C.; Ito, M.; Higashimine, K.; Nakada, T.; Takahashi, M.; Mott, D.; Miyata, M.; Ohta, M.; Miwa, H.; Akatsuka, T.; Maenosono, S.

Enhancement of the Thermoelectric Figure of Merit in Blended $Cu_2Sn_{1-x}Zn_xS_3$ Nanobulk Materials. *ACS Appl. Nano Mater.* **2018**, *1*, 4819-4827.

(92) Li, W.; Zhou, C.; Li, L. A First-Principles Theoretical Study on the Thermoelectric Properties of the Compound $Cu_5AlSn_2S_8$. *J. Electronic Mater*. **2015**, *45*, 1453-1458.

(93) Cui, Y.; Wang, G.; Pan, D. Colloidal Synthesis and Optical Properties of Metastable Wurtzite $I_3$-III-IV-$VI_5$ ($Cu_3InSnS_5$) Nanocrystals. *CrystEngComm*. **2013**, *15*, 10459-10463.

(94) Bai, T.; Xing, S.; Lou, Y.; Chen, C.; Huang, H.; Li, C.; Shi, X.; Feng, S. Colloidal Synthesis of Quaternary Wurtzite $Cu_3AlSnS_5$ Nanocrystals and Their Photoresponsive Properties. *ChemPlusChem* **2015**, *80*, 652-655.

(95) Datta, A.; Popescu, A.; Woods, L.; Nolas, G. S. The Bottom-Up Approach to Bulk Thermoelectric Materials with Nanoscale Domains: *Materials, Preparation, and Characterization in Thermoelectrics*; 1st Ed.; Rowe, D. M., Ed.; CRC Press: London, UK, **2012**; pp. 14-01–14-32.

(96) *Handbook of Thermoelectrics*; 1st Ed.; Rowe, D. M., Ed.; CRC Press: Boca Raton, FL, USA, **1995**; pp. 9-01–13-11.

(97) *Thermoelectrics Handbook: Macro to Nano*; 1st Ed.; Rowe, D. M., Ed.; CRC Press: Boca Raton, FL, USA, **2006**; pp. 19-01–20-06.

(98) Cao, M.; Shen, Y. A Mild Solvothermal Route to Kesterite Quaternary $Cu_2ZnSnS_4$ Nanoparticles. *J. Cryst. Growth* **2011**, *318*, 1117-1120.

(99) Demazeau, G.; Solvothermal Processes: Definition, Key Factors Governing the Involved Chemical Reactions and New Trends. *Z. Naturforsch*. **2010**, *65b*, 999-1006.

(100) Talapin, D. V.; Rogach, A. L.; Haase, M. Weller, H. Evolution of an Ensemble of Nanoparticles in a Colloidal Solution: Theoretical Study. *J. Phys. Chem. B* **2001**, *105*, 12278-12285.

(101) Ortega, S.; Ibanez, M.; Liu, Y.; Zhang, Y.; Kovalenko, M. V.; Cadavid, D.; Cabot, A. Bottom-up Engineering of Thermoelectric Nanomaterials and Devices from Solution Processed Nanoparticle Building Blocks. *Chem. Soc. Rev*. **2017**, *46*, 3510-3528.

(102) Aldakov, D.; Lefrancois, A.; Reiss, P. Ternary and Quaternary Metal Chalcogenide Nanocrystals: Synthesis, Properties and Applications. *J. Mater. Chem. C* **2013**, *1*, 3756-3776.

(103) Liu, Q.; Zhao, Z.; Lin, Y.; Guo, P.; Li, S.; Pan, D.; Ji, X. Alloyed $(ZnS)_x(Cu_2SnS_3)_{1-x}$ and $(CuInS_2)_x(Cu_2SnS_3)_{1-x}$ Nanocrystals with Arbitrary Composition and Broad Tunable Band Gaps. *Chem. Commun*. **2011**, *47*, 964-966.

(104) Jain, S.; Chawla, P.; Sharma, S. N.; Singh, D.; Vijayan, N. Efficient Colloidal Route to Pure Phase Kesterite $Cu_2ZnSnS_4$ (CZTS) Nanocrystals with Controlled Shape and Structure. *Superlattic. Microst*. **2018**, *119*, 59-71.

(105) Fan, F-. J.; Wu, L.; Yu, S-. H. Energetic I-III-$VI_2$ and $I_2$-II-IV-$VI_4$ Nanocrystals: Synthesis, Photovoltaic and Thermoelectric Applications. *Energy Environ. Sci*. **2014**, *7*, 190-208.

(106) Guo, Q.; Hillhouse, H. W.; Agrawal, R. Synthesis of $Cu_2ZnSnS_4$ Nanocrystal Ink and Its Use for Solar Cells. *J. Am. Chem. Soc*. **2009**, *131*, 11672-11673.

(107) Riha, S. C.; Parkinson, B. A.; Prieto, A. L. Solution-Based Synthesis and Characterization of $Cu_2ZnSnS_4$ Nanocrystals. *J. Am. Chem. Soc*. **2009**, *131*, 12054-12055.

(108) Steinhagen, C.; Panthani, M. G.; Akhavan, V.; Goodfellow, B.; Koo, B.; Korgel, B. A. Synthesis of $Cu_2ZnSnS_4$ Nanocrystals for Use in Low-Cost Photovoltaics. *J. Am. Chem. Soc*. **2009**, *131*, 12554-12555.

(109) Shi, L.; Pei, C.; Xu, Y.; Li, Q. Template-Directed Synthesis of Ordered Single-Crystalline Nanowires Arrays of $Cu_2ZnSnS_4$ and $Cu_2ZnSnSe_4$. *J. Am. Chem. Soc*. **2011**, *133*, 10328-10331.

(110) Li, Y.; han, Q.; Kim, T. W.; Shi, W. Synthesis of Wurtzite - Zincblende $Cu_2ZnSnS_4$ and $Cu_2ZnSnSe_4$ Nanocrystals: Insight into the Structural Selection of Quaternary and Ternary Compounds Influenced by Binary Nucleus. *Nanoscale* **2014**, *6*, 3777-3785.

(111) Han, S-. k.; Gong, M.; Yao, H-. B.; Wang, Z-. M.; Yu, S-. H.; One-Pot Controlled Synthesis of Hexagonal-Prismatic $Cu_{1.94}S$-ZnS, $Cu_{1.94}S$-ZnS-$Cu_{1.94}S$, and $Cu_{1.94}S$-ZnS-$Cu_{1.94}S$-ZnS-$Cu_{1.94}S$ Heteronanostructures. *Angew. Chem. Int. Ed*. **2012**, *51*, 6365-6368.

(112) Regulacio, M. D.; ye, C.; Lim, S. H.; Bosman, M.; Ye, E.; Chen, S.; Xu, Q-. H.; Han, M-. Y. Colloidal Nanocrystals of Wurtzite-Type $Cu_2ZnSnS_4$: Facile Non-injection Synthesis and Formation Mechanism. *Chem. Eur. J*. **2012**, *18*, 3127-3131.

(113) Wang, Y-. X.; Wei, M.; Fan, F-. J.; Zhuang, T-. T.; Wu, L.; Yu, S-. H.; Zhu, C-. F. Phase-Selective Synthesis of $Cu_2ZnSnS_4$ Nanocrystals through Cation Exchange for Photovoltaic Devices. *Chem. Mater*. **2014**, *26*, 5492-5498.

(114) Lu, X.; Zhuang, Z.; Peng, Q.; Li, Y. Wurtzite $Cu_2ZnSnS_4$ Nanocrystals: A Novel Quaternary Semiconductor. *Chem. Commun*. **2011**, *47*, 3141-3143.

(115) Zhou, Y-. L.; Zhou, W-. H.; Du, Y-. F.; Wu, S-. X. Hierarchical $Cu_2ZnSnS_4$ Particles for a Low-Cost Solar Cell: Morphology Control and Growth Mechanism. *J. Phys. Chem. C* **2011**, *115*, 19632-19639.

(116) Zhou, Y-. L.; Zhou, W-. H.; Du, Y-. F.; Li, M.; Wu, S-. X. Sphere-like Kesterite $Cu_2$ZnSnS4 Nanoparticles Synthesized by a Facile Solvothermal Method. *Mater. Lett.* **2011**, *65*, 1535-1537.

(117) Zaberca, O.; Dyrand, G. B.; Chane-Ching, J. Y. A General Route to the Synthesis of Surfactant-Free, Solvent-Dispersible Ternary and Quaternary Chalcogenide Nanocrystals. *J. Mater. Chem.* **2011**, *21*, 6483-6486.

(118) Khare, A.; Wills, A. W.; Ammerman, L. M.; Norrisz, D. J.; Aydil, E. S. Size Control and Quantum Confinement in $Cu_2ZnSnS_4$ Nanocrystals. *Chem. Commun.* **2011**, *47*, 11721-11723.

(119) Wei, M.; Du, Q.; Wang, D.; Liu, W.; Jiang, G.; Zhu, C. Synthesis of Spindle-like Kesterite $Cu_2ZnSnS_4$ Nanoparticles Using Thiourea as Sulfur Source. *Mater. Lett.* **2012**, *79*, 177-179.

(120) Singh, A.; Geaney, H.; Laffir, F.; Ryan, K. M. Colloidal Synthesis of Wurtzite $Cu_2ZnSnS_4$ Nanorods and Their Perpendicular Assembly. *J. Am. Chem. Soc.* **2012**, *134*, 2910-2913.

# Chapter 2

## Nanobulk Thermoelectric Materials Fabricated from Chemically Synthesized $Cu_3Zn_{1-x}Al_xSnS_{5-y}$ Nanocrystals

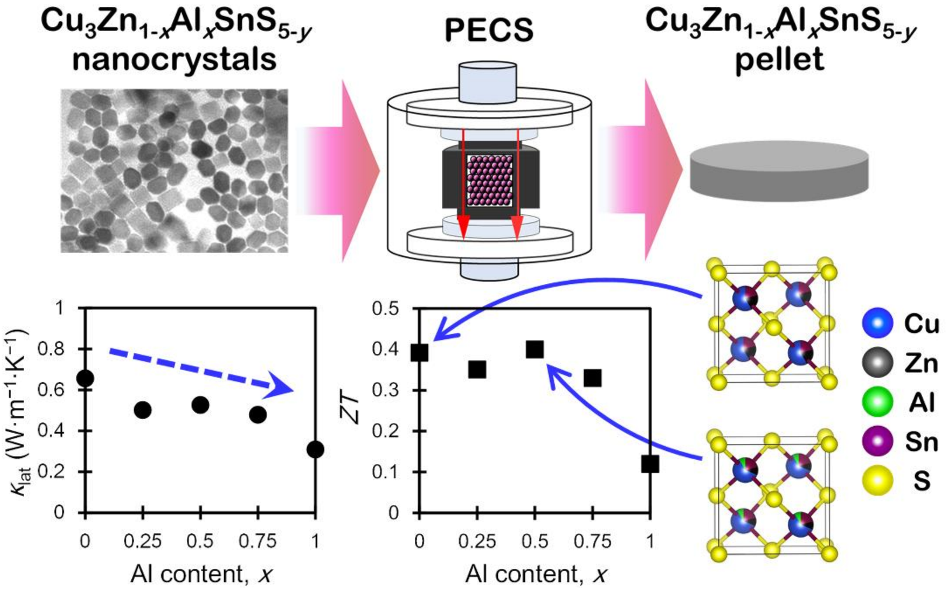

## 2.1 Introduction

Waste heat recovery has attracted attention in the last few decades, which has led to rapid progress in the development of thermoelectric materials. The performance of thermoelectric materials can be rated through a dimensionless quantity called the figure of merit ($ZT$), which is expressed as $ZT = \sigma S^2 T/\kappa$, where $\sigma$, $S$, $\kappa$, and $T$ are electrical conductivity, Seebeck coefficient, thermal conductivity, and absolute temperature, respectively. To improve the $ZT$ value, it is important to increase the power factor ($PF = \sigma S^2$) and/or decrease $\kappa$. In nanostructured materials, $\kappa$ can be decreased considerably by lowering the lattice thermal conductivity ($\kappa_{\mathrm{lat}}$) through phonon scattering at grain boundaries,[1,2] whereas $PF$ can be enhanced through quantum confinement or energy filtering.[3] Several researchers have demonstrated the enhancement of $ZT$ through nanostructuring, such as the formation of sintered nanocomposites.[4,5] However, most of these materials are prepared through complicated processes that are both energy and time consuming, which limits the development of thermoelectric materials and the wide application of thermoelectric devices. Furthermore, most thermoelectric materials are composed of heavy transition metals or rare earth elements, such as Sb or Te.[6] The exploitation of rare natural reserves makes such technology unsustainable. Therefore, it remains important to develop versatile thermoelectric materials from earth-abundant and eco-friendly constituent elements using scalable nanoparticle synthesis techniques and subsequent processing into bulk structures using facile methodologies.

Materials scientists have been exploring a wide range of cost-effective and eco-friendly materials that can be used in thermoelectric applications. Quaternary semiconductor copper zinc tin sulfide ($Cu_2ZnSnS_4$, CZTS) is one such material that has been widely explored for use in solar cells and has the ability to behave as a thermoelectric material because of its low $\kappa$ and high $S$.[7] Undoped

CZTS achieved a ZT value of 0.026 at 700 K.[8] Interestingly, Cu-doped CZTS ($Cu_{2.19}Zn_{0.80}Sn_{0.75}S_{3.53}$) exhibited a ZT value of 0.14 at 700 K, which is five times higher than that of stoichiometric CZTS, even though this ZT value is still low.[8] The low ZT value of CZTS is mainly caused by its low $\sigma$.[7] To improve the thermoelectric properties of CZTS, Zn atoms have been substituted with other transition metal atoms and/or S atoms have been substituted with Se atoms using various techniques including solid-state reaction, mechanical alloying, and wet chemical synthesis.[9–12] The results obtained by such modifications of CZTS are promising; for example, $ZT = 0.86$ (at 800 K) for $Cu_{2.2}Zn_{0.8}SnSe_4$,[13] $ZT = 0.7$ (at 850 K) for $Cu_2CoSnSe_4$ at 850 K,[14] $ZT = 0.71$ (at 685 K) for $Cu_{2.15}Cd_{0.85}SnSe_{3.9}$ at 685 K,[15] and $ZT = 0.6$ (at 800 K) for $Cu_{2.1}Mn_{0.9}SnSe_4$.[16] In addition, by replacing S with Se and Sn with Ge, the ZT value has also been markedly enhanced. For instance, $ZT = 0.55$ (at 723 K) for $Cu_{2.15}Zn_{0.85}GeSe_{3.9}$[17] and $ZT = 0.45$ (at 670 K) for $Cu_{2.075}Zn_{0.925}GeSe_4$.[18] However, these materials are no longer CZTS and most of them contain rarer and more toxic elements than CZTS.

Recently, we reported that the ZT value of Zn-doped $Cu_2SnS_3$ ($Cu_2Sn_{1-x}Zn_xS_3$)[19] could be dramatically enhanced up to 0.64 (at 670 K) by multiscale defect engineering.[20] This result suggests that the thermoelectric performance of existing systems can be substantially improved by controlling atomic structural properties such as lattice defects and non-stoichiometry along with impurities, nanostructure, and mesoscale structure. Therefore, multiscale defect engineering represents a new possibility to improve the ZT values of materials composed of sustainable elements with inferior thermoelectric performance.

Pan and coworkers synthesized wurtzite $Cu_3InSnS_5$ (CITS) nanocrystals, which belong to the $I_3$-III-IV-$VI_5$ family (a new generation of copper-based quaternary semiconductor), for solar cell applications.[21] However, the scarcity of In will limit the practical use of CITS materials. Bai et al.[22] recently reported that $Cu_3AlSnS_5$ (CATS) is a sustainable $I_3$-III-IV-$VI_5$ semiconductor that may be suitable as an alternative to CITS. In a nod to the materials described above, in this study, we attempt to synthesize $Cu_3Zn_{1-x}Al_xSnS_{5-y}$ nanocrystals as building blocks for sustainable thermoelectric materials by revisiting materials based on Cu, Zn, Sn, and S. Note that $Cu_3ZnSnS_{5-y}$ differs from conventional CZTS. The reason why Al is incorporated into Cu-Zn-Sn-S nanocrystals is that *ab initio* calculations predicted that the incorporation of Al into the I-IV-VI system may cause $\kappa_{\mathrm{lat}}$ to decrease.[23]

The work in this chapter is a part of my Ph.D. research, which has been published as an article. This work was supported by NEDO Research and Development for Innovative Use of Unused Thermal Energy. The work at AIST was supported as part of the International Joint Research Program for Innovative Energy Technology funded by the Ministry of Economy, Trade and Industry (METI), Japan. We thank Ms. Naoko Fujimoto of AIST for operating the ZEM-3 and LFA457 and Mr. Atsushi Yamamoto of AIST for supporting these measurements. Mr. Hiroshi Takida, Mr. Korefumi Kubota and Dr. Takeo Akatsuka of Nippon Shokubai Co., Ltd. supported the work of pelletization. The author also thank Mr. Koichi Higashimine of JAIST for helping with STEM-HAADF measurements.

## 2.2 Experimental

### *2.2.1 Materials*

The chemicals have been used for the synthesis of $Cu_3Zn_{1-x}Al_xSnS_{5-y}$ nanoparticles are shown in Table 2.1. All chemicals were purchased from Sigma-Aldrich and used without further purification.

### *2.2.2 Synthesis of $Cu_3Zn_{1-x}Al_xSnS_{5-y}$ Nanocrystals*

$Cu_3ZnSnS_{5-y}$ nanocrystals were synthesized as follows. $Cu(OAc)_2$ (5 mmol), $Sn(OAc)_2$ (2 mmol), $Zn(acac)_2$ (1 mmol), OAM (100 mL) and DDT (100 mL) were added to a three-necked flask equipped with a dry Ar inlet/outlet, trap sphere, condenser, heating mantle, thermocouple, and magnetic stirrer. First, the reaction mixture was stirred with Ar bubbling at room temperature for 5 min. Then, the temperature was increased to 100 °C and kept there for 10 min with Ar bubbling to remove volatile matter. Subsequently, the reaction temperature was further raised to 260 °C and held there for 1 h. After cooling the reaction mixture, the nanocrystals were separated from the reaction mixture by centrifugation at 5000 rpm for 3 min. The nanocrystals were then washed three times by repeating the following purification cycle: redispersion in hexane, centrifugation, and supernatant decantation. Finally, the obtained nanocrystals were dried under vacuum. $Cu_3Zn_{1-x}Al_xSnS_{5-y}$ nanocrystals were also synthesized in a similar manner by varying the input molar ratio of aluminum acetylacetonate [$Al(acac)_3$, purity 99%] ($x$) to $Zn(acac)_2$ while keeping the total amount of those two precursors constant [$Al(acac)_3 + Zn(acac)_2 = 1$ mmol].

**Table 2.1** List of chemicals, their chemical formula/abbreviation and purity %.

| Chemicals | Chemical Formula / Abbrevation | Purity % |
|---|---|---|
| Copper(II) acetate hydrate | $Cu(CO_2CH_3)_2 \cdot xH_2O$ / $Cu(OAc)_2 \cdot xH_2O$ | 98.0 |
| Zinc acetylacetonate hydrate | $Zn(C_5H_7O_2)_2 \cdot xH_2O$ / $Zn(acac)_2$ | 99.995 |
| Aluminium acetylacetonate | $C_{15}H_{21}AlO_6$ / $Al(acac)_3$ | 99.999 |
| Tin (II) acetate | $Sn(CH_3CO_2)_2$ / $Sn(OAc)_2$ | 99.0 |
| 1-Dodecanethiol | $CH_3(CH_2)_{11}SH$ / DDT | >98 |
| Oleylamine | $C_{18}H_{35}NH_2$ / OAM | 70.0 |
| Thiourea | $SC(NH_2)_2$ / TU | 99.0 |
| Hexane | $CH_3(CH_2)_4CH_3$ | 96.0 |
| Methanol | $CH_3OH$ | 99.8 |
| Toluene | $C_6H_5CH_3$ | 99.0 |

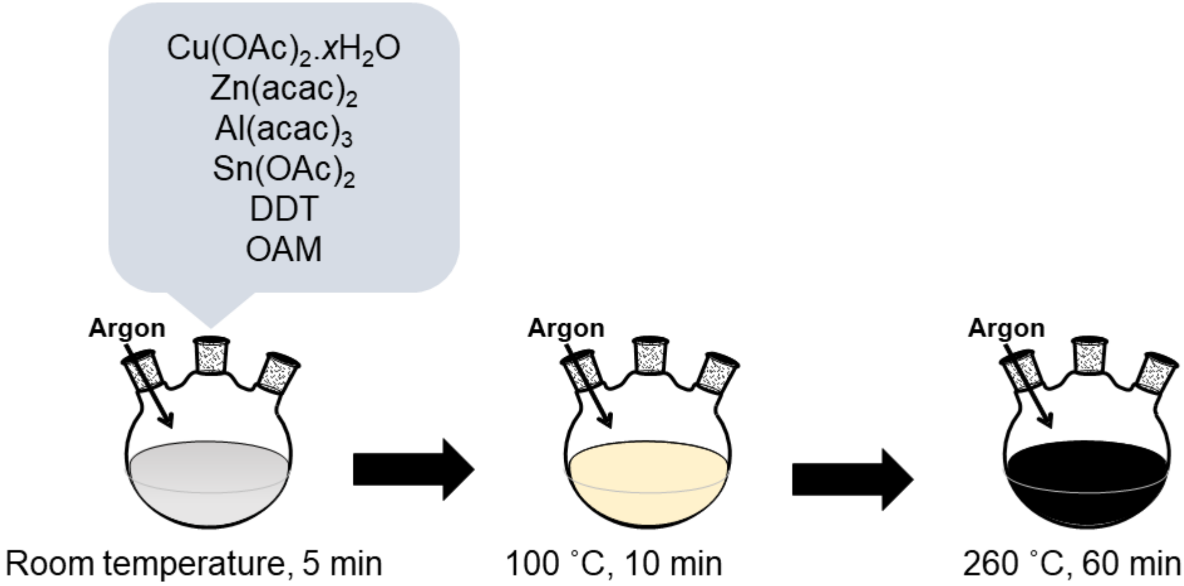

**Figure 2.1.** Synthetic scheme of $Cu_3Zn_{1-x}Al_xSnS_{5-y}$ nanocrystals system.

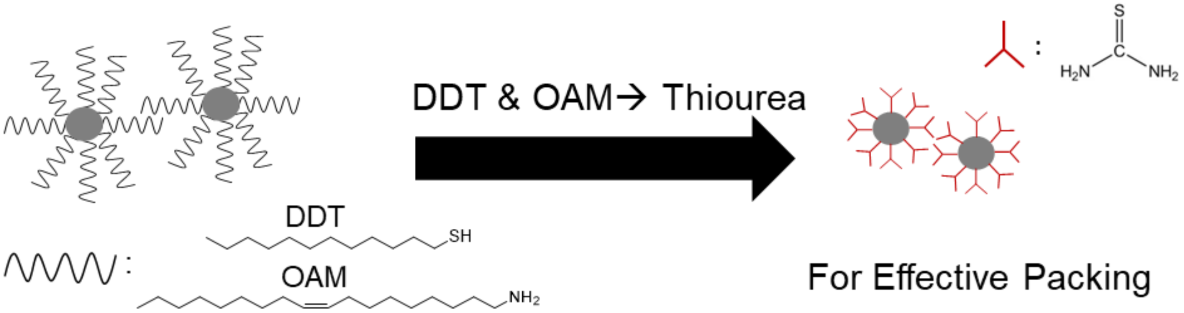

**Figure 2.2.** Schematic illustration of ligand exchange for $Cu_3Zn_{1-x}Al_xSnS_{5-y}$ nanocrystals system.

### *2.2.3 Ligand Exchange*

Thiourea (TU; Tokyo Chemical Industry, 10 g) was dissolved in methanol (Kanto Chemical, 400 mL). The TU solution was added to a dispersion of the nanocrystals (3.4 g) in toluene (250 mL). The mixture was sonicated for 1 h at room temperature. After the ligand exchange reaction, TU-capped nanocrystals were separated from the solution by centrifugation at 5000 rpm for 3 min. The TU-capped nanocrystals were washed by redispersion in a hexane/toluene mixture, centrifugation, and supernatant decantation. The TU-capped nanocrystals were redispersed in methanol (400 mL) and then toluene (125 mL) was added. The dispersion was subjected to centrifugation at 5000 rpm for 10 min to remove excess TU.

### *2.2.4 Pelletization*

After ligand exchange, nanocrystals were pelletized into a solid disk with a diameter of 10 mm and thickness of 2–3 mm using a pulsed electric current sintering machine (Sinterland LABOX-100) under the following conditions: vacuum, 3.5 Pa; temperature, 450 °C; pelletization pressure, 30 MPa; and sintering time, 5 min. The schematic illustration of pulse electric current sintering is shown in Figure 2.3. The pellets fabricated from **Powder_0**, **Powder_0.25**, **Powder_0.5**,

**Powder_0.75**, and **Powder_1** are referred to as **Pellet_0**, **Pellet _0.25**, **Pellet _0.5**, **Pellet _0.75**, and **Pellet _1**, respectively. The pellets were polished using silicon carbide abrasive paper (grit size 2000) before characterization. The densities of pellets were determined using a gas pycnometer (Shimadzu AccuPyc II 1340).

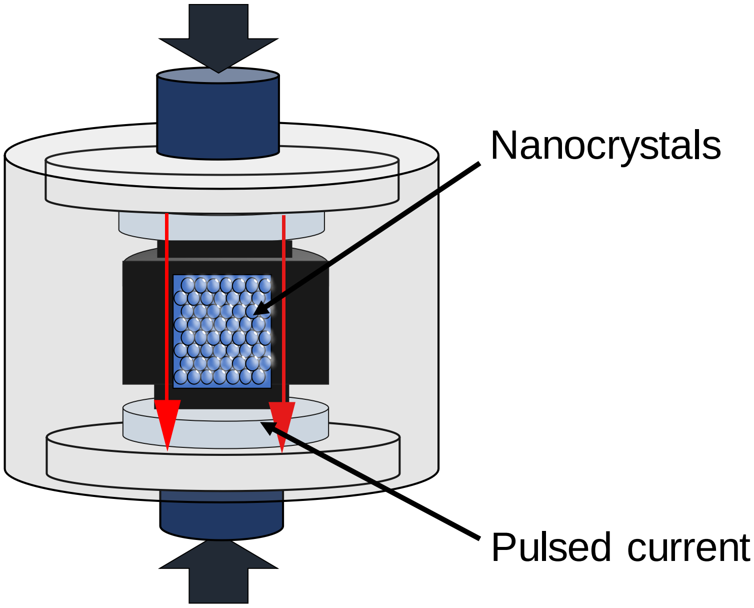

**Figure 2.3.** Schematic illustration for pulse electric current sintering.

## 2.3 Characterization Techniques

### *2.3.1 Structural and Compositional Analyses*

The synthesized nanocrystals were characterized by TEM (Hitachi H-7650 operated at 100 kV), XRD using a Rigaku Smartlab diffractometer with Cu K$\alpha$ radiation, STEM equipped with a high-angle annular dark-field (HAADF) detector and energy-dispersive X-ray spectroscopy (EDS) system (JEOL JEM-ARM200F operated at 200 kV) with a spherical aberration corrector and a nominal resolution 0.8 Å, SEM (Hitachi TM3030) equipped with an EDS system, and XPS (Shimadzu Kratos AXIS-ULTRA DLD).

### *2.3.2 Thermal Conductivity Measurement*

The samples used for thermal conductivity measurements are solid disks (pellets) with diameter of 10 mm and thickness of 2-3 mm whose surfaces were coated with graphite spray. First, $\kappa$ was measured for the pellets in the cross-plane direction by laser flash analysis (Netzsch LFA457). In this method, $\kappa$ (W $m^{-1}$ $K^{-1}$) was calculated as $\kappa = dcD$ where $d$ (kg $m^{-3}$), $c$ (J $kg^{-1}$ $K^{-1}$), and $D$ ($m^2$ $s^{-1}$) are the density, specific heat, and thermal diffusivity of the pellet, respectively. The values of $D$ were directly measured, while the values of $c$ were indirectly derived from a standard sample (Netzsch Pyroceram 9606) under an Ar flow of 100 mL·$min^{-1}$ over the temperature range of 300-670 K. The relative uncertainty of $\kappa$ was estimated to be smaller than 8% based on uncertainties of $d$, $c$ and $D$. Figure 2.4 shows the illustration of the setup for thermal conductivity measurement.

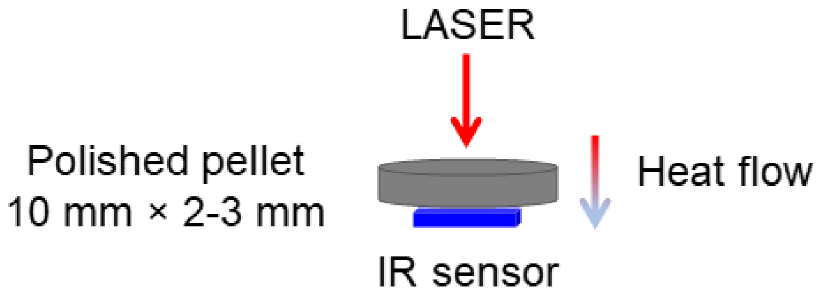

**Figure 2.4.** Schematic illustration for thermal conductivity measurement setup.

### *2.3.3 Seebeck and Electrical Conductivity Measurements*

Seebeck coefficient ($S$) and electrical resistivity ($\rho$) were measured in the in-plane direction by temperature differential and four-probe method, respectively, under a He atmosphere using ZEM-3 analyzer (ULVAC-Riko) by cutting the pellet into rectangular bar with dimensions approximately 8 mm × 2 mm × 2 mm as shown in Figure 2.5. In this method, $S$ ($\mathrm{V \cdot K^{-1}}$) is determined by the ratio of potential difference to the temperature difference (as shown in the equation $S = \Delta V/\Delta T$). Electrical conductivity ($\sigma$ ($\mathrm{S \cdot m^{-1}}$)) is given by $\sigma = 1/\rho$. The relative uncertainties of $S$ and $\sigma$ were estimated to be 5%. The $ZT$ values were calculated with those uncertainties in mind. The carrier thermal conductivity, $\kappa_{\mathrm{car}}$, was calculated as $\kappa_{\mathrm{car}} = L\sigma T - PF \cdot T$, where $L$ denotes the Lorentz number ($2.44 \times 10^{-8}$ W Ω $\mathrm{K^{-2}}$). Then, $\kappa_{\mathrm{lat}}$ was calculated as $\kappa_{\mathrm{lat}} = \kappa - \kappa_{\mathrm{car}}$. The $ZT$ value was calculated as $ZT = \sigma S^2 T/\kappa$.

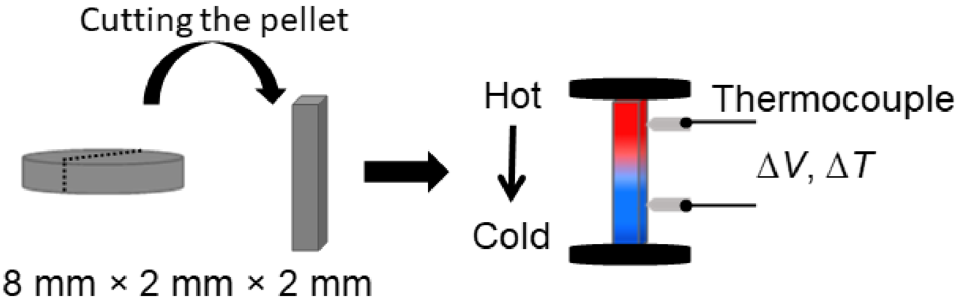

**Figure 2.5.** Illustration shown for sample cutting used for $S$ and $\rho$ measurement.

## 2.4 Results and Discussion

### *2.4.1 Morphology and Crystal Structure of Nanocrystals*

$Cu_3Zn_{1-x}Al_xSnS_{5-y}$ ($x$ = 0–1) nanocrystals with five different compositions were synthesized, which are referred to as **Powder_0**, **Powder_0.25**, **Powder_0.5**, **Powder_0.75**, and **Powder_1** corresponding to $x = 0$, 0.25, 0.5, 0.75 and 1, respectively. Depending on $x$, $y$ could vary to maintain electroneutrality of the system. Transmission electron microscopy (TEM) images of the as-synthesized nanocrystals are shown in Figure 2.6. All nanocrystals were uniform in size and shape with a hexagonal pencil-like morphology (several nanocrystals are standing up and others are lying down on the TEM grid). Average lengths and widths of nanocrystals are shown in Figure 2.6 (f), which indicates that the nanocrystal size decreases with increasing Al content. Because the nanocrystal size fundamentally depends on nucleation and growth as well as adsorption/desorption processes,[24] one plausible reason for the decrease in nanocrystal size with increasing $x$ is the low affinity between Al and 1-dodecanethiol (DDT) compared to that between Zn and DDT.[25] This phenomenon can be explained by the hard/soft-acid/base principle. Namely, the sulfide (DDT) is a soft base and Cu, Zn, and Al are soft, moderate, and hard acids, respectively.

The Cu:Zn:Al:Sn atomic ratios for **Powder_0**, **Powder_0.25**, **Powder_0.5**, **Powder_0.75**, and **Powder_1** were determined to be 59:22:0:19, 57:17:6:20, 62:9:9:20, 63:5:14:18, and 63:0:19:18, respectively, by scanning electron microscopy/energy-dispersive X-ray spectroscopy (SEM-EDS) analysis, which are approximately equal to the nominal compositions of $Cu_3Zn_{1-x}Al_xSnS_{5-y}$ with $x$ = 0, 0.25, 0.5, 0.75 and 1, respectively. To determine the oxidation states of elements in the nanocrystals, core-level X-ray photoelectron spectroscopy (XPS) analysis of **Powder_1** was performed. Figure 2.7 shows Cu 2p, Al 2p, Sn 3d and S 2p spectra obtained for this sample. The binding energies of Cu $2p_{3/2}$ and Cu $2p_{1/2}$ were 932.2 and 952.1 eV, respectively. The peak separation of 19.9 eV is indicative of the presence of $Cu^{+}$. The peak from Al $2p_{3/2}$ appeared at binding energy of 74.6 eV, which was assigned to $Al^{3+}$. The presence of $Sn^{4+}$ was confirmed by the observation of peaks at 486.4 eV ($3d_{5/2}$) and 494.8 eV ($3d_{3/2}$) with a characteristic peak separation of 8.4 eV. The presence of $S^{2-}$ was confirmed by peaks located at 161.5 eV ($2p_{3/2}$) and 162.6 eV ($2p_{1/2}$) with a peak splitting of 1.1 eV, which was consistent with the literature value for metal sulfides.[22]

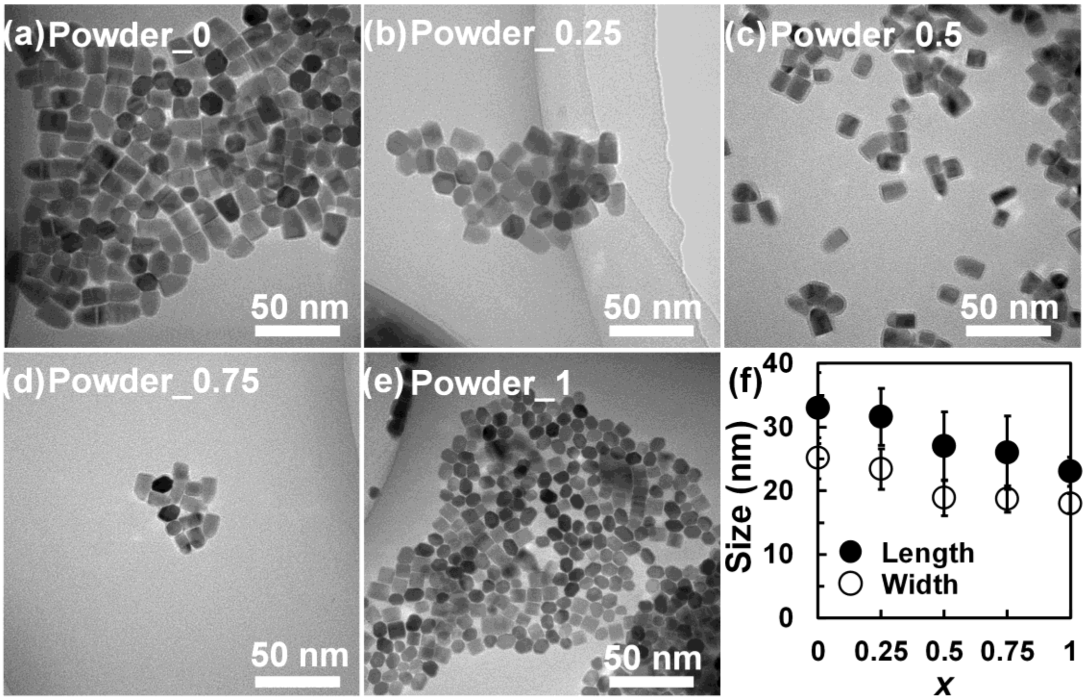

**Figure 2.6.** TEM images of $Cu_3Zn_{1-x}Al_xSnS_{5-y}$ nanocrystals with $x$ of (a) 0, (b) 0.25, (c) 0.5, (d) 0.75, and (e) 1. (f) Average length and width of the nanocrystals plotted as a function of $x$.

**Table 2.2.** Occupancy parameter of each atom in $Cu_3Zn_{1-x}Al_xSnS_{5-y}$ nanocrystals used for crystal structure generation.

| **Sample** | **Occupancy Parameter** | | | | |
|---|---|---|---|---|---|
| | **Cu** | **Zn** | **Al** | **Sn** | **S** |
| **Powder_0** | 0.6 | 0.2 | 0.0 | 0.2 | 1.0 |
| **Powder_0.25** | 0.6 | 0.15 | 0.05 | 0.2 | 1.0 |
| **Powder_0.5** | 0.6 | 0.1 | 0.1 | 0.2 | 1.0 |
| **Powder_0.75** | 0.6 | 0.05 | 0.15 | 0.2 | 1.0 |
| **Powder_1** | 0.6 | 0.0 | 0.2 | 0.2 | 1.0 |

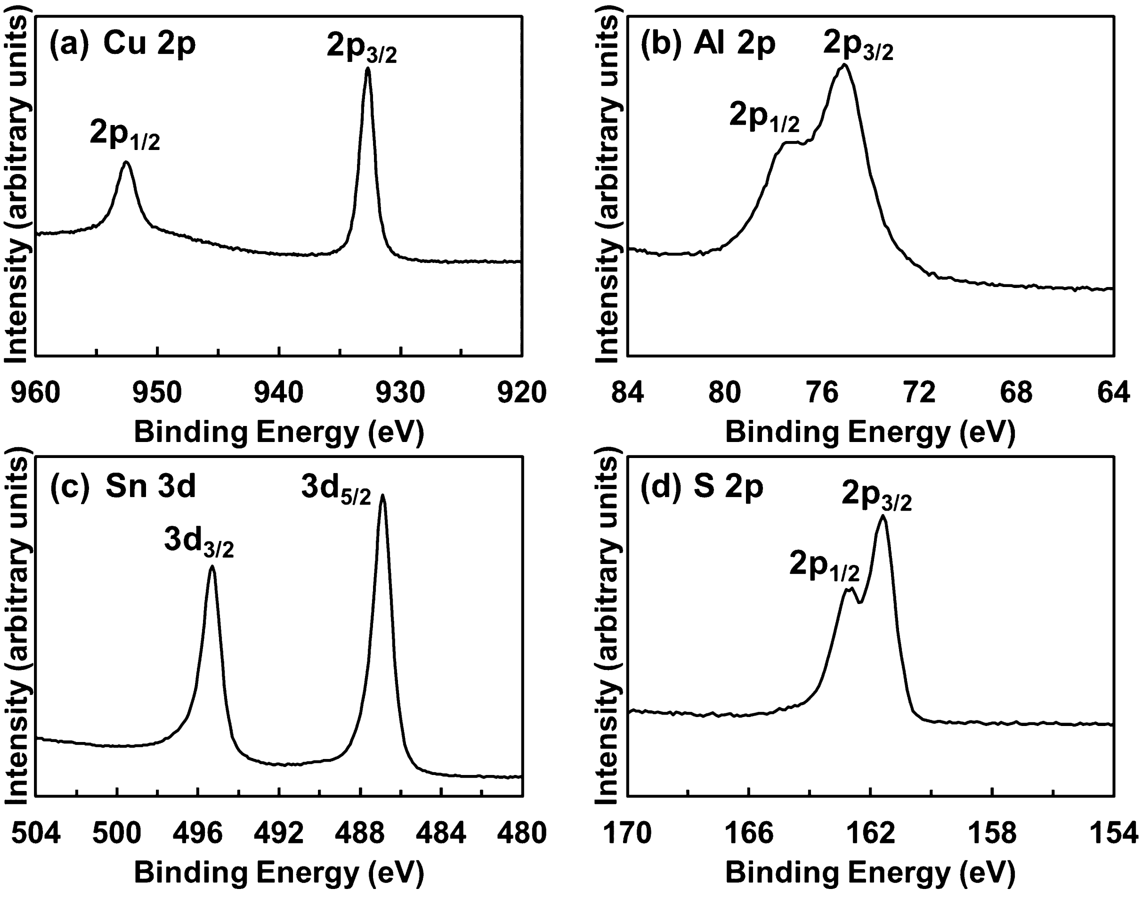

**Figure 2.7.** XPS analysis of $Cu_3AlSnS_5$ nanocrystals: (a) Cu 2p, (b) Al 2p, (c) Sn 3d, and (d) S 2p core-level spectra.

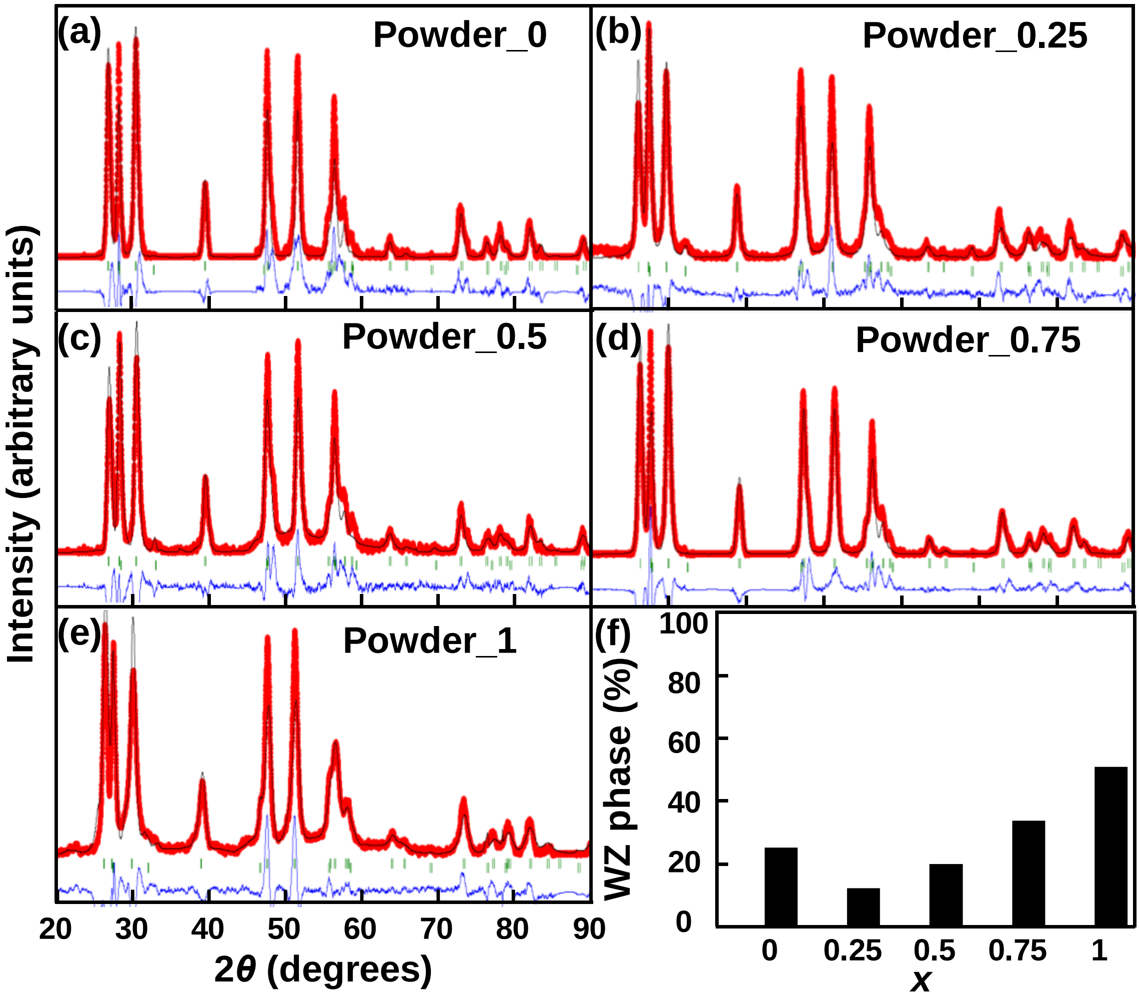

**Figure 2.8.** Rietveld refinement of powder XRD patterns of (a) P**owder_0**, (b) **Powder_0.25**, (c) **Powder_0.5**, (d) **Powder_0.75** and (e) **Powder_1**. The experimental patterns are shown as red lines and the calculated patterns are shown as black lines. The Bragg reflection positions are shown as short green bars below the diffraction patterns. The blue lines represent difference patterns.

**Table 2.3.** WZ and ZB contents of $Cu_3Zn_{1-x}Al_xSnS_{5-y}$ nanocrystals.

| Sample | WZ (wt%) | ZB (wt%) |
|---|---|---|
| **Powder_0** | 96 | 4 |
| **Powder_0.25** | 92 | 8 |
| **Powder_0.5** | 95 | 5 |
| **Powder_0.75** | 97 | 3 |
| **Powder_1** | 98 | 2 |

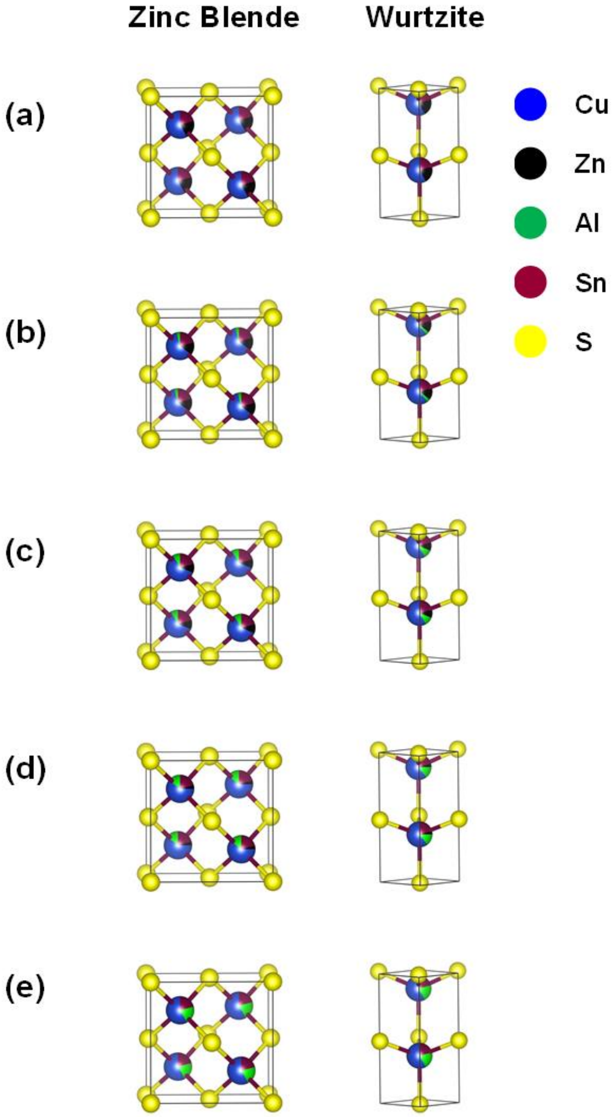

**Figure 2.9.** Crystal structures for (a) **Powder_0**, (b) **Powder_0.25**, (c) **Powder_0.5**, (d) **Powder_0.75**, and (e) **Powder_1** (from top to bottom), which are mixtures of ZB and WZ structures. Blue represents copper, yellow represents sulfur, black represents zinc, green represents aluminum, and brown represents tin.

Figure 2.8 shows the X-ray diffraction (XRD) patterns of **Powder_0**, **Powder_0.5**, and **Powder_1**. The XRD patterns of **Powder_0.25** and **Powder_0.75** are provided in Figure 2.8. Rietveld refinement of the XRD patterns was performed with the FullPROF program[26] using wurtzite (WZ) and zinc blende (ZB) ZnS crystallographic information files.[27] Simulated patterns in which Cu, Sn, and Al ions randomly substitute Zn sites in the ZnS structure are shown as black lines and occupancy parameters are listed in Table 2.2. The crystal structures of powder samples are presented in Figure 2.9.

Rietveld refinement revealed that the primary crystal structure of all nanocrystals was WZ with small amounts of ZB (Table 2.3). The fraction of ZB probably varied because the difference in the oxidation states of $Zn^{2+}$ and $Al^{3+}$ altered the degree of electrostatic interactions in the samples, yielding different crystal structures.[28]

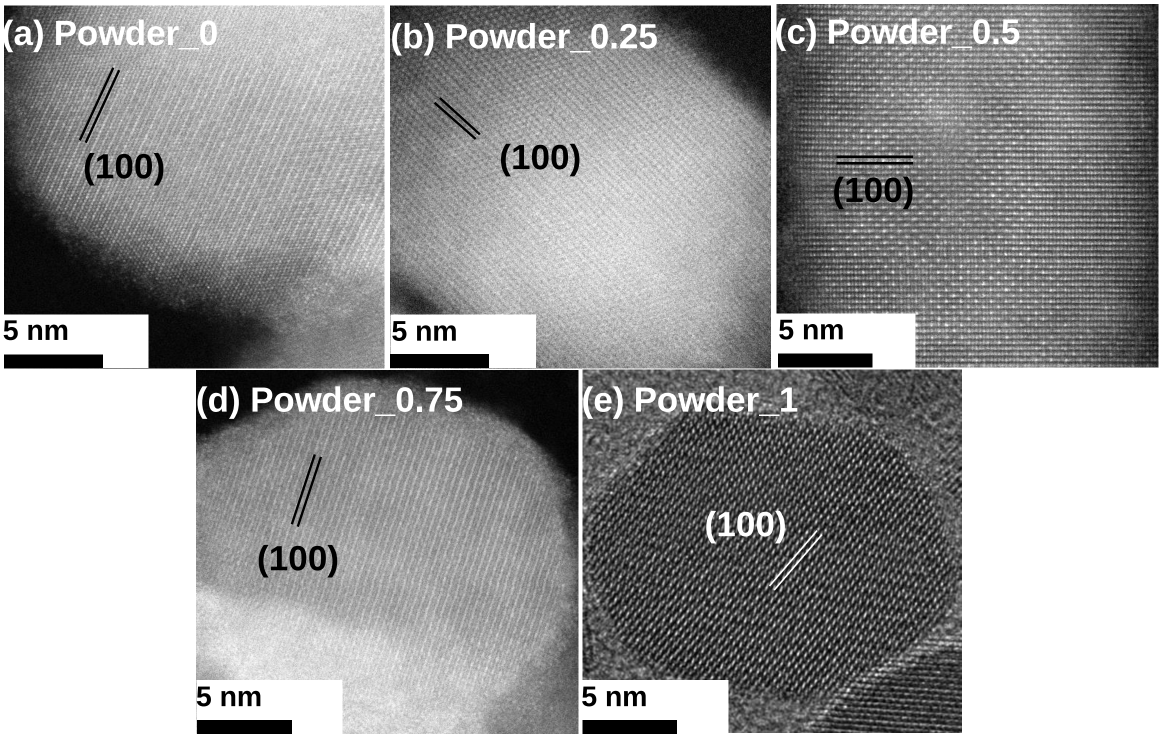

**Figure 2.10.** STEM bright-field images of single $Cu_3Zn_{1-x}Al_xSnS_{5-y}$ nanocrystals with $x$ = (a) 0, (b) 0.25, (c) 0.5, (d) 0.75, and (e) 1. The lattice fringes with an interplanar spacing of 0.33–0.38 nm are ascribed to the {100} planes of WZ.

The mean crystalline size ($D_{\mathrm{xrd}}$) was calculated with the Scherrer equation using the primary peak of the WZ phase. $D_{\mathrm{xrd}}$ calculated for **Powder_0**, **Powder_0.25**, **Powder_0.5**, **Powder_0.75**, and **Powder_1** were 12.6, 12.4, 12.8, 12.4, and 9.1 nm, respectively. The as-synthesized nanocrystals were further analyzed by high-angle annular dark-field scanning transmission electron microscopy (HAADF-STEM), as shown in Figure 2.10. Lattice fringes that were ascribed to the {100} planes of WZ were clearly seen in all cases. To confirm that all elements are within each nanocrystals, EDS elemental mapping was carried out for $Cu_3ZnSnS_{5-y}$, $Cu_3Zn_{0.5}Al_{0.5}SnS_{5-y}$ and $Cu_3AlSnS_5$ nanocrystals as shown in Figure 2.11.

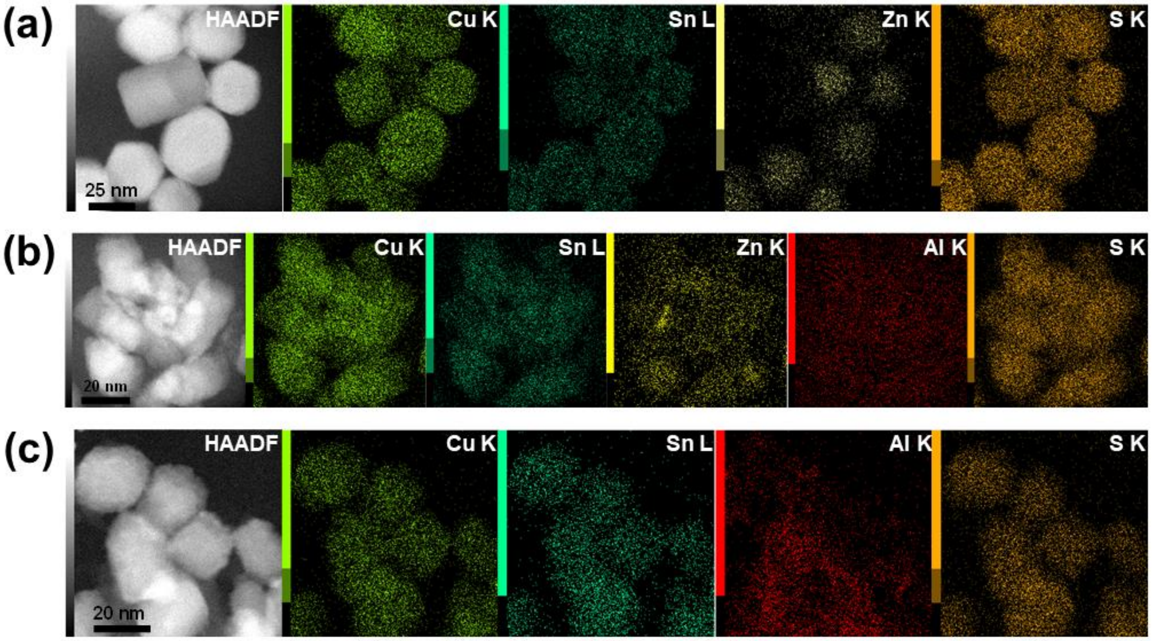

**Figure 2.11** HAADF-STEM and EDS elemental mapping images of (a) $Cu_3ZnSnS_{5-y}$, (b) $Cu_3Zn_{0.5}Al_{0.5}SnS_{5-y}$ nanocrystals.

### *2.4.2 Compositional Analysis*

To know the composition of samples SEM-EDS have been used. The atomic percentage of Cu:Zn:Al:Sn have been summarized in Table 2.4. Pellets were fabricated from the powder samples. The measured Cu:Zn:Al:Sn atomic ratios for **Pellet_0**, **Pellet_0.25**, **Pellet_0.5**, **Pellet_0.75**, and **Pellet_1** were 59:21:0:20, 58:17:7:18, 61:9:9:21, 60:6:16:18, and 61:0:22:17, respectively, which were approximately equal to the nominal compositions of $Cu_3Zn_{1-x}Al_xSnS_{5-y}$ with $x$ = 0, 0.25, 0.5, 0.75, and 1, respectively. The results showed that there is no significant change in the composition after pelletization as well.

**Table 2.4** Atomic compositions for **Powder_0**, **Powder_0.25**, **Powder_0.5**, **Powder_0.75**, **Powder_1** and **Pellet_0**, **Pellet_0.25**, **Pellet_0.5**, **Pellet_0.75** and **Pellet_1** determined using SEM-EDS.

| **Sample** | **SEM-EDS** | | | |
|---|---|---|---|---|
| | **Cu (at %)** | **Zn (at %)** | **Al (at %)** | **Sn (at %)** |
| Powder_0 | 59 | 22 | 0 | 19 |
| Pellet_0 | 59 | 21 | 0 | 20 |
| Powder_0.25 | 57 | 17 | 6 | 20 |
| Pellet_0.25 | 58 | 17 | 7 | 18 |
| Powder_0.5 | 62 | 9 | 9 | 20 |
| Pellet_0.5 | 61 | 9 | 9 | 21 |
| Powder_0.75 | 63 | 5 | 14 | 18 |
| Pellet_0.75 | 60 | 6 | 16 | 18 |
| Powder_1 | 63 | 0 | 19 | 18 |
| Pellet_1 | 61 | 0 | 22 | 17 |

### *2.4.3 Crystal Structure of Pellets*

Figure 2.12 (a–e) show XRD patterns of the pellets. To perform quantitative phase-composition analysis of the pellets, Rietveld refinement of their XRD patterns was performed. Figure 2.12 (f) shows the weight percentage of the WZ phase in each pellet. A phase transition from WZ to ZB was clearly observed for all pellets during sintering. Specifically, **Pellet_0** consisted of a pure ZB phase after sintering. The measured densities of **Pellet_0**, **Pellet_0.25**, **Pellet_0.5**, **Pellet_0.75**, and **Pellet_1** were 4.522, 4.531, 4.518, 4.544, and 4.356 g·cm$^{-3}$, respectively. Thus, the relative densities of all pellets were higher than 95%.

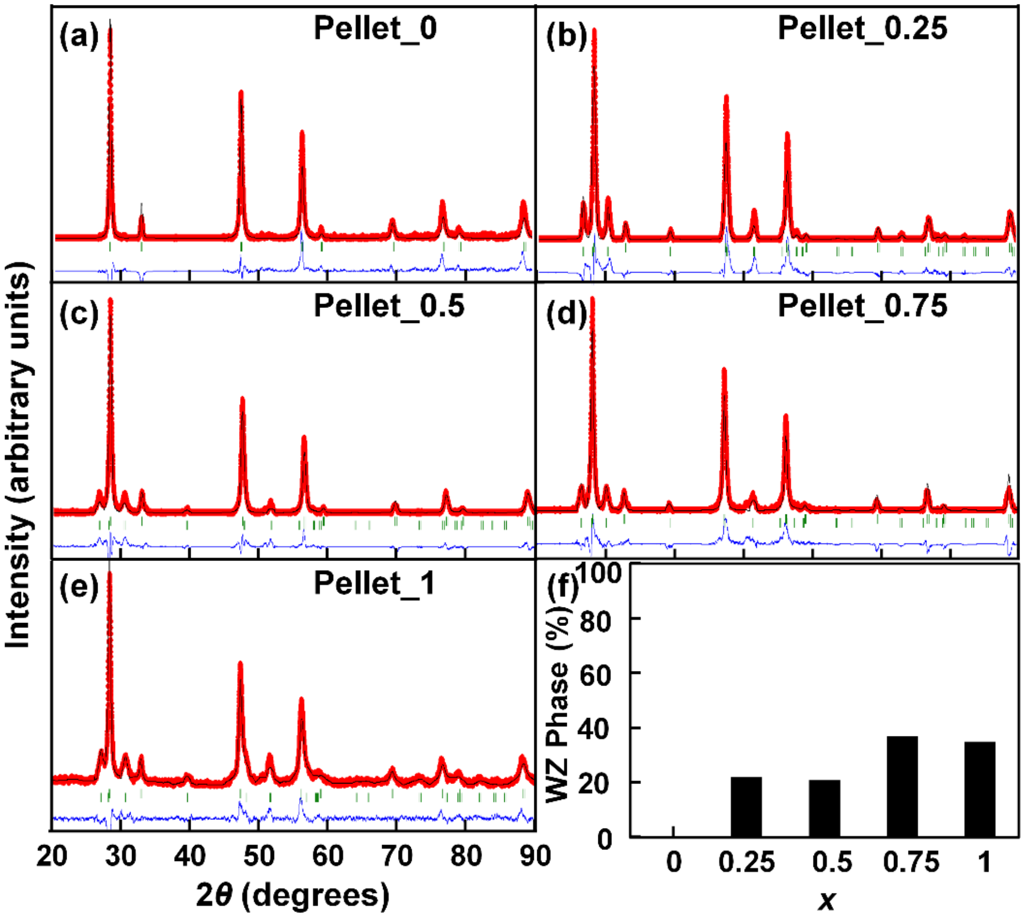

**Figure 2.12** Rietveld refinement of powder XRD patterns of (a) **Pellet_0**, (b) **Pellet_0.25**, (c) **Pellet_0.5**, (d) **Pellet_0.75**, and (e) **Pellet_1**. Experimental and calculated patterns are shown as red and black lines, respectively. (f) Weight percentage of WZ plotted as a function of *x*.

The phase transition was ascribed to the greater thermodynamic stability of the ZB phase than that of WZ phase because of the more symmetrical structure of the former, which might increase with the Zn content and thereby facilitate the phase transition. The lattice constants of ZB phase are plotted as a function of $x$ in Figure 2.13. The calculated $D_{xrd}$ values of **Pellet_0**, **Pellet_0.25**, **Pellet_0.5**, **Pellet_0.75**, and **Pellet_1** were 22.7, 20.2, 21.5, 17.7, and 19.8 nm, respectively, indicating that $D_{xrd}$ slightly increased during sintering for all the pellets.

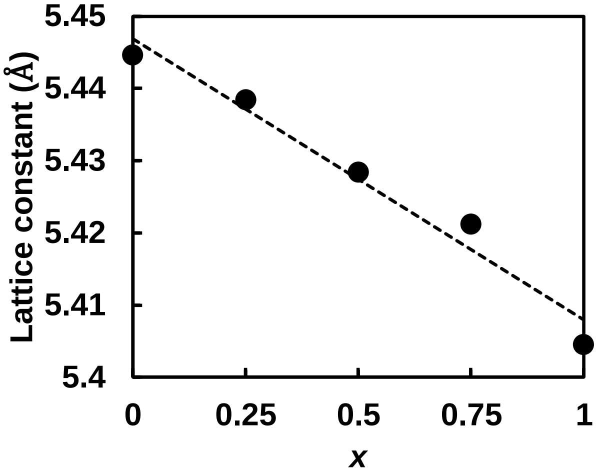

**Figure 2.13.** Lattice constants for the ZB phase of $Cu_3Zn_{1-x}Al_xSnS_{5-y}$ pellets plotted as a function of $x$.

### 2.4.4 Thermoelectric Properties

Thermal diffusivities and specific heats for all pellets are provided in Figure 2.14. Figure 2.15 shows the thermoelectric properties of **Pellet_0**, **Pellet_0.25**, **Pellet_0.5**, **Pellet_0.75**, and **Pellet_1**. It should be noted that we measured $S$ and $\sigma$ in both heating and cooling cycles and found that the values coincided in both types of cycles (Figure 2.16). As shown in Figure 2.15a, $\sigma$ decreases with temperature, indicating the metallic behavior of the pellets. It is noteworthy that the $\sigma$ values of **Pellet_1** are an order of magnitude higher than those of the other pellets as well as those of other high-performance copper sulfide-based thermoelectric materials including $Cu_{1.97}S$,[29] $Cu_{10}Ni_2Sb_4S_{13}$,[30] and $Cu_{26}V_2Sn_6S_{32}$.[31]

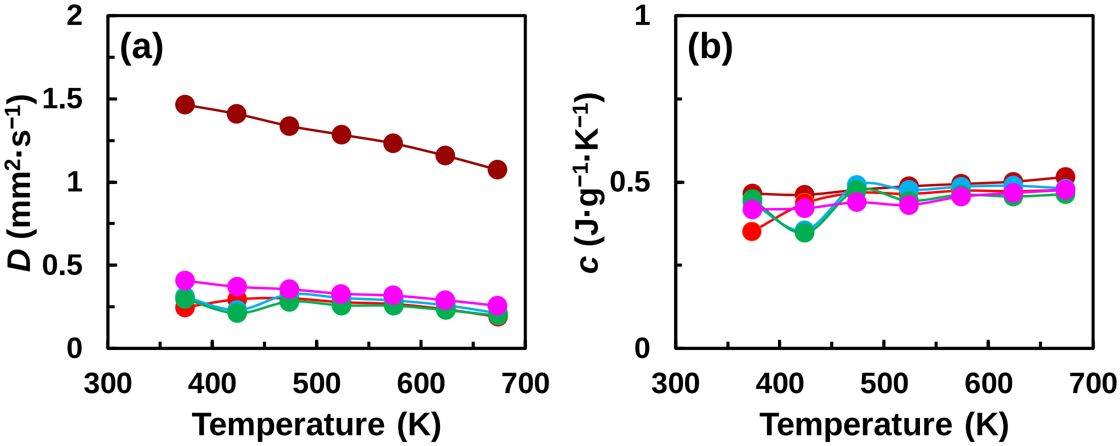

**Figure 2.14** (a) Thermal diffusivities *D* ($mm^2 \cdot s^{-1}$) and (b) specific heats *c* ($J \cdot g^{-1} \cdot K^{-1}$) of **Pellet_0** (pink circles), **Pellet_0.25** (red circles), **Pellet_0.5** (blue circles), **Pellet_0.75** (green circles), and **Pellet_1** (brown circles).

It is interesting to compare the thermoelectric properties of our samples with those of reported CZTS materials[8] (Figure 2.15) Cu-doped CZTS ($Cu_{2.19}Zn_{0.80}Sn_{0.75}S_{3.53}$) exhibited a $\sigma$ value that was 38 times higher than that of undoped CZTS at 700 K (Figure 2.15 (a)). The atomic fraction of Cu in our pellet samples was higher than that in Cu-doped CZTS, and the $\sigma$ values of our pellets were much higher than that of Cu-doped CZTS, as shown in Figure 2.15 (a).

Figure 2.15 (b) illustrates the temperature dependence of *S*. In general, *S* depends inversely on $\sigma$. However, the *S* values of **Pellet_0**, **Pellet_0.25**, **Pellet_0.5**, and **Pellet_0.75** are approximately the same as that of Cu-doped CZTS, even though the $\sigma$ values of these pellets are much higher than that of Cu-doped CZTS, resulting in our pellets displaying much higher *PF* values than those of CZTS materials. Though it is not appropriate to directly compare the electrical transport properties of the $Cu_3Zn_{1-x}Al_xSnS_{5-y}$ materials, which are $I_3$–II/III–IV–$VI_5$ semiconductors with ZB structure, with those of conventional CZTS materials, which are $I_2$–II–IV–$VI_4$ semiconductors with tetragonal crystal structure, we would like to emphasize that the electrical transport properties of $Cu_3Zn_{1-x}Al_xSnS_{5-y}$ materials differ markedly from those of CZTS materials.

Figure 2.15 (c) displays the temperature dependence of $\kappa$. The $\kappa$ values are quite low for all pellets except for **Pellet_1** and $\kappa$ shows almost no temperature dependence. This is more evident in Figure 2.15 (c) and (d), where $\kappa_{\mathrm{lat}}$ of undoped CZTS exhibits the classical $1/T$ dependence caused by Umklapp scattering, whereas the characteristic $1/T$ dependence of $\kappa_{\mathrm{lat}}$ completely disappeared for the $Cu_3Zn_{1-x}Al_xSnS_{5-y}$ materials, indicating that the phonon scattering is dominated by defect scattering including nanograins and lattice distortion. In addition, the $\kappa_{\mathrm{lat}}$ values decreased with increasing $x$, as expected. The reason for the disappearance of the $1/T$ dependence of $\kappa_{\mathrm{lat}}$ in the case of Cu-doped CZTS has been explained by lattice distortion generated by excess Cu dopants occupying Zn positions in the lattice.[8]

Figure 2.15 (e) and (f) show the temperature dependences of $PF$ and $ZT$ values, respectively. **Pellet_0** and **Pellet_0.5** exhibited $ZT$ values of 0.39 (at 658 K) and 0.40 (at 666 K), respectively; these values are approximately 15 and 3 times higher than the $ZT$ values (at 700 K) of undoped and Cu-doped CZTS materials,[8] respectively. The $ZT$ value of **Pellet_1** was only 0.12 (at 668 K), which was mainly because **Pellet_1** had a high $\sigma$, resulting in the high carrier thermal conductivity ($\kappa_{\mathrm{car}}$) (Figure 2.17).

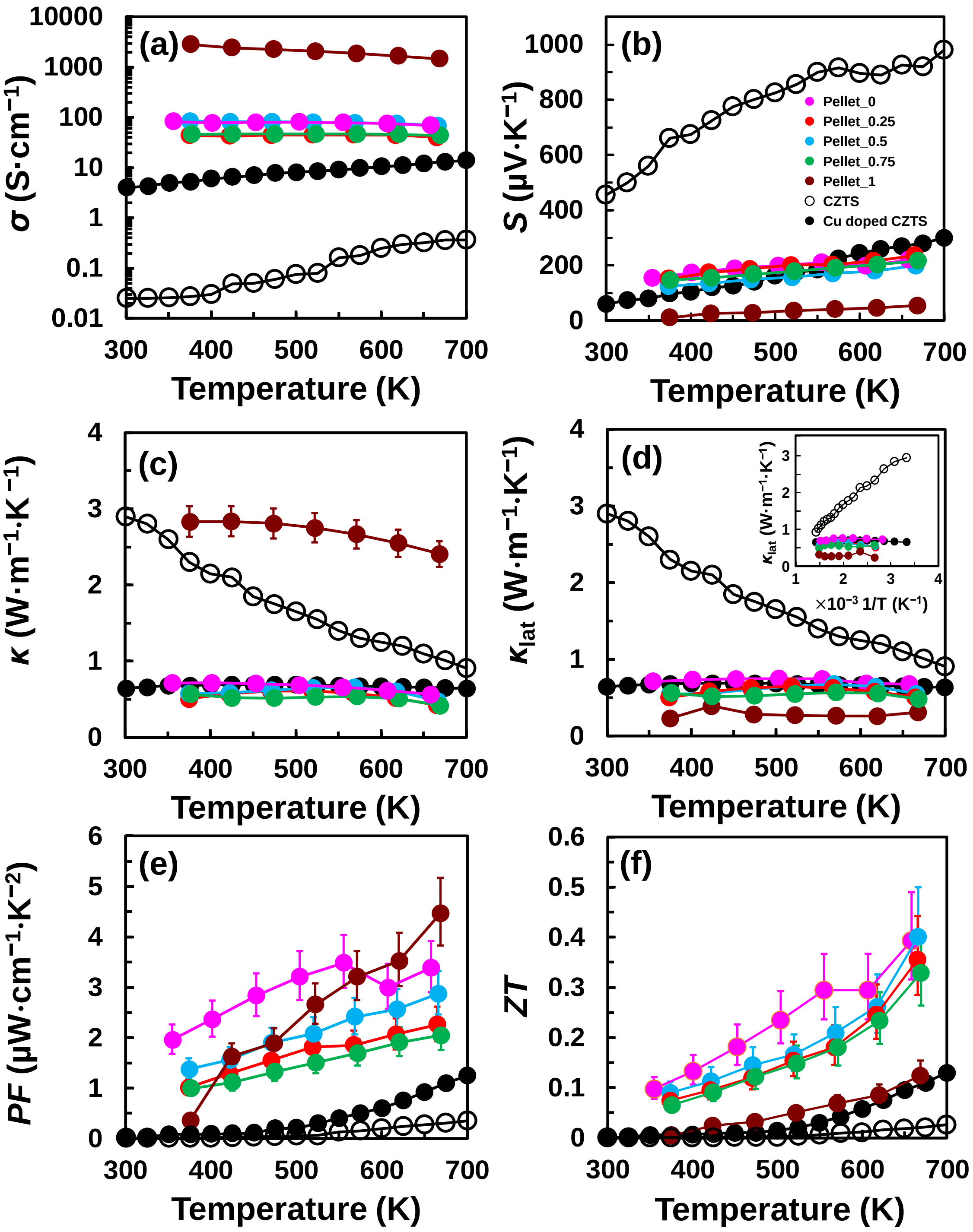

**Figure 2.15** (a) $\sigma$, (b) $S$, (c) $\kappa$, (d) $\kappa_{\mathrm{lat}}$, (e) $PF$, and (f) $ZT$ values of **Pellet_0** (filled pink circles), **Pellet_0.25** (filled red circles), **Pellet_0.5** (filled blue circles), **Pellet_0.75** (filled green circles), **Pellet_1** (filled brown circles), undoped CZTS (unfilled black circles),[8] and Cu-doped CZTS (filled black circles).[8] The inset of (d) shows $\kappa_{\mathrm{lat}}$ plotted with respect to the reciprocal of temperature.

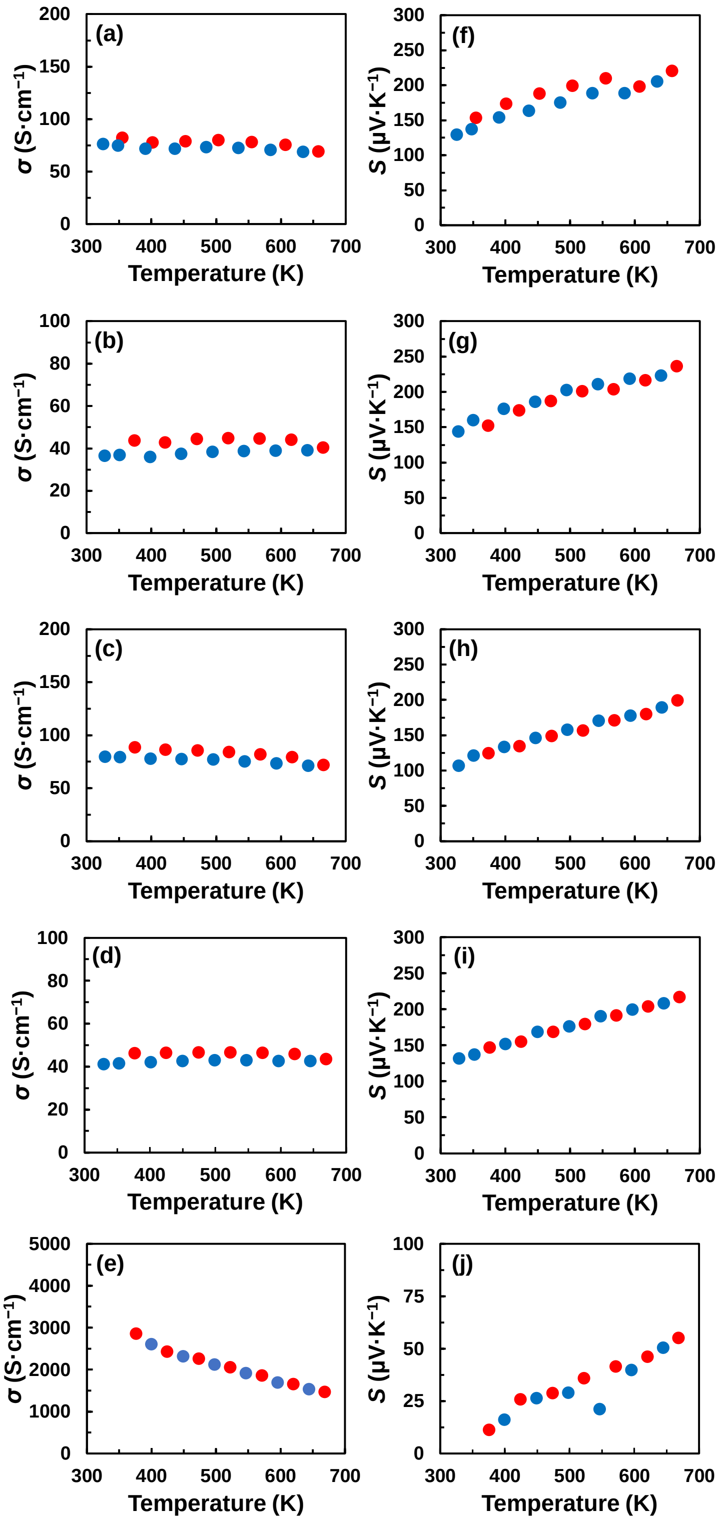

**Figure 2.16** (a), (b), (c), (d), and (e) Electrical conductivities ($\sigma$) and (f), (g), (h), (i), and (j) Seebeck coefficients ($S$) of **Pellet_0**, **Pellet_0.25**, **Pellet_0.5**, **Pellet_0.75**, and **Pellet_1**, respectively. Red and blue circles represent data measured in heating and cooling cycles, respectively.

Therefore, there is a high possibility of improvement of the *ZT* value of CATS materials by lowering $\sigma$ to decrease $\kappa_{\mathrm{car}}$, because $\kappa_{\mathrm{lat}}$ of CATS is already quite low (~0.3 W $\mathrm{m^{-1}\ K^{-1}}$), as shown in Figure 2.15 (d). The decrease of $\sigma$ can be achieved in several ways; for example, incorporating nanoinclusions in the material to scatter carriers or decreasing the size of nanocrystals.

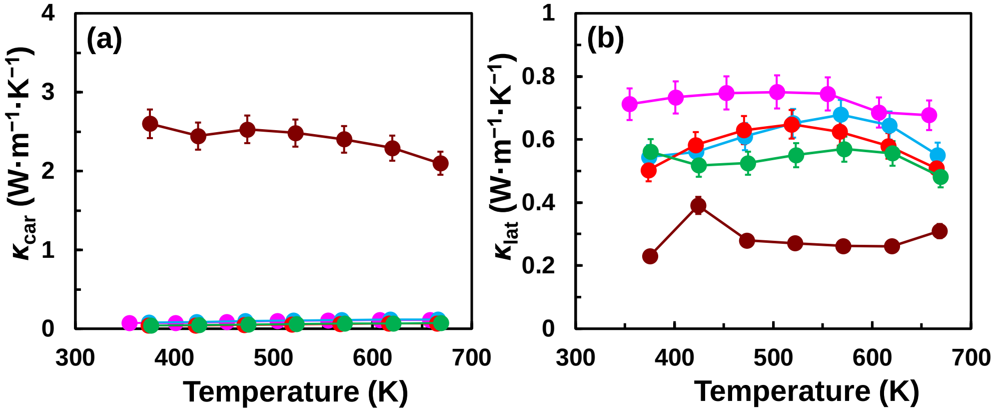

**Figure 2.17.** (a) $\kappa_{\mathrm{car}}$ and (b) $\kappa_{\mathrm{lat}}$ of **Pellet_0** (filled pink circles), **Pellet_0.25** (filled red circles), **Pellet_0.5** (filled blue circles), **Pellet_0.75** (filled green circles) and of **Pellet_1** (filled brown circles).

**Pellet_0** ($\mathrm{Cu_3ZnSnS_{5-\mathit{y}}}$) consisted of a pure ZB phase accompanied with high *S* compared to those of metals and high $\sigma$ compared to those of intrinsic semiconductors, implying that **Pellet_0** is a degenerate semiconductor. In contrast, **Pellet_0.25**, **Pellet_0.5**, **Pellet_0.75**, and **Pellet_1** consisted of mixtures of ZB and WZ phases. The weight percentage of the WZ phase increased with Al content, as shown in Figure 2.12 (f). The *S* and $\sigma$ values of the pellets at 375 and 650 K are summarized in Table 2.5 as well as the weight percentages of ZB and WZ phases of all pellets. Both *S* and $\sigma$ exhibited complex behavior with respect to *x*, indicating that the fraction of ZB phase has a noticeable effect on the electrical transport properties of the pellets.

**Table 2.5** $S$, $\sigma$, and contents of ZB and WZ phases of pellets.

| **Sample** | **at 375 K** | | **at 650 K** | | **ZB (wt%)** | **WZ (wt%)** |
|---|---|---|---|---|---|---|
| | **$S$ (μV·K$^{-1}$)** | **$\sigma$ (S·cm$^{-1}$)** | **$S$ (μV·K$^{-1}$)** | **$\sigma$ (S·cm$^{-1}$)** | | |
| **Pellet_0** | 164 | 81 | 214 | 71 | 100 | 0 |
| **Pellet_0.25** | 156 | 43 | 229 | 42 | 78 | 22 |
| **Pellet_0.5** | 125 | 88 | 193 | 75 | 79 | 21 |
| **Pellet_0.75** | 146 | 46 | 212 | 45 | 63 | 37 |
| **Pellet_1** | 14 | 2801 | 51 | 1548 | 65 | 35 |

Even though the amount of data was insufficient, one could argue that the carrier concentration of $Cu_3Zn_{1-x}Al_xSnS_{5-y}$ materials seems to increase with Al content if one compares the characteristics of **Pellet_0.25** and **Pellet_0.5** or **Pellet_0.75** and **Pellet_1**, which have similar weight percentages of the ZB phase (Table 2.5). To confirm this hypothesis, based on the free electron model, Fermi energy $E_F$ can be described as

$$E_{\mathrm{F}} = \frac{\hbar^2 {k_{\mathrm{F}}}^2}{2m} \tag{2.1}$$

where $\hbar$ is the Dirac constant, $k_F = (3\pi^2 n)^{1/3}$ is the wave number at the Fermi surface, and $n$ is the carrier concentration. We assumed that an acoustic phonon scattering of carriers is dominant at high temperature region. According to this assumption, $S$ can be described as below,

$$\sigma = A\varepsilon^{\gamma} \tag{2.2}$$

$$S = -\frac{\pi^2 {k_{\mathrm{B}}}^2 T}{3e} \frac{\mathrm{d}\ln\sigma}{\mathrm{d}\varepsilon}\bigg|_{\varepsilon = E_{\mathrm{F}}} = \frac{\pi^2 {k_{\mathrm{B}}}^2}{6eE_{\mathrm{F}}} T \tag{2.3}$$

where $A$ is the arbitrary constant, $\varepsilon$ is the energy, $\gamma$ is the scattering parameter, $k_B$ is the Boltzmann constant, and $e$ is the elementary charge. When the carrier scattering is dominated by acoustic phonon scattering, $\gamma = -1/2$. From Eqs. (2.1)−(2.3), the values of $n$ and mobility ($\mu$) were estimated as shown in Table 2.6.

**Table 2.6** $n$ and $\mu$ estimated from the values of $S$ and $\sigma$ (at 375 K).

| **Sample** | **$S$ (μV·K$^{-1}$)** | **$\sigma$ (S·cm$^{-1}$)** | **$n$ (cm$^{-3}$)** | **$\mu$ (cm$^{2}$·V$^{-1}$·s$^{-1}$)** |
|---|---|---|---|---|
| **Pellet_0** | 164 | 81 | $2.1 \times 10^{19}$ | 24 |
| **Pellet_0.25** | 156 | 43 | $2.3 \times 10^{19}$ | 12 |
| **Pellet_0.5** | 125 | 88 | $3.2 \times 10^{19}$ | 17 |
| **Pellet_0.75** | 146 | 46 | $2.5 \times 10^{19}$ | 11 |
| **Pellet_1** | 14 | 2801 | $8.5 \times 10^{20}$ | 21 |

The value of $\mu$ are low for all pellets as compared to typical semiconductors probably due to the defect scattering. These results create opportunity for finer tuning of the material physical properties contributing towards better understanding of their thermoelectric performances.

## 2.5. Conclusions

A novel series of thermoelectric materials was chemically synthesized with earth-abundant and eco-friendly elements. Incorporation of Al in the Cu-Zn-Sn-S system decreased $\kappa_{\mathrm{lat}}$ by about 4 times and enhanced $\sigma$ by an order of magnitude at most. In consequence, $Cu_3Zn_{1-x}Al_xSnS_{5-y}$ ($x$ = 0 and 0.5) materials exhibited $ZT$ values of 0.39 (at 658 K) and 0.40 (at 666 K), respectively, which are approximately 15 times higher than that of conventional CZTS. It was challenging to determine the most important factor to control the $ZT$ value because incorporation of Al not only changed the material stoichiometry but also the phase fraction and crystal structure and their dependent parameters. This research contributes to the development of Cu-Zn/Al-Sn-S-based semiconductors as sustainable thermoelectric materials and creates space for further development of a profound understanding of transport properties and $ZT$ values without sacrificing sustainability.

# References

(1) Vineis, C. J.; Shakaouri, A.; Majumdar, A.; Kanatzidis, M. G. Nanostructured Thermoelectrics: Big Efficiency Gains from Small Features. *Adv. Mater*. **2010**, *22*, 3970-3980.

(2) Lan, Y.; Minnich, A. J.; Chen, G.; Ren, Z. Enhancement of Thermoelectric Figure-of-Merit by a Bulk Nanostructuring Approach. *Adv. Funct. Mater*. **2010**, *20*, 357-376.

(3) Dmitriev, A. V.; Zvyagin, I. P. Current Trends in the Physics of Thermoelectric Materials. *Physics-Uspekhi* **2010**, *53*, 789-803.

(4) Poudel, B.; Hao, Q.; Ma, Y.; Lan, Y.; Minnich, A.; Yu, B.; Yan, X.; Wang, D.; Muto, A.; Vashaee, D.; Chen, X.; Liu, J.; Dresselhaus, M. S.; Chen, G.; Ren, Z. High-Thermoelectric Performance of Nanostructured Bismuth Antimony Telluride Bulk Alloys. *Science* **2008**, *320*, 634-638.

(5) Joshi, G.; Lee, H.; Lan, Y.; Wang, X.; Zhu, G.; Wang, D.; Gould, R. W.; Cuff, D. C.; Tang, M. Y.; Dresselhaus, M. S.; Chen, G.; Ren, Z. Enhanced Thermoelectric Figure-of-Merit in Nanostructured p-type Silicon Germanium Bulk Alloys. *Nano Lett*. **2008**, *8* (12), 4670-4674.

(6) Kanatzidis, M. G. Nanostructured Thermoelectrics: The New Paradigm? *Chem. Mater*. **2010**, *22*, 648-659.

(7) Liu, M. L.; Huang, F. Q.; Chen, L. D.; Chen, I. W. A Wide-band-gap p-type Thermoelectric Material based on Quaternary Chalcogenides of $Cu_2ZnSnQ_4$ (Q = S, Se). *Appl. Phys. Lett*. **2009**, *94*, 202103.

(8) Yang, H.; Jauregui, L. A.; Zhang, G.; Chen, Y. P.; Wu, Y. Nontoxic and Abundant Copper Zinc Tin Sulfide Nanocrystals for Potential High-Temperature Thermoelectric Energy Harvesting. *Nano Lett*. **2012**, *12*, 540-545.

(9) Zheng, X.; Liu, Y.; Du, Y.; Sun, Y.; Li, J.; Zhang, R.; Li, Q.; Chen, P.; Zhao, G.; Fang, Y.; Dai, N. P-type Quaternary Chalcogenides of $Cu_2ZnSn(S,Se)_4$ Nanocrystals: Large-scale Synthesis, Band Gap Engineering and Their Thermoelectric Performances. *J. Alloy. Compd.* **2018**, *738*, 484-490.

(10) Shavel, A.; Cadavid, D.; Ibanez, M.; Carrete, A.; Cabot, A. Continuous Production of $Cu_2ZnSnS_4$ Nanocrystals in a Flow Reactor. *J. Am. Chem. Soc*. **2012**, *134*, 1438-1441.

(11) Isotta, E.; Fanciulli, C.; Pugno, N. M.; Scardi, P. Effect of the Order-Disorder Transition on the Seebeck Coefficient of Nanostructured Thermoelectric $Cu_2ZnSnS_4$. *Nanomaterials* **2019**, *9*, 762.

(12) Jain, S.; Chawla, P.; Sharma, S. N.; Singh, D.; Vijayan, N. Efficient Colloidal Route to Pure Phase Kesterite $Cu_2ZnSnS_4$ (CZTS) Nanocrystals with Controlled Shape and Structure. *Superlattices Microstruct.* **2018**, *119*, 59-71.

(13) Dong, Y.; Wang, H.; Nolas, G. S. Synthesis and Thermoelectric Properties of Cu Excess $Cu_2ZnSnSe_4$. *Phys. Status Solidi: Rapid Res. Lett*. **2014**, *8* (1), 61-64.

(14) Song, Q.; Qiu, P.; Hao, F.; Zhao, K.; Zhang, T.; Ren, D.; Shi, X.; Chen, L. Quaternary Pseudocubic $Cu_2TMSnSe_4$ (TM = Mn, Fe, Co) Chalcopyrite Thermoelectric Materials. *Adv. Electron. Mater*. **2016**, *2*, 1600312.

(15) Ibáñez, M.; Cadavid, D.; Zamani, R.; García-Castelló, N.; Izquierdo-Roca, V.; Li, W.; Fairbrother, A.; Prades, J. D.; Shavel, A.; Arbiol, J.; Pérez-Rodríguez, A.; Morante, J. R.;

Cabot, A. Composition Control and Thermoelectric Properties of Quaternary Chalcogenide Nanocrystals: The Case of Stannite $Cu_2CdSnSe_4$. *Chem. Mater*. **2012**, *24*, 562-570.

(16) Song, Q.; Qiu, P.; Chen, H.; Zhao, K.; Ren, D.; Shi, X.; Chen, L. Improved Thermoelectric Performance in Non-stoichiometric $Cu_{2+\delta}Mn_{1-\delta}SnSe_4$ Quaternary Diamond-like Compounds. *ACS Appl. Mater. Interf*. **2018**, *10*, 10123-10131.

(17) Ibáñez, M.; Zamani, R.; Lalonde, A.; Cadavid, D.; Li, W.; Shavel, A.; Arbiol, J.; Morante, J. R.; Gorsse, S.; Snyder, G. J.; Cabot, A. $Cu_2ZnGeSe_4$ Nanocrystals: Synthesis and Thermoelectric Properties. *J. Am. Chem. Soc*. **2012**, *134*, 4060-4063.

(18) Zeier, W. G.; Lalonde, A.; Gibbs, Z. M.; Heinrich, C. P.; Panthöfer, M.; Snyder, G. J.; Tremel, W. Influence of a Nano Phase Segregation on the Thermoelectric Properties of the p-Type Doped Stannite Compound $Cu_{2+x}Zn_{1-x}GeSe_4$. *J. Am. Chem. Soc*. **2012**, *134,* 7147-7154.

(19) Zhou, W.; Shijimaya, C.; Takahashi, M.; Miyata, M.; Mott, D.; Koyano, M.; Ohta, M.; Akatsuka, T.; Ono, H.; Maenosono, S. Sustainable Thermoelectric Materials Fabricated by using $Cu_2Sn_{1-x}Zn_xS_3$ Nanoparticles as Building Blocks. *Appl. Phys. Lett*. **2017**, *111*, 263105.

(20) Zhou, W.; Dwivedi, P.; Shijimaya, C.; Ito, M.; Higashimine, K.; Nakada, T.; Takahashi, M.; Mott, D.; Miyata, M.; Ohta, M.; Miwa, H.; Akatsuka, T.; Maenosono, S. Enhancement of the Thermoelectric Figure of Merit in Blended $Cu_2Sn_{1-x}Zn_xS_3$ Nanobulk Materials. *ACS Appl. Nano Mater*. **2018**, *1* (9), 4819-4827.

(21) Cui, Y.; Wang, G.; Pan, D. Colloidal Synthesis and Optical Properties of Metastable Wurtzite $I_3$-III-IV-$VI_5$ ($Cu_3InSnS_5$) Nanocrystals. *CrystEngComm*. **2013**, *15*, 10459-10463.

(22) Bai, T.; Xing, S.; Lou, Y.; Chen, C.; Huang, H.; Li, C.; Shi, Z.; Feng, S. Colloidal Synthesis of Quaternary Wurtzite $Cu_3AlSnS_5$ Nanocrystals and Their Photoresponsive Properties. *ChemPlusChem* **2015**, *80*, 652-655.

(23) Li, W.; Zhou, C.; Li, L. A First-Principles Theoretical Study on the Thermoelectric Properties of the Compound $Cu_5AlSn_2S_8$. *J. Electronic Mater*. **2015**, *45* (3), 1453-1458.

(24) Thanh, N. T. K.; Maclean, N.; Mahiddine, S. Mechanisms of Nucleation and Growth of Nanoparticles in Solution. *Chem. Rev*. **2014**, *114*, 7610-7630.

(25) Chen, L.; Li, G. Functions of 1-Dodecanethiol in the Synthesis and Post-Treatment of Copper Sulfide Nanoparticles Relevant to Their Photocatalytic Applications. *ACS Appl. Nano Mater*. **2018**, *19*, 4587-4593.

(26) Rodriguez, J. C. Recent Advances in Magnetic Structure Determination by Neutron Powder Diffraction. *Phys. B* **1993**, *192*, 55-69.

(27) http://www.crystallography.net/cod/ (accessed on March 6, 2019).

(28) Brown, I. D. Recent Developments in the Methods and Applications of the Bond Valence Model, *Chem. Rev*. **2009**, *109*, 6858-6919.

(29) He, Y.; Day, T.; Zhang, T.; Liu, H.; Shi, X.; Chen, L.; Snyder, G. J. High Thermoelectric Performance in Non-Toxic Earth-Abundant Copper Sulfide. *Adv. Mater*. **2014**, *26*, 3974-3978.

(30) Suekuni, K.; Tsuruta, K.; Kunii, M.; Nishiate, H.; Nishibori, E.; Maki, S.; Ohta, M.; Yamamoto, A.; Koyano, M. High-performance Thermoelectric Mineral $Cu_{12-x}Ni_xSb_4S_{13}$ Tetrahedrite. *J. Appl. Phys*. **2013**, *113*, 043712.

(31) Suekuni, K.; Kim, F. S.; Nishiate, H.; Ohta, M.; Tanaka, H. I.; Takabatake, T. High-performance Thermoelectric Minerals: Colusites $Cu_{26}V_2M_6S_{32}$ (M = Ge, Sn). *Appl. Phys. Lett*. **2014,** *105*, 132107.

# Chapter 3

## Effect of Gallium Substitution in $Cu_3Al_{1-x}Ga_xSnS_5$ Nanobulk Materials on Thermoelectric Properties

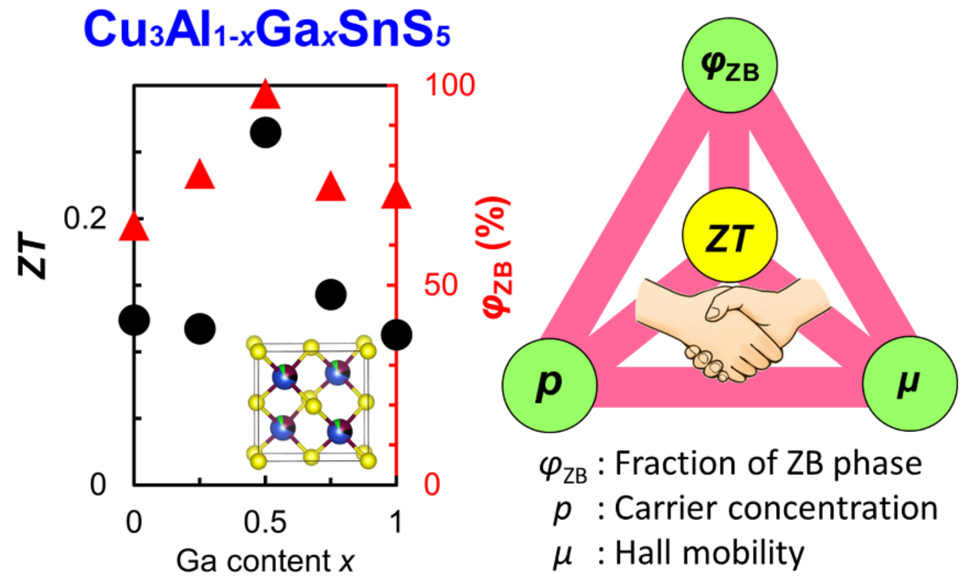

## 3.1 Introduction

Thermoelectric (TE) materials can be used to generate electricity from a temperature gradient to effectively recycle the abundant waste heat. The performance of TE materials can be rated through the dimensionless figure of merit, $ZT = \sigma S^2 T/(\kappa_{\mathrm{lat}}+\kappa_{\mathrm{car}})$, where $\sigma$, $S$, $\kappa_{\mathrm{lat}}$, $\kappa_{\mathrm{car}}$ and $T$ are the electrical conductivity, Seebeck coefficient, lattice thermal conductivity, carrier thermal conductivity and absolute temperature, respectively. The improvement of the $ZT$ value is a pressing issue for TE materials research. To improve the $ZT$ value, it is important to increase the power factor (PF = $\sigma S^2$) and/or decrease the total thermal conductivity, $\kappa = \kappa_{\mathrm{lat}}+\kappa_{\mathrm{car}}$. In nanostructured materials, $\kappa$ can be decreased considerably by lowering $\kappa_{\mathrm{lat}}$ through phonon scattering at grain boundaries,[1-4] whereas the PF can be enhanced by several methods such as quantum confinement or energy filtering.[5] The physical methodologies adopted for TE material synthesis are often energy- and time-consuming, however, which creates difficulties in the practical production of TE materials.[6] Furthermore, high-performance TE materials are primarily composed of relatively rare and/or toxic elements,[7-9] making them questionable in terms of sustainability. To explore more sustainable high-performance TE materials, it is important to develop a scalable synthetic methodology for the fabrication of TE materials consisting of earth-abundant and eco-friendly elements.

With these points in mind, Cu-M-Sn-S (M = metal) quaternary TE materials have recently been regarded as suitable candidates. Among these sulfide TE materials, the Cu-Al-Sn-S system has been predicted to possess a low $\kappa_{\mathrm{lat}}$ value based on the *ab initio* calculation that suggests that the incorporation of a Group IIIA element into the I-IV-VI system will significantly reduce the $\kappa_{\mathrm{lat}}$ via effective phonon scattering owing to its complex crystal structure.[10] Recently, we fabricated a $Cu_3AlSnS_5$ (CATS) nanobulk TE material using chemically-synthesized CATS nanocrystals and succeeded in achieving a $\kappa_{\mathrm{lat}}$ lower than that exhibited by other Cu-M-Sn-S systems.[11] We also fabricated $Cu_3Zn_{1-x}Al_xSnS_{5-y}$ ($x = 0$, 0.25, 0.5 and 0.75) nanobulk materials by replacing Al with Zn in CATS. It was found that the $ZT$ value of $Cu_3ZnSnS_{5-y}$ exhibited a threefold increase over that of CATS.[11] Even though the $ZT$ value of CATS was found to be nearly one third of that of $Cu_3ZnSnS_{5-y}$, CATS interestingly exhibited the lowest $\kappa_{lat}$ and the highest $\sigma$ among $Cu_3Zn_{1-x}Al_xSnS_{5-y}$ ($x = 0-1$) nanobulk materials. The introduction of Al into the Cu-Sn-S system led to a considerable increase in $\sigma$, which resulted in a high $\kappa_{car}$.[11] Therefore, the $\kappa$ value of CATS is quite high even though it has an ultra-low $\kappa_{lat}$, and the $ZT$ value of CATS remains low. If it is possible to reduce the $\kappa_{car}$ of CATS while maintaining its relatively high PF and ultra-low $\kappa_{lat}$ values by tuning the carrier concentration, CATS deserves to be revisited as a promising sustainable TE material.

Several researchers have attempted to modulate the $\sigma$ by elemental substitution reactions in the chalcogenide materials.[12-14] In present case, one of the strategy to reduce $\kappa_{car}$ while maintaining ultra-low $\kappa_{lat}$ is the incorporation of another Group IIIA element into CATS to inherently lower the $\sigma$ without any harmful effects to the $\kappa_{lat}$ value. The replacement of Al with Ga in Al-containing chalcogenide semiconductors has been shown to lead to a modulation of the band gap energy, thereby tuning the electrical transport properties.[15] Recently, it has been suggested that the introduction of Ga/In in an I-VI (i.e., Cu-S) system may create promising TE materials based on high-throughput calculations estimating electrical and thermal transport properties of 84,908 materials.[16] Moreover, Ga/In-based I-III-VI systems (e.g., $CuInTe_2$, $CuGaSe_2$, $CuGaS_2$) are TE materials that possess relatively low $\kappa_{car}$ and high $S$ compared with CATS.[16-19] It is known that the substitution reactions have potential to change the crystalline phases of Cu-base chalcogenides.[20,21] When the crystalline phase changed to more ordered crystal structure due to the substitution, the TE performance could be enhanced.[22] On the other hand, the presence of a complex mixture of crystalline phases in the TE material leads to suppression in $\kappa_{\text{lat}}$ resulting in the enhancement of the $ZT$ value.[23] Therefore, the dependence of the crystallite features of TE materials on their transport properties needs to be systematically investigated.

In the present study, we chemically synthesized $Cu_3Al_{1-x}Ga_xSnS_5$ ($x$ = 0, 0.25, 0.5, 0.75 and 1) nanocrystals substituting Al with Ga in CATS, and then fabricated $Cu_3Al_{1-x}Ga_xSnS_5$ nanobulk materials by pulsed electric current sintering using the nanocrystals as building blocks. Although the chemical synthesis of various kinds of Cu-based chalcogenide nanocrystals have been reported in literature so far,[20,21] $Cu_3Al_{1-x}Ga_xSnS_5$ nanocrystals have never been studied to the best of our knowledge. Subsequently, the relationships between the composition, crystalline phases and TE properties were systematically investigated for the purpose of developing earth-abundant and eco-friendly TE materials.

The work in this chapter is a part of my Ph.D. research, which has been published as a full article in the ACS Applied Energy Materials. We are grateful to Mr. Korefumi Kubota, Mr. Hiroshi Takida and Mr. Takeo Akatsuka of Nippon Shokubai Company for their support in operating Sinterland LABOX-100. We thank Ms. Naoko Fujimoto of AIST for operating the ZEM-3 and LFA457 and Mr. Atsushi Yamamoto of AIST for supporting these measurements. The author also thank Mr. Koichi Higashimine of JAIST for helping with STEM-HAADF measurements.

## 3.2 Experimental Section

### *3.2.1 Materials*

The chemicals have been used for the synthesis of $Cu_3Al_{1-x}Ga_xSnS_5$ nanoparticles are shown in Table 3.1. All chemicals were purchased from Sigma-Aldrich and used without further purification.

### *3.2.2 Synthesis of $Cu_3Al_{1-x}Ga_xSnS_5$ Nanocrystals*

The $Cu_3Al_{1-x}Ga_xSnS_5$ ($x$ = 0−1) nanocrystals were synthesized with five different compositions, referred to herein as **Powder_0**, **Powder_0.25**, **Powder_0.5**, **Powder_0.75**, and **Powder_1** corresponding to $x$ = 0, 0.25, 0.5, 0.75 and 1, respectively. The respective preparation processes were as follows: For $x$ = 0, 0.25, 0.5, 0.75, and 1, $Cu(OAc)_2$ (5 mmol), $Sn(OAc)_2$ (2 mmol), $Al(acac)_3$ (1−$x$ mmol), $Ga(acac)_3$ (2$x$ mmol, except for $x$ = 1 when $Ga(acac)_3$ was $x$ mmol), OAM (100 mL), and DDT (100 mL) were added to a three-necked flask equipped with a dry Ar inlet/outlet, trap sphere, condenser, heating mantle, thermocouple, and magnetic stirrer. Initially, the reaction mixture was stirred with Ar bubbling at room temperature for 5 min. Thereafter, the temperature was raised to 100 °C and held for 10 min with Ar bubbling to remove volatile matter. Subsequently, the reaction temperature was increased to 260 °C and held for 1 h. After cooling the reaction mixture, the nanocrystals were separated by centrifugation at 5000 rpm for 3 min. The nanocrystals were washed three times by repeating the following purification cycle: redispersion in hexane, centrifugation, and supernatant decantation. Finally, the obtained nanocrystals were dried under vacuum.

**Table 3.1** List of chemicals, their chemical formula/abbreviation and purity %.

| Chemicals | Chemical Formula / Abbrevation | Purity % |
|---|---|---|
| Copper(II) acetate hydrate | $Cu(CO_2CH_3)_2 \cdot xH_2O$ / $Cu(OAc)_2 \cdot xH_2O$ | 98.0 |
| Gallium acetylacetonate | $C_{15}H_{21}GaO_6$ / $Ga(acac)_3$ | 99.99 |
| Aluminium acetylacetonate | $C_{15}H_{21}AlO_6$ / $Al(acac)_3$ | 99.999 |
| Tin (II) acetate | $Sn(CH_3CO_2)_2$ / $Sn(OAc)_2$ | 99.0 |
| 1-Dodecanethiol | $CH_3(CH_2)_{11}SH$ / DDT | >98 |
| Oleylamine | $C_{18}H_{35}NH_2$ / OAM | 70.0 |
| Thiourea | $SC(NH_2)_2$ / TU | 99.0 |
| Hexane | $CH_3(CH_2)_4CH_3$ | 96.0 |
| Methanol | $CH_3OH$ | 99.8 |
| Toluene | $C_6H_5CH_3$ | 99.0 |

### *3.2.3 Ligand Exchange*

Because the as-synthesized nanocrystals were capped with DDT and OAM, post-synthesis ligand exchange was performed by replacing DDT/OAM with thiourea which can be more easily removed from the pellet than DDT/OAM during sintering to avoid a harmful effect on the electrical conductivity. The thiourea (TU; Tokyo Chemical Industry, 10 g) was dissolved in methanol (Kanto Chemical, 400 mL), and this TU solution was added to a dispersion of the nanocrystals (3.4 g) in toluene (250 mL). The mixture was stirred for 1 h at room temperature. After the ligand exchange reaction, the TU-capped nanocrystals were separated from the solution by centrifugation at 5000 rpm for 3 min, and were washed by redispersion in a hexane/toluene mixture, centrifugation, and supernatant decantation. The TU-capped nanocrystals were then redispersed in methanol (400 mL) whereupon toluene (125 mL) was then added. This dispersion was subjected to centrifugation at 5000 rpm for 10 min to remove excess TU.

### *3.2.4 Pelletization*

After ligand exchange, nanocrystals were pelletized into a solid disk with a diameter of 10 mm and thickness of 2–3 mm using a pulsed electric current sintering machine (Sinterland LABOX-100) under the following conditions: vacuum, 3.5 Pa; temperature, 450 °C; pelletization pressure, 30 MPa; and sintering time, 5 min. The pellets fabricated from **Powder_0**, **Powder_0.25**, **Powder_0.5**, **Powder_0.75**, and **Powder_1** are referred to as **Pellet_0**, **Pellet _0.25**, **Pellet _0.5**, **Pellet _0.75**, and **Pellet _1**, respectively. The pellets were polished using silicon carbide abrasive paper (grit size 2000) before characterization. The pellet densities were determined using a gas pycnometer (Shimadzu AccuPyc II 1340).

## 3.3 Characterization Techniques

### *3.3.1 Structural and Compositional Analyses*

The synthesized nanocrystals were characterized by a transmission electron microscope (TEM, Hitachi H-7650 operated at 100 kV), an X-ray diffractometer (XRD, Rigaku SmartLab) with Cu K$\alpha$ radiation, a scanning TEM (STEM) equipped with a high-angle annular dark-field (HAADF) detector and energy-dispersive X-ray spectroscopy (EDS) system (JEOL JEM-ARM200F operated at 200 kV), a scanning electron microscope (SEM, Hitachi TM3030) equipped with an EDS system, and an X-ray photoelectron spectroscope (XPS, Shimadzu Kratos AXIS-ULTRA DLD). The pellets were characterized by XRD and SEM-EDS.

### 3.3.2 Electrical Transport Properties Measurements

The Hall voltage $V_H$ (V) was measured at 300 K using a physical properties measurement system (PPMS; Quantum Design) by applying a magnetic field of ±5 T with an AC current. The electrodes were bonded to the rectangular in-plane specimen using gold paste. In this way, the Hall coefficient, $R_H$ ($\mathrm{cm^3\ C^{-1}}$), was calculated as $R_H = V_H d/BI$, where $d$ (m), $B$ (T) and $I$ (A) are the thickness of specimen, external magnetic field and current, respectively. Assuming single carrier transport, carrier concentration $p$ ($\mathrm{cm^{-3}}$) and Hall mobility $\mu$ ($\mathrm{cm^2\ V^{-1}\ s^{-1}}$) were calculated as $p = 1/|R_H|e$ and $\mu = R_H\sigma$, where $e$ (C) is the elementary charge.

### 3.3.3 Measurement of Thermoelectric Properties

First, $\kappa$ was measured for the pellets in the cross-plane direction by laser flash analysis (Netzsch LFA457). In this method, $\kappa$ ($\mathrm{W\ m^{-1}\ K^{-1}}$) was calculated as $\kappa = dcD$ where $d$ ($\mathrm{kg\ m^{-3}}$), $c$ ($\mathrm{J\ kg^{-1}\ K^{-1}}$), and $D$ ($\mathrm{m^2\ s^{-1}}$) are the density, specific heat, and thermal diffusivity of the pellet, respectively. Then, $S$ and electrical resistivity ($\rho$) were measured in the in-plane direction by a ZEM-3 analyzer (ULVAC-Riko). The carrier thermal conductivity, $\kappa_{car}$, was calculated as $\kappa_{car} = L\sigma T - \mathrm{PF}\cdot T$,[24] where $L$ denotes the Lorentz number ($2.44\times10^{-8}\ \mathrm{W\ \Omega\ K^{-2}}$). Finally, $\kappa_{lat}$ was calculated as $\kappa_{lat} = \kappa - \kappa_{car}$; and the $ZT$ value was calculated as $ZT = \sigma S^2 T/\kappa$.

## 3.4 Results and Discussion

### *3.4.1 Structural Characterization of Nanocrystals*

Figure 3.1 (a–e) shows the TEM images of as-synthesized $Cu_3Al_{1-x}Ga_xSnS_5$ ($x$ = 0−1) nanocrystals. It is evident that most nanocrystals have a hexagonal cylindrical shape, recognizing that some nanocrystals are standing upright and others are lying down on the TEM grid. Figure 3.1 (f–j) shows the STEM bright-field images of as-synthesized $Cu_3Al_{1-x}Ga_xSnS_5$ nanocrystals. Lattice fringes with an interplanar spacing of 3.3−3.8 Å ascribed to the {100} planes of wurtzite (WZ) phase are clearly seen in all cases. the average nanocrystal lengths and widths are shown in Figure 3.2. As can be seen, the nanocrystal size as well as the size distribution increases with increasing Ga content, $x$.

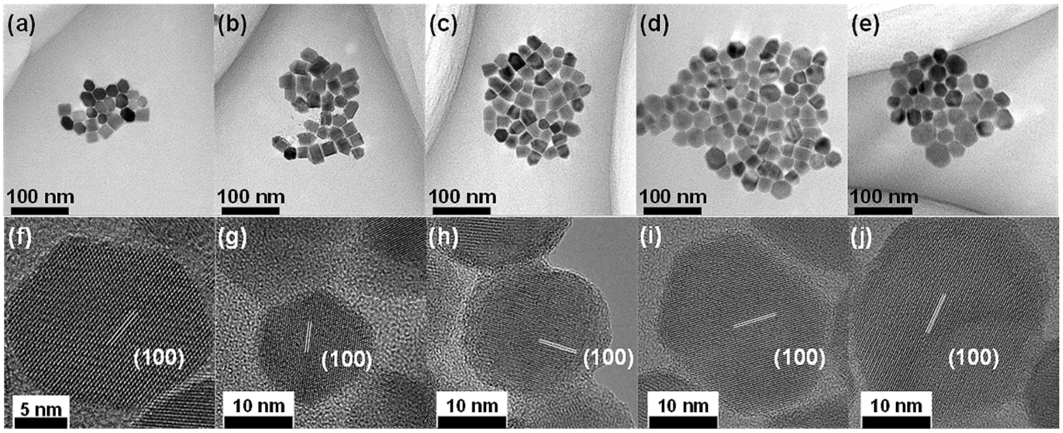

**Figure 3.1.** (a–e) TEM and (f–j) STEM bright-field images of $Cu_3Al_{1-x}Ga_xSnS_5$ nanocrystals. From left to right, $x$ = 0, 0.25, 0.5, 0.75, and 1, respectively. The lattice fringes indicated in (f–j) are ascribed to the {100} planes of WZ.

The nanocrystal size is primarily dependent on nucleation and growth rates as well as adsorption/desorption processes.[25] Using the amount of nanocrystals obtained, the nanocrystal size as estimated by TEM analysis, and the nanocrystal density as estimated by XRD analysis, the number of nuclei were calculated using the assumption that the number of nuclei approximately equals the number of nanocrystals. As a result, it was found that the number of nuclei decreased with increasing Ga content. In general, the particle size increases when the number of nuclei decreases. Therefore, the nanocrystal size increased with *x*. Applying the hard-soft acid-base theory,[26] both Ga and Al are hard acids. However, owing to the larger ionic radii of Ga compared with Al, Al is a relatively harder acid.[27] Therefore, DDT may bind more strongly with Ga than with Al through the sulfur in DDT, which is a soft base. Thus, the Ga-DDT complex would be more stable than the Al-DDT complex at a given temperature, resulting in the lower supersaturation of Ga that consequently leads to a lower nucleation rate. The nanocrystal size distribution also increased with *x* (Figure 3.2). The broadening in the size distribution would be presumably owing to Ostwald ripening.[28] Specifically, the monomer was depleted more rapidly with increased Ga content possibly because of the same reason (i.e., lower supersaturation of Ga).

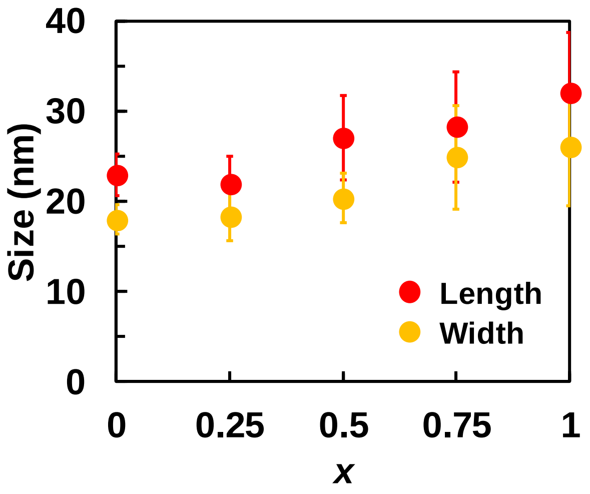

**Figure 3.2.** Average lengths and widths of $Cu_3Al_{1-x}Ga_xSnS_5$ nanocrystals with respect to *x*.

To confirm the spatial distribution of each element within a single nanocrystal, STEM-EDS elemental mapping was carried out for $Cu_3AlSnS_5$, $Cu_3Al_{0.5}Ga_{0.5}SnS_5$ and $Cu_3GaSnS_5$ (CGTS) nanocrystals, as shown in Figure 3.3. The STEM-EDS maps clearly show that both Al and Ga are evenly distributed and simultaneously exist in the particles for the case of $Cu_3Al_{0.5}Ga_{0.5}SnS_5$. The average compositions of as-synthesized nanocrystals were determined to be Cu:Al:Ga:Sn = 63:19:0:18, 61:15:5:19, 64:7:8:21, 59:6:16:19, and 62:0:19:19 for **Powder_0**, **Powder_0.25**, **Powder_0.5**, **Powder_0.75**, and **Powder_1**, respectively, using SEM-EDS. Those atomic ratios are approximately equal to the nominal compositions of $Cu_3Al_{1-x}Ga_xSnS_5$ with $x = 0, 0.25, 0.5, 0.75$ and 1, respectively.

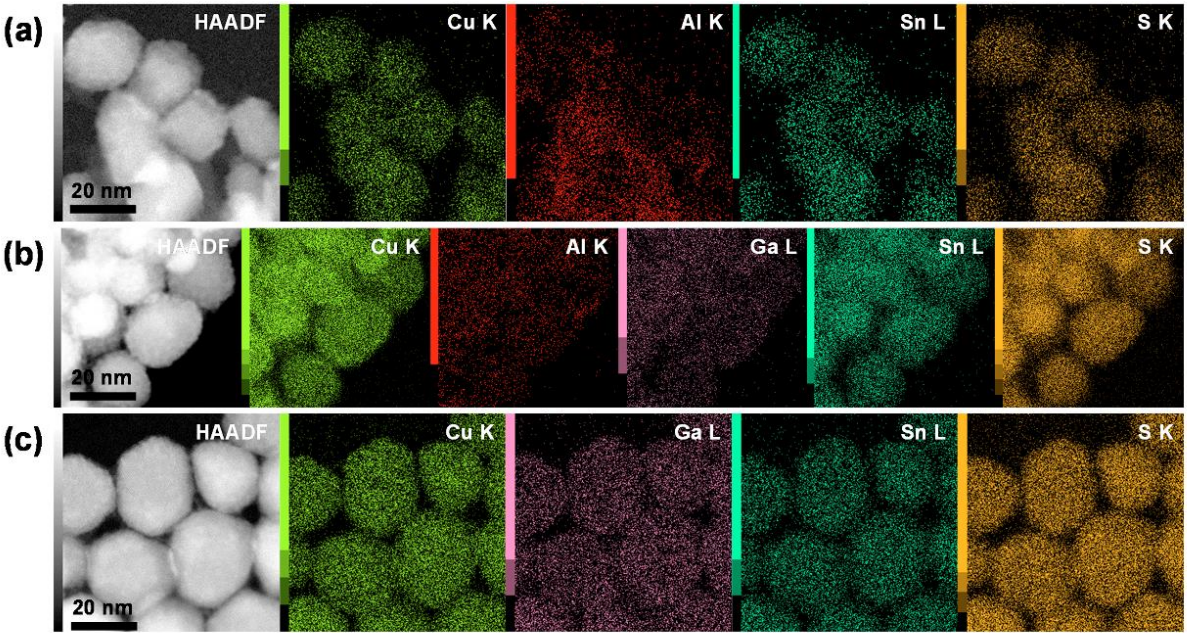

**Figure 3.3.** HAADF-STEM images and corresponding EDS elemental mapping images for Cu, Al, Ga, Sn, and S of the (a) $Cu_3AlSnS_5$ (CATS), (b) $Cu_3Al_{0.5}Ga_{0.5}SnS_5$ and (c) $Cu_3GaSnS_5$ (CGTS) nanocrystals.

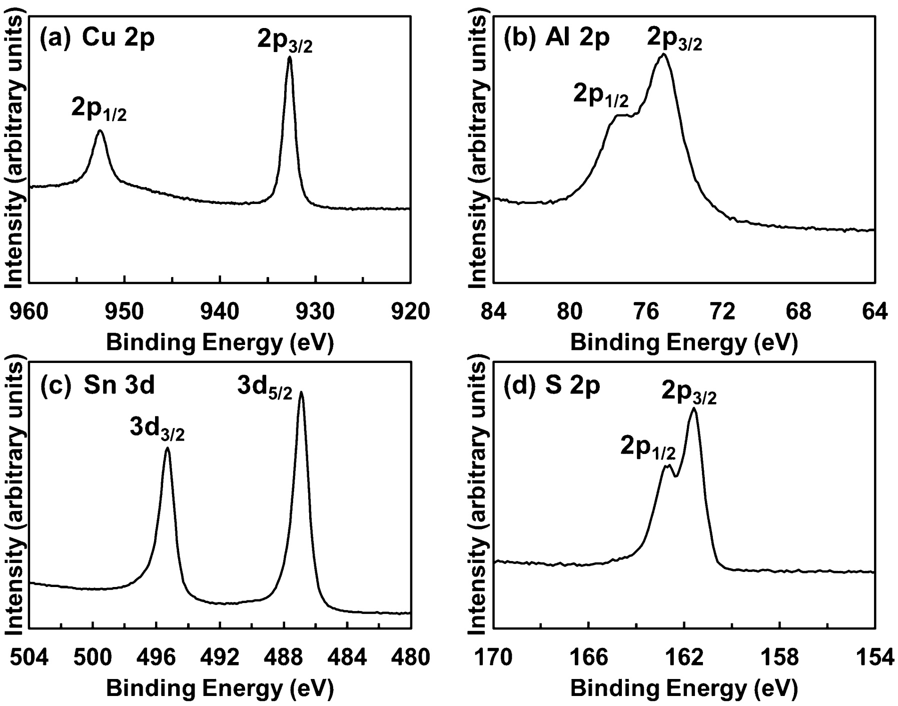

**Figure 3.4** XPS spectra for (a) Cu 2p, (b) Al 2p, (c) Sn 3d, and (d) S 2p of the CATS nanocrystals.

To determine the oxidation states of elements in the nanocrystals, core-level XPS analysis for **Powder_0** and **Powder_1** was performed. Figure 3.4 shows the Cu 2p, Al 2p, Sn 3d and S 2p spectra obtained for **Powder_0**. The binding energies of Cu $2p_{3/2}$ and Cu $2p_{1/2}$ were 932.2 and 952.1 eV, respectively, where this peak separation of 19.9 eV is indicative of the presence of $Cu^{+}$.[11] The Al $2p_{3/2}$ peak appeared at a binding energy of 74.6 eV and can be assigned to $Al^{3+}$.[11] The presence of $Sn^{4+}$ was confirmed by the peaks observed at 486.4 eV ($3d_{5/2}$) and 494.8 eV ($3d_{3/2}$) with a characteristic peak separation of 8.4 eV.[11] Furthermore, the presence of $S^{2-}$ was confirmed by the peaks located at 161.5 eV ($2p_{3/2}$) and 162.6 eV ($2p_{1/2}$) with a peak splitting of 1.1 eV, which is consistent with the literature value for metal sulfides.[11]

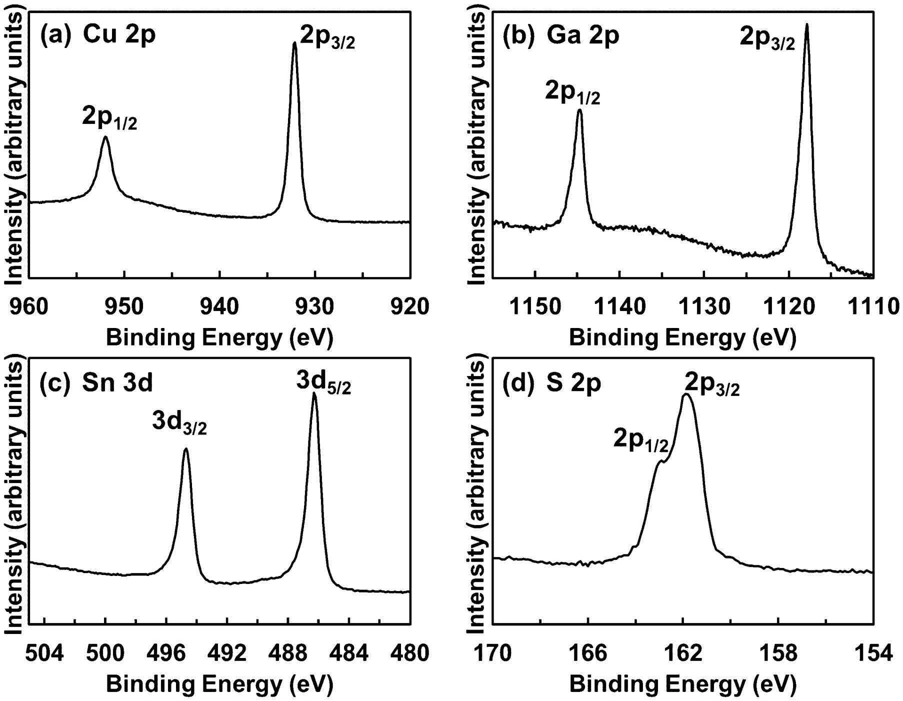

**Figure 3.5** XPS spectra of (a) Cu 2p, (b) Ga 2p, (c) Sn 3d, and (d) S 2p of the CGTS nanocrystals.

Figure 3.5 shows the Cu 2p, Ga 2p, Sn 3d and S 2p spectra obtained for **Powder_1**. The binding energies of Cu, Sn and S exhibited the similar oxidation states to the case of **Powder_0**. The Ga $2p_{3/2}$ and Ga $2p_{1/2}$ peaks respectively appeared at binding energies of 1117.9 and 1144.8 eV, which can be assigned to $Ga^{3+}$.[29]

Figure 3.6 (a–e) shows XRD patterns of **Powder_0**, **Powder_0.25**, **Powder_0.5**, **Powder_0.75**, and **Powder_1**. Rietveld refinement of the XRD patterns was performed with the FullPROF program[30] using WZ and zinc blende (ZB) ZnS crystallographic information files.[31] Simulated XRD patterns for which Cu, Sn, Al, and Ga ions randomly occupy Zn sites in the ZnS structure (see Figure 3.7) are shown as black lines in Figure 3.6, and occupancy parameters are as listed in Table 3.2. The Rietveld refinement revealed that the primary crystal structure of all nanocrystals was WZ with small amounts of ZB (Table 3.3).

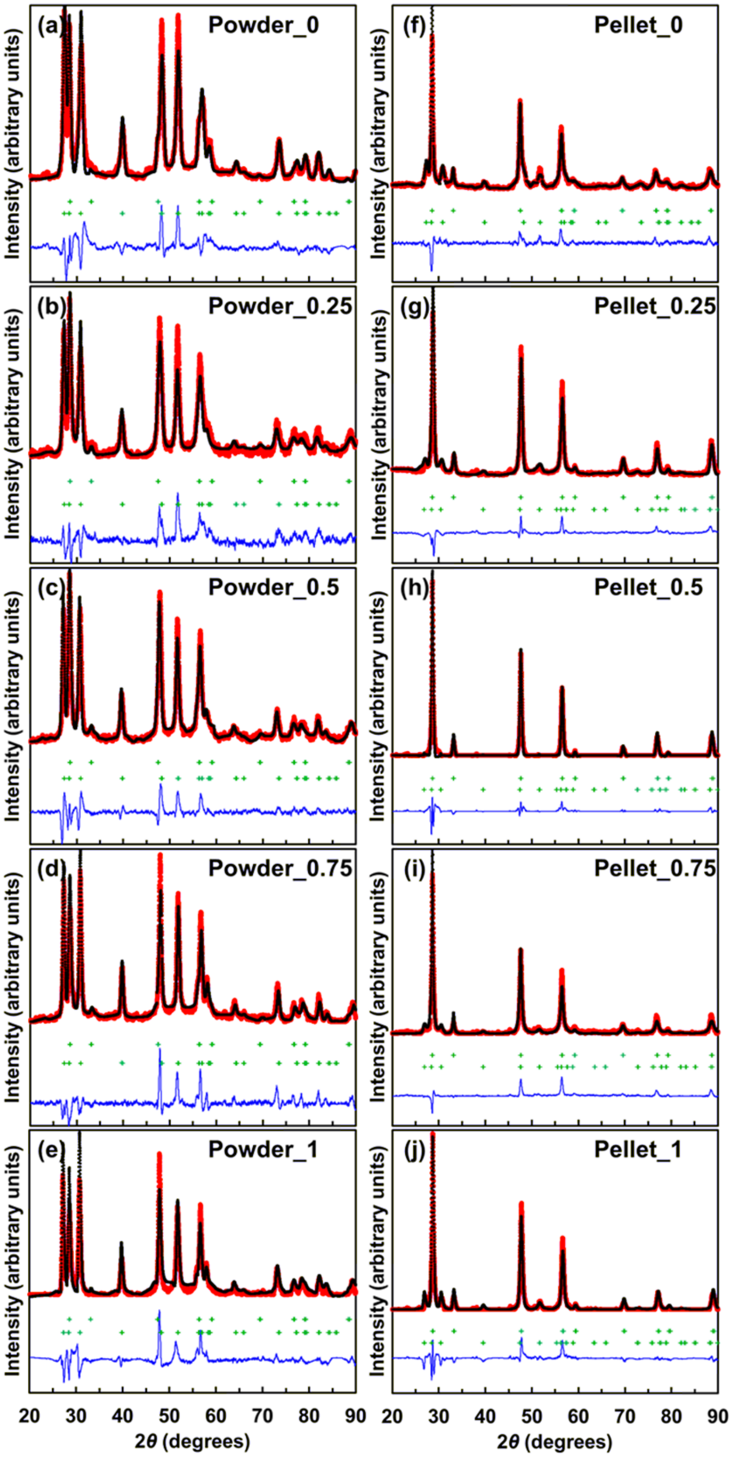

**Figure 3.6.** XRD patterns of (a) **Powder_0**, (b) **Powder_0.25**, (c) **Powder_0.5**, (d) **Powder_0.75**, and (e) **Pellet_1** (f) **Pellet_0**, (g) **Pellet_0.25**, (h) **Pellet_0.5**, (i) **Pellet_0.75**, and (j) **Pellet_1**. Shown are the experimental patterns (red lines) and the Rietveld refined patterns (black lines) and their difference (blue lines), as well as the Bragg reflection positions (short green bars below the diffraction patterns).

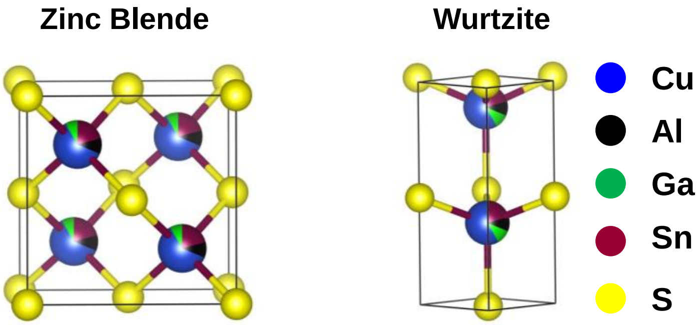

**Figure 3.7.** Crystal structures for the powder and pellet samples comprising a mixture of zinc blende (ZB) and wurtzite (WZ) structures are generated using Table 3.1, showing copper (blue circle), sulfur (yellow circle), aluminum (black circle), gallium (green circle), and tin (brown circle).

**Table 3.2.** Occupancy parameter of each atom in $Cu_3Al_{1-x}Ga_xSnS_5$ nanocrystals used for crystal structure generation.

| Sample | Occupancy Parameter | | | | |
|---|---|---|---|---|---|
| | Cu | Al | Ga | Sn | S |
| **Powder_0** | 0.6 | 0.2 | 0.0 | 0.2 | 1.0 |
| **Powder_0.25** | 0.6 | 0.15 | 0.05 | 0.2 | 1.0 |
| **Powder_0.5** | 0.6 | 0.1 | 0.1 | 0.2 | 1.0 |
| **Powder_0.75** | 0.6 | 0.05 | 0.15 | 0.2 | 1.0 |
| **Powder_1** | 0.6 | 0.0 | 0.2 | 0.2 | 1.0 |

**Table 3.3.** Wurtzite (WZ) and zinc blende (ZB) contents of $Cu_3Al_{1-x}Ga_xSnS_5$ nanocrystals.

| Sample | WZ (wt%) | ZB (wt%) |
|---|---|---|
| **Powder_0** | 98 | 2 |
| **Powder_0.25** | 82 | 18 |
| **Powder_0.5** | 81 | 19 |
| **Powder_0.75** | 87 | 13 |
| **Powder_1** | 84 | 16 |

The mean crystalline size ($D_{\mathrm{xrd}}$) was calculated with the Scherrer formula using the primary peak of the WZ phase. The values of $D_{\mathrm{xrd}}$ were calculated as 9.1, 10.2, 13.8, 17.6, and 16.1 nm for **Powder_0**, **Powder_0.25**, **Powder_0.5**, **Powder_0.75**, and **Powder_1**, respectively. Figure 3.8 shows the $D_{\mathrm{xrd}}$ values plotted versus the average widths of nanocrystals as measured by TEM ($D_{\mathrm{TEM}}$). As can be seen in Figure 3.8, $D_{\mathrm{xrd}}$ is always slightly smaller than $D_{\mathrm{TEM}}$, indicating that nanocrystals are polycrystalline in nature and/or have low crystallinity.[32]

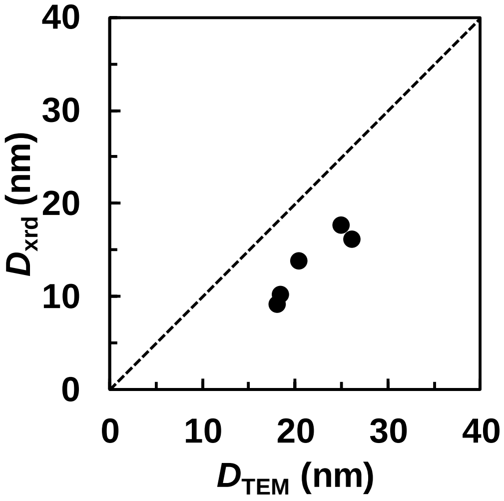

**Figure 3.8.** Mean crystalline size obtained via X-ray diffraction $D_{\mathrm{xrd}}$ plotted vs the average widths of nanocrystals obtained via transmission electron microscopy $D_{\mathrm{TEM}}$ for $Cu_3Al_{1-x}Ga_xSnS_5$ nanocrystals.

### *3.4.2 Compositional Analysis*

To know the composition of samples SEM-EDS have been used. The atomic percentage of Cu:Al:Ga:Sn have been summarized in Table 3.4. The average pellet composition was determined to be Cu:Al:Ga:Sn = 61:22:0:17, 61:15:6:18, 63:8:8:21, 59:6:16:19, and 61:0:19:20 for **Pellet_0**, **Pellet_0.25**, **Pellet_0.5**, **Pellet_0.75**, and **Pellet_1**, respectively, using SEM-EDS. Those atomic ratios are approximately equal to the nominal compositions of $Cu_3Al_{1-x}Ga_xSnS_5$ with $x = 0$, 0.25, 0.5, 0.75 and 1, respectively. The results exemplify that there is no significant change in the composition after pelletization as well.

**Table 3.4.** Atomic compositions for **Powder_0**, **Powder_0.25**, **Powder_0.5**, **Powder_0.75**, **Powder_1** and **Pellet_0**, **Pellet_0.25**, **Pellet_0.5**, **Pellet_0.75** and **Pellet_1** determined using SEM-EDS.

| **Sample** | **SEM-EDS** | | | |
|---|---|---|---|---|
| | **Cu (at %)** | **Al (at %)** | **Ga (at %)** | **Sn (at %)** |
| Powder_0 | 63 | 19 | 0 | 18 |
| Pellet_0 | 61 | 22 | 0 | 17 |
| Powder_0.25 | 61 | 15 | 5 | 19 |
| Pellet_0.25 | 61 | 15 | 6 | 18 |
| Powder_0.5 | 64 | 7 | 8 | 21 |
| Pellet_0.5 | 63 | 8 | 8 | 21 |
| Powder_0.75 | 59 | 6 | 16 | 19 |
| Pellet_0.75 | 59 | 6 | 16 | 19 |
| Powder_1 | 62 | 0 | 19 | 19 |
| Pellet_1 | 61 | 0 | 19 | 20 |

### *3.4.3 Structural Characterization of Pellets*

Figure 3.6 (f–j) shows XRD patterns of **Pellet_0**, **Pellet_0.25**, **Pellet_0.5**, **Pellet_0.75**, and **Pellet_1**. The densities of **Pellet_0**, **Pellet_0.25**, **Pellet_0.5**, **Pellet_0.75**, and **Pellet_1** were measured to be 4.356, 4.383, 4.406, 4.354, and 4.405 g·cm$^{-3}$, respectively. The relative densities of all of the pellets were greater than 90% when compared with the theoretical densities. To perform quantitative phase-composition analysis of the pellets, Rietveld refinement of the XRD patterns was performed. A phase transition from WZ to ZB was clearly observed for all samples during sintering, and the weight percentages of ZB and WZ phases for all pellets are shown in Table 3.5. Note that no impurity phases such as CuS and SnS were detected. This phase transition was ascribed to the higher thermodynamic stability of the ZB phase than that of the WZ phase, which is owing to the former having a more highly ordered structure. It is noteworthy that **Pellet_0.5** exhibited a certain trend in the phase fraction obtained from XRD analysis, wherein **Pellet_0.5** exhibits more than 95 wt% of ZB phase, which is the highest among all of the pellets. The larger ionic radius of Ga than that of Al can create lattice distortion, affecting the crystal strain and thereby the phase fraction content with the extent of Ga incorporation in the CATS system.[27,33,34] The lattice strain ($\varepsilon$) was estimated using the Williamson-Hall method,[35] as shown in Figure 3.9. It was found that **Pellet_0.5** exhibited a minimum strain, almost 55% less than **Pellet_0** (pristine CATS) and 45% less than **Pellet_1** (CGTS), and therefore the content of Ga and Al in **Pellet_0.5** may contribute to a more ordered crystal structure.

**Table 3.5.** Wurtzite (WZ) and zinc blende (ZB) contents of $Cu_3Al_{1-x}Ga_xSnS_5$ nanobulk materials.

| Sample | WZ (wt%) | ZB (wt%) |
|---|---|---|
| **Pellet_0** | 35 | 65 |
| **Pellet_0.25** | 22 | 78 |
| **Pellet_0.5** | 2 | 98 |
| **Pellet_0.75** | 25 | 75 |
| **Pellet_1** | 27 | 73 |

The lattice constants of the ZB phase are plotted as a function of *x* in Figure 3.10, where the lattice constant is seen to increase linearly with *x*, confirming successful substitution of Al with Ga. The $D_{\mathrm{xrd}}$ values of **Pellet_0**, **Pellet_0.25**, **Pellet_0.5**, **Pellet_0.75**, and **Pellet_1** were respectively calculated to be 21.3, 19.8, 23.1, 21.7, 23.5 nm by the Williamson-Hall method. These values indicate that the mean crystalline size slightly increased during sintering for all pellets, possibly owing to grain boundary fusion.[36]

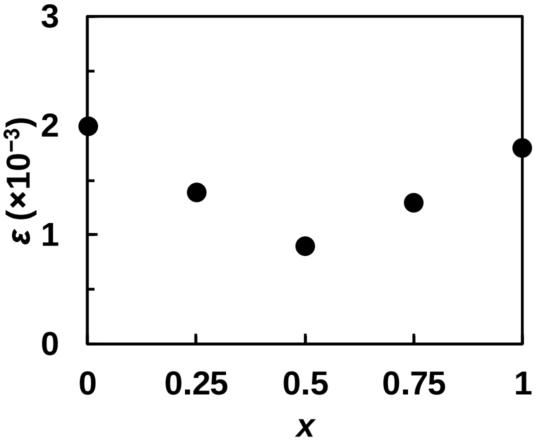

**Figure 3.9.** Lattice strain $\varepsilon$ plotted as a function of *x*.

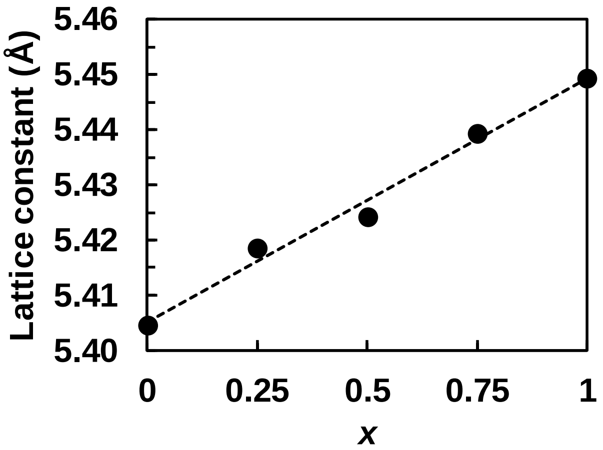

**Figure 3.10.** Lattice constant for the zinc blende (ZB) phase of pellets plotted as a function of *x*.

### *3.4.4 Thermoelectric Properties*

Figure 3.11 shows the TE properties of **Pellet_0**, **Pellet_0.25**, **Pellet_0.5**, **Pellet_0.75**, and **Pellet_1**. The thermal diffusivity and specific heat of all pellet samples are provided in Figure 3.12. As shown in Figure 3.11 (a), the $\sigma$ for **Pellet_0** decreases with temperature, indicating its metallic behavior.[11] However, Ga-containing pellets (**Pellet_0.25**, **Pellet_0.5**, **Pellet_0.75**, and **Pellet_1**) showed the increase in $\sigma$ with temperature, which indicates their semiconductor behavior. It is noteworthy that the $\sigma$ values of **Pellet_0** were one or two orders of magnitude higher than those of the other pellets, as well as other high-performance copper-sulfide-based TE materials including $Cu_{1.97}S$,[37] $Cu_{10}Ni_2Sb_4S_{13}$,[38] and $Cu_{26}V_2Sn_6S_{32}$.[39] Figure 3.11 (b) illustrates the temperature dependence of $S$. In general, $S$ depends inversely on $\sigma$, and therefore a decrease in $\sigma$ with increasing Ga content enhances $S$. In other words, the increased $S$ values of **Pellet_0.25**, **Pellet_0.5**, **Pellet_0.75** and **Pellet_1** over that of **Pellet_0** (CATS) may be owing to the larger value of $p$ exhibited by **Pellet_0**.

Figure 3.11 (c) displays the temperature dependence of $\kappa$, where the $\kappa$ values are less than 0.42 $W \cdot m^{-1} \cdot K^{-1}$ for all pellets except **Pellet_0**. Figure 3.11 (d) shows $\kappa_{lat}$ plotted as a function of temperature, where no apparent temperature dependence can be observed. This lack of temperature dependence is more evident in the inset of Figure 3.11 (d), where the characteristic $1/T$ dependence of $\kappa_{lat}$ indicates that the phonon scattering is dominated by defect scattering, which includes nanograins and lattice distortion.[5] As mentioned earlier, the high $\kappa$ value of **Pellet_0** is owing to a high $\kappa_{car}$ value. The efficient reduction of $\kappa_{car}$ by the replacement of Al with Ga in CATS is evident, as shown in Figure 3.13. Note that $S$ and $\sigma$ were measured during both the heating and cooling cycle and the values were found to coincide in both cycle types, as shown in Figure 3.14.

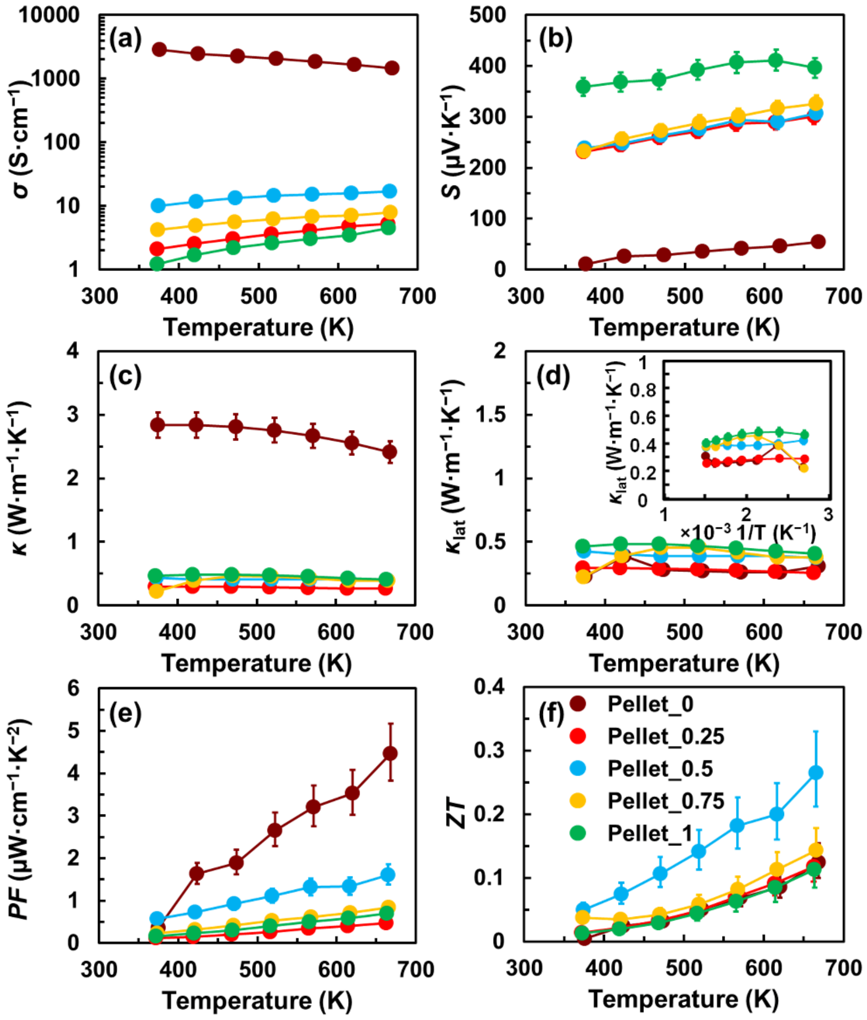

**Figure 3.11.** (a) Electrical conductivity $\sigma$, (b) Seebeck coefficient $S$, (c) total thermal conductivity $\kappa$, (d) lattice thermal conductivity $\kappa_{\mathrm{lat}}$, (e) power function PF, and (f) dimensionless figure of merit $ZT$ values of **Pellet_0** (brown circles), **Pellet_0.25** (red circles), **Pellet_0.5** (blue circles), **Pellet_0.75** (yellow circles), **Pellet_1** (green circles). The inset of (d) shows $\kappa_{\mathrm{lat}}$ plotted with respect to the reciprocal of temperature.

Figure 3.11 (e) and (f) show the temperature dependence of PF and $ZT$, respectively. Because of its high $\sigma$, **Pellet_0** exhibited the highest PF among all pellets, though its $ZT$ value was only 0.12 (at 668 K) owing to its high $\kappa$. Despite **Pellet_1** possessing the highest $S$ value along with a substantially suppressed $\kappa$, its low $\sigma$ contributed to suppression of the PF. Therefore, **Pellet_1** deviated from the conditions for acquiring a high $ZT$ value (0.11 at 664 K), but was instead almost the same as in the case of **Pellet_0**. However, **Pellet_0.5** exhibited a *ZT* value of 0.26 (at 665 K), which is more than twofold that of the CATS (**Pellet_0**) and CGTS (**Pellet_1**) nanobulks.

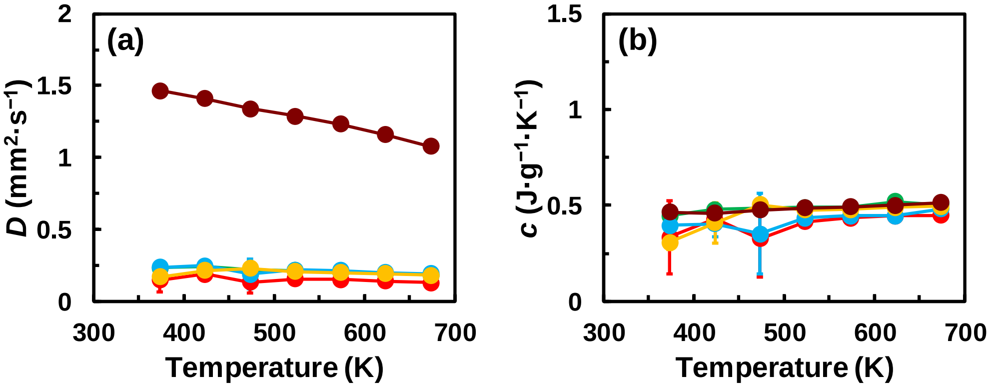

**Figure 3.12.** (a) Thermal diffusivity $D$ (mm$^2$·s$^{-1}$) and (b) specific heat $c$ (J·g$^{-1}$·K$^{-1}$) of **Pellet_0** (brown circles), **Pellet_0.25** (red circles), **Pellet_0.5** (blue circles), **Pellet_0.75** (yellow circles), and **Pellet_1** (green circles).

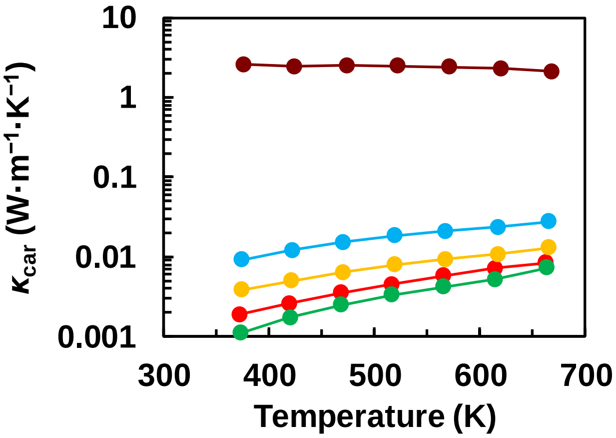

**Figure 3.13.** Carrier thermal conductivity $\kappa_{\mathrm{car}}$ of **Pellet_0** (brown circles), **Pellet_0.25** (red circles), **Pellet_0.5** (blue circles), **Pellet_0.75** (yellow circles), and **Pellet_1** (green circles).

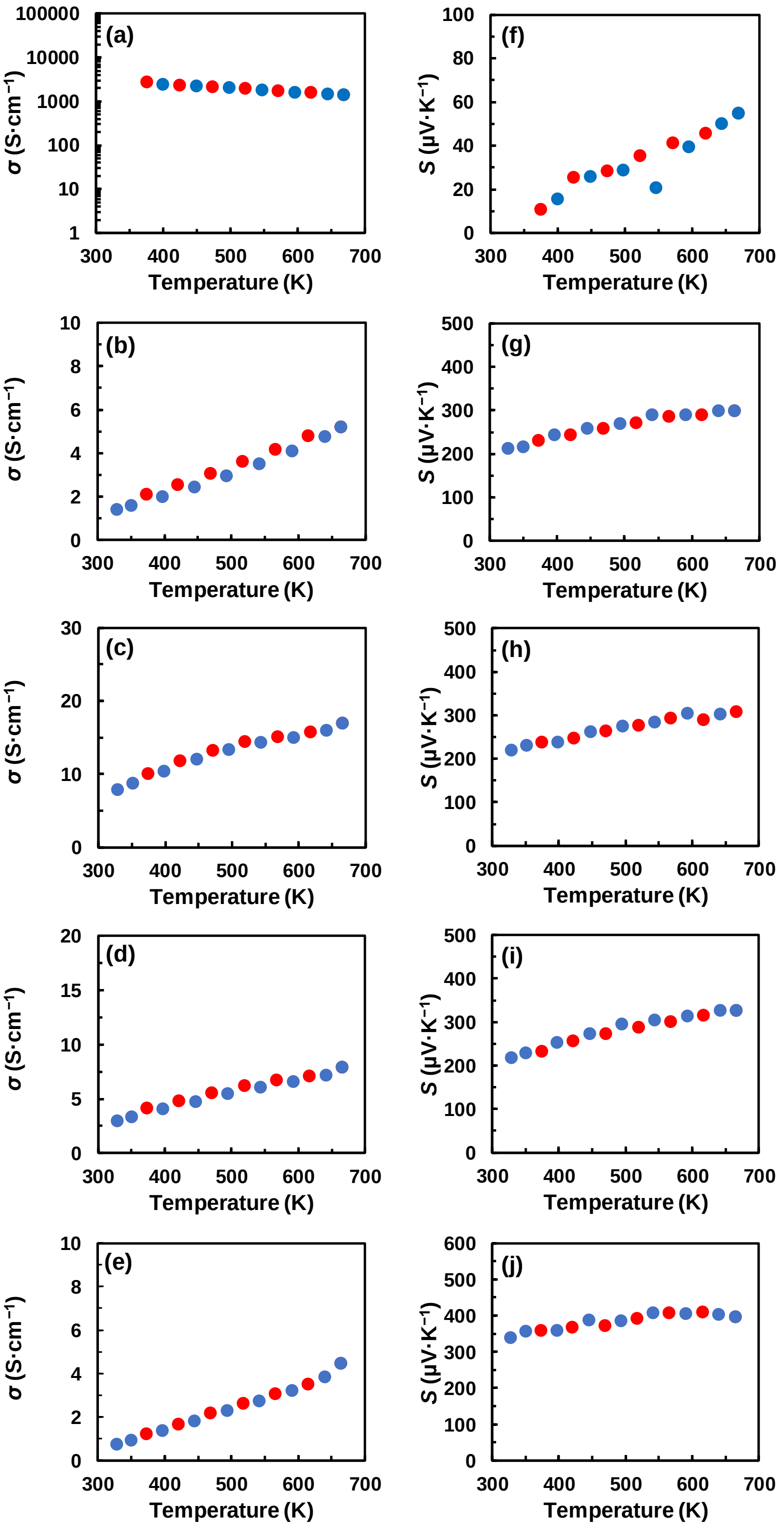

**Figure 3.14.** (a–e) Electrical conductivity *σ* and (f–j) Seebeck coefficient *S* of **Pellet_0**, **Pellet_0.25**, **Pellet_0.5**, **Pellet_0.75**, and **Pellet_1**, respectively, for the heating (red circles) and cooling (blue circles) cycles.

To understand the reason for the variation of $\sigma$ with respect to $x$, the activation energy $E_a$ was estimated using the Arrhenius equation[40]

$$\sigma = \sigma_0 \exp\left(-\frac{E_a}{k_B T}\right), \tag{3.1}$$

where $k_B$ is the Boltzmann constant, and $T$ is the absolute temperature. Figure 3.15 (a) reveals that the Ga-containing pellets (i.e., **Pellet_0.25, Pellet_0.5, Pellet_0.75**, and **Pellet_1**) exhibit a linear correlation between ln $\sigma$ and $1/T$. The values of $E_a$ were then plotted as a function of $x$, as shown in Figure 3.15 (b), exhibiting a parabolic correlation between $E_a$ and $x$. A parabolic minimum was observed for **Pellet_0.5**, indicating that it has the smallest activation energy among the samples. We also measured $p$ and $\mu$ at 300 K, as shown in Table 3.6. The substitution of Al with Ga in the CATS led to substantial reduction in $p$ by more than one or two orders of magnitude. The decrease in $p$ is likely owing to the variation in $E_a$. **Pellet_0** was not included in the analyses primarily because its electronic nature was totally different (i.e., metallic) from the other pellets (i.e., semiconductor).

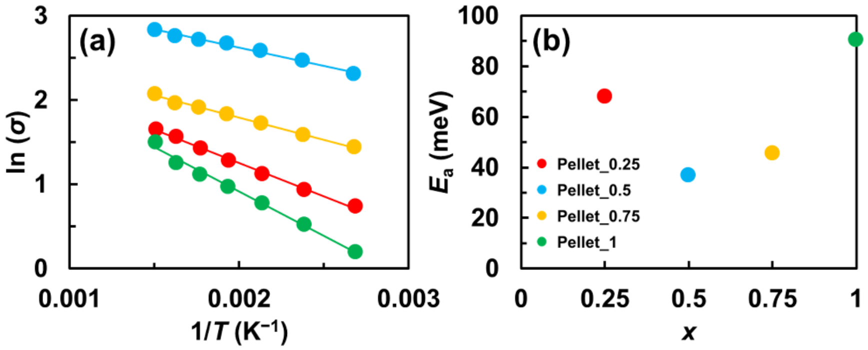

**Figure 3.15.** (a) Natural logarithmic plot of electrical conductivity ln $\sigma$ with respect to the reciprocal of temperature and (b) activation energy $E_a$ plotted with respect to $x$ for **Pellet_0.25** (red circles), **Pellet_0.5** (blue circles), **Pellet_0.75** (yellow circles), and **Pellet_1** (green circles).

**Table 3.6.** Parameters at ~300 K of $Cu_3Al_{1-x}Ga_xSnS_5$ nanobulk materials.

| **Sample** | $E_a$ **(meV)** | $p$ **(cm$^{-3}$)** | $\mu$ **(cm$^2$·V$^{-1}$·s$^{-1}$)** | $R_H$ **(cm$^3$·C$^{-1}$)** | $m^*/m_0$ **(−)** | $\tau$ **(s)** |
|---|---|---|---|---|---|---|
| **Pellet_0.25** | 67.9 | $1.9\times10^{20}$ | 0.2 | $3.2\times10^{-2}$ | 3 | $0.3\times10^{-15}$ |
| **Pellet_0.5** | 36.9 | $4.7\times10^{20}$ | 1.0 | $1.3\times10^{-2}$ | 7 | $4.0\times10^{-15}$ |
| **Pellet_0.75** | 45.5 | $2.3\times10^{20}$ | 0.2 | $2.8\times10^{-2}$ | 5 | $0.6\times10^{-15}$ |
| **Pellet_1** | 90.5 | $6.9\times10^{19}$ | 0.4 | $9.2\times10^{-2}$ | 3 | $0.7\times10^{-15}$ |

Note: **Pellet_0** is omitted owing to the metallic character ($p$~$10^{21}$ cm$^{-3}$).[11]

Both $S$ and $\mu$ are dependent on the effective mass, $m^*$.[41] To estimate $m^*$, we assumed that acoustic phonon scattering and neutral impurity scattering are dominant in the high-temperature region. Thus, $\sigma$ and $S$ can be written as[24,42]

$$\sigma = \frac{4e^2 N_{\mathrm{B}} \tau_0}{3\sqrt{\pi} m^*}(s+\tfrac{3}{2}) F_{s+\frac{1}{2}}(\xi_{\mathrm{F}}), \tag{3.2}$$

$$S = \frac{k_{\mathrm{B}}}{e}\left\{\frac{\left(s+\frac{5}{2}\right)F_{s+\frac{3}{2}}(\xi_{\mathrm{F}})}{\left(s+\frac{3}{2}\right)F_{s+\frac{1}{2}}(\xi_{\mathrm{F}})} - \xi_{\mathrm{F}}\right\}, \tag{3.3}$$

$$S_{\mathrm{neu+ap}} = \frac{\sigma_{\mathrm{neu}} S_{\mathrm{neu}} + \sigma_{\mathrm{ap}} S_{\mathrm{ap}}}{\sigma_{\mathrm{neu}} + \sigma_{\mathrm{ap}}} \tag{3.4}$$

where $F_s(\xi_F)$ is the Fermi integral; $N_B$ is the effective density of states; $\tau_0$ is the proportionality constant; $s$ is the scattering parameter with values −1/2 and 0 for the cases of acoustic phonon scattering and neutral scattering, respectively; $S_{neu+ap}$ is the overall Seebeck coefficient including both contributions from neutral and acoustic phonon scattering according to Matthiessen's rule; $\sigma_{neu}$ and $S_{neu}$ are the electrical conductivity and Seebeck coefficient in the case of neutral impurity scattering; $\sigma_{ap}$ and $S_{ap}$ are the electrical conductivity and Seebeck coefficient in the case of acoustic phonon scattering. From these equations we estimated the values of $m^*$ using experimentally-obtained $S$ and $p$ values, as shown in Figure 3.16.

As can be seen in Figure 3.16, **Pellet_0.5** has the highest $m^*$ (~$7m_0$, where $m_0$ is the mass of the free electron). However, the increase in $m^*$ is associated with a decrease in $\mu$, whereby the relation between $\mu$ and $m^*$ can be expressed as[24]

$$\mu = \frac{e\tau}{m^*} \tag{3.5}$$

where $\tau$ denotes the charge carrier relaxation time. **Pellet_0.5** has the highest $\mu$ despite it exhibiting the highest $m^*$, suggesting that **Pellet_0.5** possesses a longer $\tau$ (Table 3.6).[24]

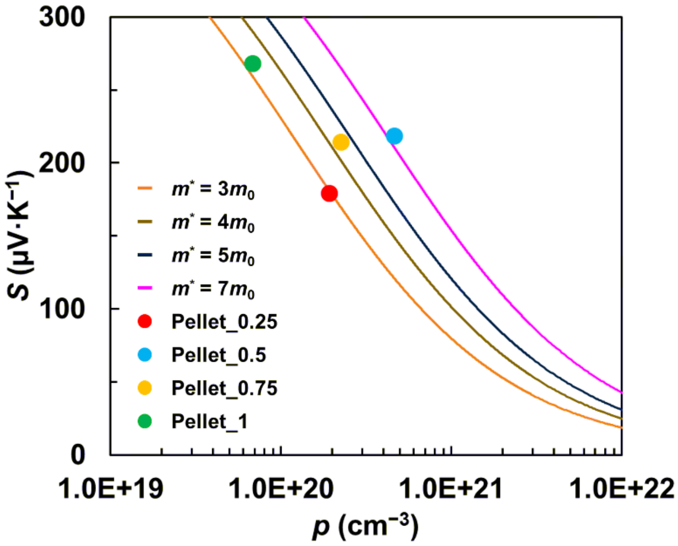

**Figure 3.16.** Seebeck coefficient $S$ estimated by considering acoustic phonon scattering and neutral scattering plotted as a function of carrier concentration $p$ for various values of effective mass $m^*$, where $m_0$ is the mass of the free electron.

Narrowing down the parameters dominant in reducing $\kappa_{car}$ (i.e. $\sigma$) or enhancing $S$ is important to understand the underlying mechanisms. To understand the dominant factor in the system under analysis, a correlation matrix was generated, as shown in Table 3.7. In Table 3.7, it can be clearly observed that the ZB phase content exhibits a distinct positive correlation with the $ZT$ value. As stated, to better understand the dependence of $S$ and $\sigma$ (and $\kappa_{car}$) on number of other parameters such as $\mu$, $E_a$, $p$, as well as indirectly on $\varepsilon$, requires untangling the individual contributions. Table 3.7 reveals the values of $p$, $\mu$ and ZB phase content to be significant parameters, manifesting at least five strong correlations among the parameters under consideration. It can be easily observed that the ZB phase content exhibits the highest number and magnitude of correlations with the other considered parameters and emerges as one of the most important inherent material characteristics.

**Table 3.7.** Correlation matrix for parameters at ~300 K of $Cu_3Al_{1-x}Ga_xSnS_5$ nanobulk materials. The correlation cells expressing dominance ($|r| \geq 0.5$ where $r$ is the correlation coefficient) have been highlighted with color (positive and negative correlations are shown in pink and blue, respectively).

| | **ZB** | $\boldsymbol{S}$ | $\boldsymbol{\kappa_{lat}}$ | $\boldsymbol{p}$ | $\boldsymbol{\mu}$ | $\boldsymbol{E_a}$ | $\boldsymbol{\varepsilon}$ | $\boldsymbol{ZT}$ |
|---|---|---|---|---|---|---|---|---|
| **ZB** | 1 | | | | | | | |
| $\boldsymbol{S}$ | −0.205 | 1 | | | | | | |
| $\boldsymbol{\kappa_{lat}}$ | 0.724 | 0.456 | 1 | | | | | |
| $\boldsymbol{p}$ | 0.945 | −0.355 | 0.494 | 1 | | | | |
| $\boldsymbol{\mu}$ | 0.917 | 0.198 | 0.924 | 0.786 | 1 | | | |
| $\boldsymbol{E_a}$ | −0.690 | 0.482 | −0.088 | −0.888 | −0.460 | 1 | | |
| $\boldsymbol{\varepsilon}$ | −0.869 | 0.511 | −0.307 | −0.979 | −0.643 | 0.946 | 1 | |
| $\boldsymbol{ZT}$ | 0.934 | −0.300 | 0.503 | 0.997 | 0.794 | −0.898 | −0.971 | 1 |

ZB (wt%): zinc blende content, $S$ ($\mu V \cdot K^{-1}$): Seebeck coefficient, $\kappa_{lat}$ ($W \cdot m^{-1} \cdot K^{-1}$): lattice thermal conductivity, $p$ ($cm^{-3}$): carrier concentration, $\mu$ ($cm^2 \cdot V^{-1} \cdot K^{-1}$): Hall mobility, $E_a$ (meV): activation energy, $\varepsilon$: lattice strain, $ZT$: dimensionless figure of merit.

To be precise, the ZB phase content exhibits a total of six correlations (four positive ($\kappa_{lat}$, $p$, $\mu$, $ZT$) and two negative ($E_a$, $\varepsilon$)). We note that **Pellet_0.5** has the lowest $E_a$, which would lead to the highest $p$, that contributes to the increase in $\sigma$ within the Ga-containing samples. The highest $p$ and the highest $\mu$ values exhibited by **Pellet_0.5** can be associated with the higher degree of band degeneracy in the sample, resulting from its more ordered crystal phase structure.[34, 43] On the contrary, for the **Pellet_0.25**, **Pellet_0.75** and **Pellet_1** the presence of greater crystal strain leads to higher $E_a$ and thus lower $p$, $\mu$ and thereby lower the $ZT$ value. Considering all of these correlations together, the enhancement in the $ZT$ value for **Pellet_0.5** can be understood as a decrease in $p$ from the CATS nanobulk value that leads to a significant reduction in $\kappa_{car}$ owing to the Ga substitution;  and the highest ZB phase fraction contributes to the highest PF among the $Cu_3Al_{1-x}Ga_xSnS_5$ ($0.25 \leq x \leq 1$) nanobulk materials. Though the $ZT$ value of the material is derived from a combination of each parameter contribution, the $p$ and ZB phase content of the given system plays a major role in influencing the other parameters.

## 3.5. Conclusions

A series of Cu-Al/Ga-Sn-S-based materials were synthesized and used for TE performance evaluation. The effect of Ga substitution in the $Cu_3Al_{1-x}Ga_xSnS_5$ nanobulk materials on their transport properties was systematically investigated. The $Cu_3Al_{1-x}Ga_xSnS_5$ nanobulk for $x = 0.5$ exhibited a $ZT$ value more than twice that for $x = 0$ at 665 K. An exhaustive examination of the correlations existing among transport parameters, crystal structure and thermoelectric performance of the $Cu_3Al_{1-x}Ga_xSnS_5$ ($0.25 \leq x \leq 1$) nanobulks showed that the ZB fraction was an important parameter that was strongly related to the electrical as well as thermal characteristics of the material. Overall, **Pellet_0.5** exhibited the highest $ZT$ value among the Ga-containing samples ranging from $0 \leq x \leq 1$ owing to its significantly reduced $\kappa_{car}$ along with its highest ZB phase fraction, resulting in a greater PF contribution. Despite the ZB phase content not appearing in the $ZT$ value determination, the dominance of this material-inherent characteristic property makes this study very interesting. This study exemplifies a systematic methodology for CATS-based nanobulk TE materials to simultaneously control the $\kappa_{\mathrm{car}}$ as well as the $\kappa_{\mathrm{lat}}$, and represents an excellent methodology to tune the thermoelectric material performance.

# References

(1) Vineis, C. J.; Shakouri, A.; Majumdar, A.; Kanatzidis, M. G. Nanostructured Thermoelectrics: Big Efficiency Gains from Small Features. *Adv*. *Mater*. **2010**, *22*, 3970-3980.

(2) Lan, Y.; Minnich, A. J.; Chen, G.; Ren, Z. Enhancement of Thermoelectric Figure-of-Merit by a Bulk Nanostructuring Approach. *Adv*. *Funct*. *Mater*. **2010**, *20*, 357-376.

(3) Poudel, B.; Hao, Q.; Ma, Y.; Lan, Y.; Minnich, A.; Yu, B.; Yan, X.; Wang, D.; Muto, A.; Vashaee, D.; Chen, X.; Liu, J.; Dresselhaus, M. S.; Chen, G.; Ren, Z. High-Thermoelectric Performance of Nanostructured Bismuth Antimony Telluride Bulk Alloys. *Science* **2008**, *320*, 634-638.

(4) Joshi, G.; Lee, H.; Lan, Y.; Wang, X.; Zhu, G.; Wang, D.; Gould, R. W.; Cuff, D. C.; Tang, M. Y.; Dresselhaus, M. S.; Chen, G.; Ren, Z. Enhanced Thermoelectric Figure-of-Merit in Nanostructured p-type Silicon Germanium Bulk Alloys. *Nano Lett*. **2008**, *8*, 4670-4674.

(5) Bahk, J. H.; Bian, Z.; Shakouri, A. Electron Energy Filtering by a Nonplanar Potential to Enhance the Thermoelectric Power Factor in Bulk Materials. *Phys*. *Rev*. *B* **2013**, *87*, 075204-075216.

(6) Ortega, S.; Ibáñez, M.; Liu, Y.; Zhang, Y.; Kovalenko, M. V.; Cadavid, D.; Cabot, A. Bottom-up Engineering of Thermoelectric Nanomaterials and Devices from Solution-Processed Nanoparticle Building Blocks *Chem*. *Soc*. *Rev*. **2017**, *46*, 3510-3528.

(7) Goldsmid, J. H. Review of Thermoelectric Materials. In *Introduction to thermoelectricity*; Springer: Berlin, **2010**; pp 139-164.

(8) Chen, Z.; Guo, X.; Tang, J.; Xiong, F.; Li, W.; Chen, Y.; Ang, R. Extraordinary Role of Bi for Improving Thermoelectrics in Low Solubility SnTe−CdTe Alloys. *ACS Appl. Mater. Interfaces* **2019**, *11*, 26093-26099.

(9) Guo, X.; Chen, Z.; Tang, J.; Zhang, F.; Zhong, Y.; Liu, H.; Ang, R. Thermoelectric Transport Properties in Bi-doped SnTe–SnSe Alloys. *Appl. Phys. Lett.* **2020**, *116*, 103901.

(10) Li, W.; Zhou, C.; Li, L. A First-Principles Theoretical Study on the Thermoelectric Properties of the Compound $Cu_5AlSn_2S_8$. *J. Electron. Mater.* **2016**, *45*, 1453-1458.

(11) Dwivedi, P.; Miyata, M.; Higashimine, K.; Takahashi, M.; Ohta, M.; Kubota, K.; Takida, H.; Akatsuka, T.; Maenosono, S. Nanobulk Thermoelectric Materials Fabricated from Chemically Synthesized $Cu_3Zn_{1-x}Al_xSnS_{5-y}$ Nanocrystals. *ACS Omega* **2019**, *4*, 16402-16408.

(12) Roychowdhury, S.; Samanta, M.; Perumal, S.; Biswas, K. Germanium Chalcogenide Thermoelectrics: Electronic Structure Modulation and Low Lattice Thermal Conductivity. *Chem. Mater.* **2018**, *30*, 5799-5813.

(13) Yin, C.; Hu, Q.; Tang, M.; Liu, H.; Chen, Z.; Wang, Z.; Ang, R. Boosting the Thermoelectric Performance of Misfit-Layered $(SnS)_{1.2}(TiS_2)_2$ by a Co- and Cu-Substituted Alloying Effect. *J. Mater. Chem. A* **2018**, *6*, 22909-22914.

(14) Cui, J.; He, T.; Han, Z.; Liu, X.; Du, Z. Improved Thermoelectric Performance of Solid Solution $Cu_4Sn_{7.5}S_{16}$ through Isoelectronic Substitution of Se for S. *Sci. Rep.* **2018**, *8*, 8202.

(15) Bouroushian, M. *Electrochemistry of Metal Chalcogenides*; Springer: Berlin, **2010**; pp 16-52.

(16) Li, R.; Li, X.; Xi, L.; Yang, J.; Singh, D. J.; Zhang, W. High-Throughput Screening for Advanced Thermoelectric Materials: Diamond-Like $ABX_2$ Compounds. *ACS Appl. Mater. Interfaces* **2019**, *11*, 24859-24866.

(17) Bobone, R.; Kendall, L. F.; Vought, R. H. Thermoelectric Properties of Some Chalcopyrite-Type Compounds. *Adv. Energy Conv.* **1961**, *1*, 149.

(18) Sevik, C.; Çağın, T. Ab Initio Study of Thermoelectric Transport Properties of Pure and Doped Quaternary Compounds. *Phys. Rev. B* **2010**, *82*, 045202-045208.

(19) Wei, T.-R.; Wu, C.-F.; Li, F.; Li, J.-F. Low-cost and Environmentally Benign Selenides as Promising Thermoelectric Materials. *J. Materiomics* **2018**, *4*, 304-320.

(20) Coughlan, C.; Ibanez, M.; Dobrozhan, O.; Singh, A.; Cabot, A.; Ryan, K. M. Compound Copper Chalcogenide Nanocrystals. *Chem. Rev.* **2017**, *117*, 5865-6109.

(21) Trizio, L. D.; Manna, L. Forging Colloidal Nanostructures via Cation Exchange Reactions. *Chem. Rev.* **2016**, *116*, 10852-10887.

(22) Kumar, A.; Vermeulen, P. A.; Kooi, B. J.; Rao, J.; Eijck, L. V.; Schwarzmüller, S.; Oeckler, O.; Blake, G. R. Phase Transitions of Thermoelectric TAGS-85. *Inorg. Chem.* **2017**, *56*, 15091-15100.

(23) Biswas, K.; He, J.; Blum, I. D.; Wu, C. I.; Hogan, T. P.; Seidman, D. N.; Dravid, V. P.; Kanatzidis. High-Performance Bulk Thermoelectrics with All-Scale Hierarchical Architectures. *Nature* **2012**, *489*, 414-418.

(24) *Thermoelectrics: Design and Materials*; 1st Ed.; Lee, H. S., Ed.; Wiley: Chichester, UK, **2017**; pp 206-229.

(25) Thanh, N. T. K.; Maclean, N.; Mahiddine, S. Mechanisms of Nucleation and Growth of Nanoparticles in Solution. *Chem. Rev.* **2014**, *114*, 7610-7630.

(26) Pearson, R. G. Hard and Soft Acids and Bases, HSAB, Part II: Underlying theories. *J. Chem. Educ.* **1968**, *45*, 643-648.

(27) Shannon, R. D. Revised Effective Ionic Radii and Systematic Studies of Interatomic Distances in Halides and Chalcogenides. *Acta Cryst*. **1976**, *A32*, 751-767.

(28) Madras, G.; McCoy, B. J. Transition from Nucleation and Growth to Ostwald Ripening. *Chem*. *Eng*. *Sci*. **2002**, *57*, 3809-3818.

(29) Thermo Scientific XPS Reference Website. XPS Interpretation of Gallium. https://xpssimplified.com/elements/gallium.php (accessed January 16, 2020).

(30) Rodríguez-Carvajal, J. Recent Advances in Magnetic Structure Determination by Neutron Powder Diffraction. *Physica B Condens*. **1993**, *192*, 55-69.

(31) Crystallography Open Database Home Page. http://www.crystallography.net/cod/ (accessed November 6, 2019).

(32) Shevchenko, E. V.; Talapin, D. V.; Schnablegger, H.; Kornowski, A.; Festin, O.; Svedlindh, P.; Haase, M.; Weller, H. Study of Nucleation and Growth in the Organometallic Synthesis of Magnetic Alloy Nanocrystals: The Role of Nucleation Rate in Size Control of $CoPt_3$ Nanocrystals. *J. Am*. *Chem*. *Soc*. **2003**, *125*, 9090-9101.

(33) Choi, M.; Choi, H.; Kim, S.; Ahn, J.; Kim, Y. T. Lattice Distortion in $In_3SbTe_2$ Phase Change Material with Substitutional Bi. *Sci. Rep.* **2015**, *5*, 12867.

(34) Sun, Y.; Thompson, S. E.; Nishida, T. *Strain Effects in Semiconductors*: *Theory and Applications*; Springer: New York, USA, **2010**; pp 23-50.

(35) Williamson, G. K.; Hall, W. H. X-ray Line Broadening from Filed Aluminium and Wolfram. *Acta Metall*. **1953**, *1*, 22-31.

(36) Barry, C. C.; Grant, N. M. *Ceramic Materials*: *Science and Engineering*; Springer-Verlag: New York, 2007; pp 427-443.

(37) He, Y.; Day, T.; Zhang, T.; Liu, H.; Shi, X.; Chen, L.; Snyder, G. J. High Thermoelectric Performance in Non-Toxic Earth-Abundant Copper Sulfide. *Adv*. *Mater*. **2014**, *26*, 3974-3978.

(38) Suekuni, K.; Tsuruta, K.; Kunii, M.; Nishiate, H.; Nishibori, E.; Maki, S.; Ohta, M.; Yamamoto, A.; Koyano, M. High-performance Thermoelectric Mineral $Cu_{12-x}Ni_xSb_4S_{13}$ Tetrahedrite. *J*. *Appl*. *Phys*. **2013**, *113*, 043712-043716.

(39) Suekuni, K.; Kim, F. S.; Nishiate, H.; Ohta, M.; Tanaka, H. I.; Takabatake, T. High-performance Thermoelectric Minerals: Colusites $Cu_{26}V_2M_6S_{32}$ (M = Ge, Sn). *Appl*. *Phys*. *Lett*. **2014**, *105*, 132107-132110.

(40) Warnes, L. A. A. *Electronic Materials*; Springer: Boston, USA, **1990**; pp 84-117.

(41) Yu, Y.; Cagnoni, M.; Cojocaru-Mirédin, O.; Wuttig, M. Chalcogenide Thermoelectrics Empowered by an Unconventional Bonding Mechanism. *Adv*. *Funct*. *Mater*. **2020**, *30*, 1904862-1904880.

(42) Mishima, Y.; Kimura, Y.; Kim, S. W. Enhancement of Thermoelectric Figure of Merit through Nanostructural Control on Intermetallic Semiconductors toward High-Temperature Applications. In *Nanomaterials*: *From Research to Applications*, 1st Ed.; Hosono, H.; Mishima, Y.; Takezoe, H.; Mackenzie, K. J. D., Eds.; Elsevier Science: UK, **2006**; pp 383-418.

(43) Jonnard, P.; Capron, N.; Semond, F.; Massies, J.; Martinez-Guerrero, E.; Mariette. Electronic Structure of Wurtzite and Zinc-blende AlN. *Eur*. *Phys*. *J*. *B* **2004**, *42*, 351-359.

# Chapter 4

## Effect of $Cu_2SnS_3$ Nanoinclusions in $Cu_3AlSnS_5$ Nanobulk Materials on Thermoelectric Properties

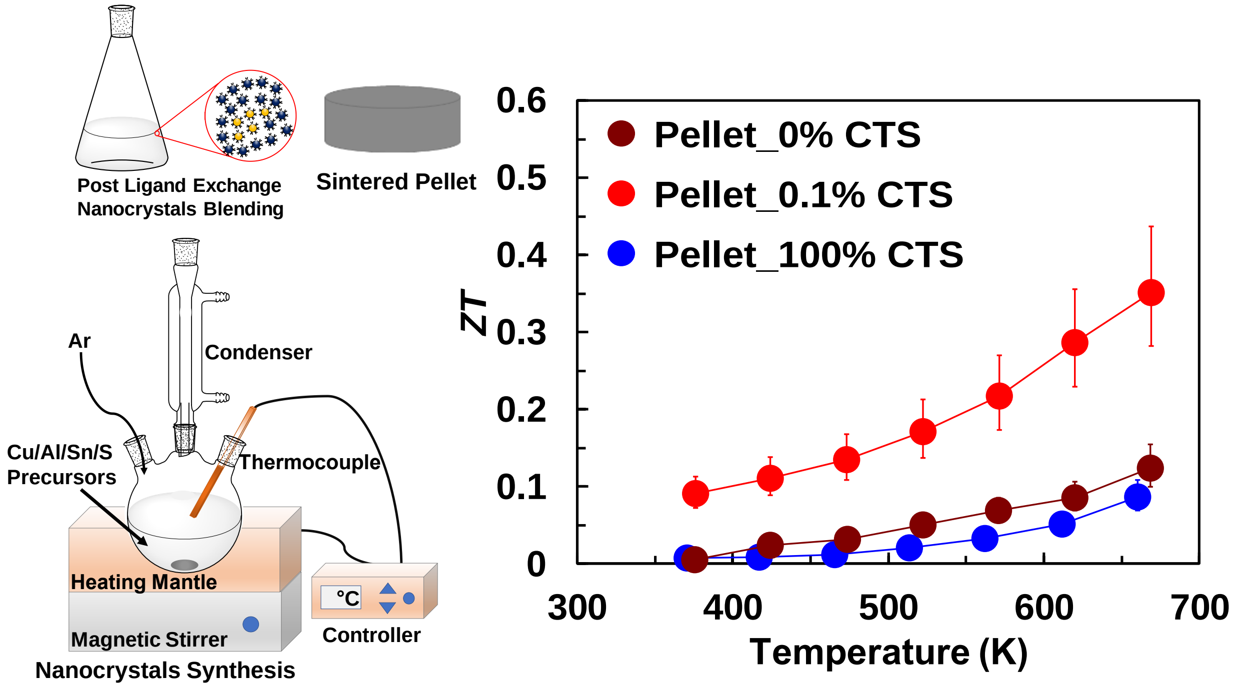

## 4.1 Introduction

Impending energy crisis demands judicious usage of energy in various forms.[1] Thermoelectric (TE) materials have long been recognized as a cost-effective and pollution-free technology due to their ability to convert heat energy directly into electric energy. The research on TE materials keeps exhibiting rapid improvement and exciting breakthroughs in the past twenty years due to the extensive investigation on nanostructured TE materials.[2-5] The conversion efficiency of TE materials is related to a quantity named the figure-of-merit ($ZT$) which is defined as $ZT=S^2\sigma/(\kappa_{\mathrm{lat}}+\kappa_{\mathrm{car}})$; where $S$ is the Seebeck coefficient; $\sigma$ is the electrical conductivity; $S^2\sigma$ is the power factor ($PF$); $T$ is the temperature (K); $\kappa_{\mathrm{lat}}$ and $\kappa_{\mathrm{car}}$ is the lattice and charge-carrier thermal conductivity respectively.[6] In energy harvesting applications, it has been a major challenge to boost the $ZT$ value of TE materials composed of earth-abundant and low-toxic elements.

Materials scientists are constantly exploring a extensive range of cost effective and eco-friendly TE materials which can be synthesized in bulk form. One of the strong TE material candidate includes copper based chalcogenides (S and Se); especially quaternary semiconductors ($Cu_2ZnSnSe_4$, $Cu_2ZnSnS_4$ (CZTS)) due to their complex crystal structure.[7-13] $ZT$ values for undoped $Cu_2ZnSnS_4$ remain quite low, ranging from $4.6 \times 10^{-5}$ at 300 K to 0.026 at 700 K and has huge scope to combat $\kappa_{\mathrm{lat}}$ and/or $PF$.[13] In last decade, the quaternary Cu-S based compounds acquired global attention with number of outstanding studies. Among these sulfide TE materials, the Cu-Al-Sn-S system has been predicted to possess a low $\kappa_{\mathrm{lat}}$ value based on the *ab-initio* calculations the incorporation of a Group IIIA element into the I-IV-VI system can significantly reduce the $\kappa_{\mathrm{lat}}$ via effective phonon scattering owing to its complex crystal structure.[14] Recently, we fabricated a $Cu_3AlSnS_5$ (CATS) nanobulk TE material using chemically-synthesized CATS nanocrystals and succeeded in achieving a $\kappa_{\mathrm{lat}}$ lower than shown by other quaternary Cu-M-Sn-S systems.[15] Despite the fact that CATS possess quite good *PF* due to dramatic increase in the $\sigma$ accompanied with substantially high $\kappa_{\mathrm{car}}$. Therefore, the $\kappa$ value of CATS is quite high even though it has an ultra-low $\kappa_{\mathrm{lat}}$, and thereby the *ZT* value remains low. A multifaceted strategy is required to reduce the $\kappa_{\mathrm{car}}$ of CATS without negatively impacting relatively high *PF* and ultra-low $\kappa_{\mathrm{lat}}$ values with the tuning of $\sigma$, for developing a promising sustainable TE material.

A decade ago, Dresselhaus *et al*. proposed that nanocomposite TE materials would offer a promising approach for the preparation of bulk samples with nano-sized constituents.[16] Broadly, there have been three main strategies for nanobulk TE materials fabrication. The first strategy uses single-phase nanograins, which primarily involves reduction of the thermal conductivity. The other two strategies are to form second-phase nanoinclusions, where a large number of interfaces are formed between the TE material and the nanoinclusions.[17,18] Right after bringing nanoinclusions concept in light, a variety of nanocomposites with improved TE properties than bulk materials have been prepared. For example, Li *et al*. prepared *n*-type skutterudites $\mathrm{In}_x\mathrm{Ce}_y\mathrm{Co}_4\mathrm{Sb}_{12}$ with in-situ forming nano-sized InSb phase, and attained the maximum *ZT* value of 1.43 was obtained at 800 K.[19] Chen *et al*. reported substantially reduced $\kappa$ and $\sigma$ with an enhanced $S$ was obtained from gallium antimonide (GaSb) dispersed in $\mathrm{Yb}_{0.26}\mathrm{Co}_4\mathrm{Sb}_{12}$ nanobulk material with improve *ZT* value of 1.45 at 850 K.[20] It shows apart from $\kappa_{\mathrm{lat}}$, the transport of charge carriers greatly influenced by the distribution of the secondary phases in the nanocomposite due to the scattering at the interfaces and influences the $\sigma$ and $S$.[21,22] Several theoretical studies explicitly exemplify the effective medium approximation; which predicts that the value of $\sigma$ and $\kappa$ of composites will be an average of the two phases without considering the effects of interface and grain boundaries[23,24]. For instance, Scherrer *et al*. synthesized and evaluated the TE properties of polycrystalline Bi and Bi–$\mathrm{SiO}_2$ nanocomposites and found that despite the substantial reduction in $\kappa_{\mathrm{lat}}$; the decrease in $\sigma$ due to finite-size effect compromised the *ZT* value.[25] On the other hand, a range of examples demonstrate the efforts towards optimization of nanoinclusion size, type and content leading to the reduction in $\kappa_{\mathrm{lat}}$, $\sigma$ and enhancing $S$; contributing for improving the *ZT* value. For instance, Girardin *et al*. reported PbTe bulk materials with uniformly distributed PbS nano-size dots leading to the *ZT* value 1.4 at 750K in the PbS(8%)-PbTe materials system.[26] Biswas *et al*. reported a *ZT* of 1.7 at 800K in PbTe-SrTe (SrTe = 0.52 mol%) materials doped with 1 mol% $Na_2Te$.[27] While, Poudeu *et al*. showed in $Na_{1-x}Pb_mSb_yTe_{m+2}$ systems, *ZT* = 1.7 at 700 K as a consequence of nanoinclusion.[28] In chalcogenides materials, Wei *et al*. reported the *ZT* value enhancement from 0.37 to 0.64 at 670 K, through blending of $Cu_2Sn_{1-x}Zn_xS_3$ compounds possessing varying level of Zn/Sn content.[29] Above-mentioned studies on TE materials with nanocomposite gave us some good inspirations. Recently, we found that the zincblende (ZB) rich nanobulk $Cu_3Al_{1-x}Ga_xS_5$ resulted *ZT* twice as higher than neat CATS.[30] Several chalocogenide materials shows the preference of more symmetric crystalline phase content and/or lower secondary crystalline phase to yield greater *ZT* value.[31,32] However, such peculiar correlation between material crystalline phase and transport properties has been largely ignored in the secondary phase containing copper-based quaternary chalcogenide nanoinclusion based TE system.

In current study, a systematic study has been made by introducing a well-defined shaped nanocrystal of $Cu_2SnS_3$ (CTS) in the CATS system and varied the loading of nanoinclusions (CTS) at 0.1, 1, 3, 5, 10 wt%. The CTS nanocrystals possess well defined particle shape with particle size and $\kappa_{\mathrm{lat}}$ similar to CATS but with substantially low $\sigma$. The nanoinclusion of CTS is expected to not only lowers the $\kappa_{\mathrm{lat}}$ but can modulate the crystallite phase content and $\sigma$ as well.[21] The TE properties of the resultant materials have been measured and studied the effect of CTS nanoinclusions in the CATS system.

## 4.2 Experimental

### *4.2.1 Materials*

The chemicals used for the synthesis of $Cu_3AlSnS_5$ (CATS) and $Cu_2SnS_3$ (CTS) samples are shown in Table 4.1. All chemicals have been used without purification.

**Table 4.1.** List of the chemicals, their chemical formula or abbreviation, and purity %.

| Chemicals | Chemical Formula / Abbreviation | Purity % |
|---|---|---|
| Copper(II) nitrate hydrate | $Cu(NO_3)_2{\cdot}xH_2O$ | 98.0 |
| Tin (II) acetate | $Sn(CH_3CO_2)_2$ / $Sn(OAc)_2$ | 99.0 |
| 1-Dodecanethiol | $CH_3(CH_2)_{11}SH$ / DDT | >98 |
| Oleylamine | $C_{18}H_{35}NH_2$ / OAM | 70.0 |
| Thiourea | $SC(NH_2)_2$ / TU | 99.0 |
| Hexane | $CH_3(CH_2)_4CH_3$ | 96.0 |
| Methanol | $CH_3OH$ | 99.8 |
| Toluene | $C_6H_5CH_3$ | 99.0 |

### *4.2.2 Synthesis of CATS and CTS Nanocrystals*

CATS nanocrystals were synthesized as mentioned in Chapter 2. For CTS nanocrystals the synthesis procedure mentioned as follows:

Firstly, 4 mmol of copper(II) nitrate hydrate [$Cu(NO_3)_2$], 2 mmol of tin(II) acetate [$Sn(OAc)_2$], 100 mL of oleylamine (OAM) and 100 mL of 1-dodecanethiol (DDT) were added into a 500 mL three-necked flask equipped with a dry Ar inlet/outlet, trap sphere, condenser, heating mantle, thermometer, and a magnetic stirrer. In starting, the reaction mixture was stirred with Ar bubbling at room temperature for 5 min. Thereafter the reaction temperature was increased to 100 °C and kept for 10 min with Ar bubbling to eliminate the volatile matter. Then, the reaction temperature was further raised to 260 °C and maintained for 1 h. After the reaction, the nanocrystals were separated from the reaction mixture by centrifugation process at 5000 rpm for 3 min; followed by the washing of the nanocrystals by repeating the following purification cycle: redispersion in hexane, addition of ethanol, centrifugation, and supernatant removal. Finally, the nanocrystals were dried in vacuum.

### *4.2.3 Ligand Exchange*

A thiourea (TU; Tokyo Chemical Industry, 10 g) solution was prepared in methanol (Kanto Chemical, 400 mL). The TU solution was added to a dispersion of the nanocrystals (3.4 g) in toluene (250 mL). The mixture was subjected to sonication for 1 h at room temperature. On completion of the ligand exchange reaction, the TU-capped nanocrystals were separated from the solution by centrifugation at 5000 rpm for 3 min. Subsequently, the TU-capped nanocrystals were washed through redispersion in a hexane/toluene mixture, centrifugation, and supernatant decantation. The excess TU was removed by following a washing procedure involving the redispersion of the TU-capped nanocrystals in methanol (400 mL) and then in toluene (125 mL) with centrifugation at 5000 rpm for 10 min.

### *4.2.4 Preparation of Blended Nanobulk Materials*

The blending of nanocrystals was pursued after the ligand exchange process.[29] Prior to the mixing, the TU capped CATS and TU capped CTS nanocrystals were separately dispersed in methanol. Afterwards, both nanocrystals dispersions were mixed in five different weight percentage as 99.9%

CATS + 0.1% CTS, 99% CATS + 1% CTS, 97% CATS + 3% CTS, 95% CATS + 5% CTS and 90% CATS + 10%CTS. After dispersion, the respective mixtures were centrifuged, and the resulting nanocrystals were dried in vacuum. The general synthetic scheme for blended material is shown in Figure 4.1.

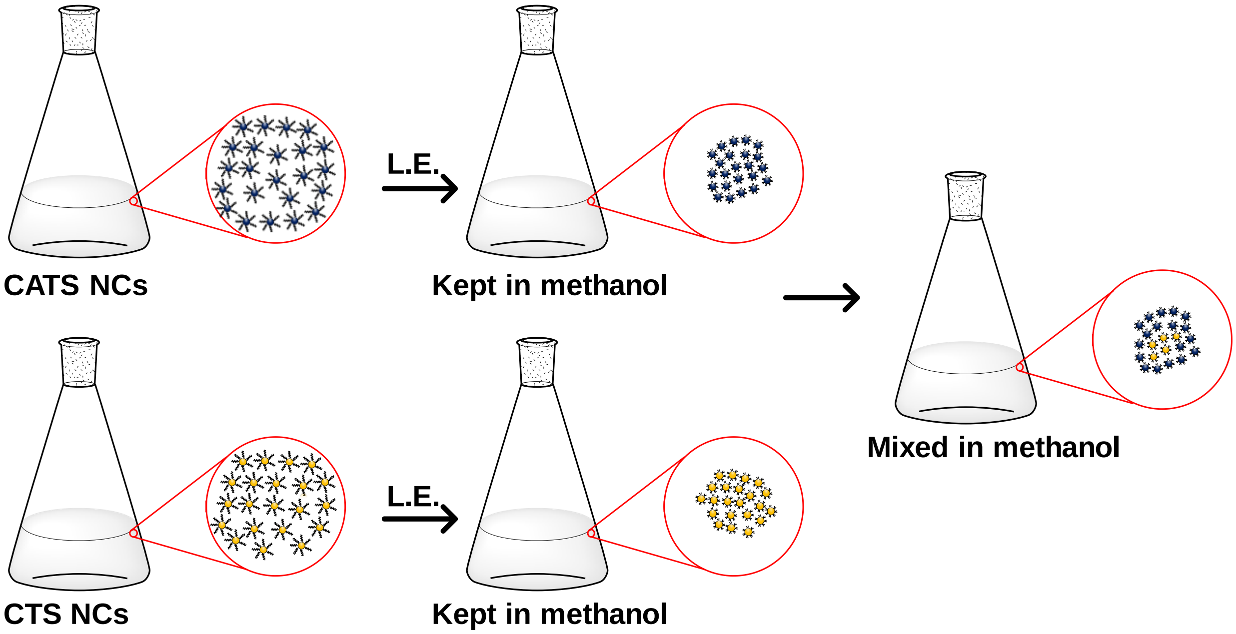

**Figure 4.1.** Illustration for ligand exchange followed by the blending of nanocrystals.

### *4.2.5 Pelletization*

The pulse electric current sintering machine (Sinterland LABOX-100) was employed to pelletize the blended nanocrystals into solid disks with diameter 10 mm and thickness of 2-3 mm, under following conditions: vacuum, 3.5 Pa; temperature, 450 °C; pelletization pressure, 30 MPa; and sintering time, 5 min. The pellets fabricated from **Powder_0.1% CTS**, **Powder_1% CTS**, **Powder_3% CTS**, **Powder_5% CTS**, **Powder_10% CTS**, and **Powder_100% CTS** are referred to as **Pellet_0.1% CTS**, **Pellet_1% CTS**, **Pellet _3% CTS**, **Pellet _5% CTS**, **Pellet _10% CTS**, and **Pellet_100% CTS** respectively. Pellets were polished using silicon carbide abrasive paper before the characterization. The densities of pellets were determined using a gas pycnometer (Shimadzu AccuPyc II 1340).

**Table 4.2.** The weight of CATS and CTS in blended nanobulk materials.

| Sample | CATS (g) | CTS (g) |
|---|---|---|
| **Pellet_0% CTS** | 0.85 | 0 |
| **Pellet_0.1% CTS** | 0.8491 | 0.0009 |
| **Pellet_1% CTS** | 0.8415 | 0.0085 |
| **Pellet_3% CTS** | 0.8245 | 0.0255 |
| **Pellet_5% CTS** | 0.8075 | 0.0425 |
| **Pellet_10% CTS** | 0.765 | 0.085 |
| **Pellet_100% CTS** | 0 | 0.85 |

## 4.3 Characterization Techniques

### *4.3.1 Structural and Compositional Analyses*

The synthesized nanocrystals were characterized by TEM (Hitachi H-7650 operated at 100 kV), XRD using a Rigaku Smartlab diffractometer with Cu K$\alpha$ radiation, STEM equipped with a high-angle annular dark-field (HAADF) detector and energy-dispersive X-ray spectroscopy (EDS) system (JEOL JEM-ARM200F operated at 200 kV) with a spherical aberration corrector and a nominal resolution 0.8 Å, SEM (Hitachi TM3030) equipped with an EDS system, and XPS (Shimadzu Kratos AXIS-ULTRA DLD).

### 4.3.2 Thermal Conductivity Measurement

The samples used for thermal conductivity measurements are solid disks (pellets) with diameter of 10 mm and thickness of 2-3 mm and prior to measurements the pellet surfaces were coated with graphite spray. First, $\kappa$ was measured for the pellets in the cross-plane direction by laser flash analysis (Netzsch LFA457). In this method, $\kappa$ (W $m^{-1}$ $K^{-1}$) was calculated as $\kappa = dcD$ where $d$ (kg $m^{-3}$), $c$ (J $kg^{-1}$ $K^{-1}$), and $D$ ($m^2$ $s^{-1}$) are the density, specific heat, and thermal diffusivity of the pellet, respectively. The values of $D$ were directly measured, while the values of $c$ were indirectly derived from a standard sample (Netzsch Pyroceram 9606) under an Ar flow of 100 mL·$min^{-1}$ over the temperature range of 300-670 K. The relative uncertainty of $\kappa$ was estimated to be smaller than 8% based on uncertainties of $d$, $c$ and $D$.

### 4.3.3 Electrical Transport Properties Measurements

After thermal conductivity measurement, all solid disks were cut into bars approximately 2 mm × 2 mm × 8 mm. The $S$ and $\sigma$ were measured in in-plane direction by ZEM-3 (ULVAC-Riko). The relative uncertainty of $S$ and $\sigma$ were estimated to be 5%. The $ZT$ values were calculated by considering those uncertainties. Power factor ($PF$) and $ZT$ values were calculated as $PF = \sigma S^2$ and $ZT = \sigma S^2 T/\kappa$, respectively.

## 4.4 Results and Discussion

### *4.4.1 Morphology and Compositional Analysis*

Figure 4.2 show the TEM images of synthesized CATS and CTS nanocrystals, respectively Both types of nanocrystals are uniform in size with hexagonal like morphology (some nanocrystals are standing up and others are lying down on the TEM grid). The average length and width of CATS nanocrystals are calculated to be 23 ± 2.3 nm and 18 ± 1.6 nm, respectively. The average length and width of CTS nanocrystals are also calculated to be 21 ± 4.5 nm and 15 ± 2.5 nm, respectively. The atomic percentage of Cu:Al:Sn of synthesized CATS and CTS nanocrystals were determined to be 63:19:18 and 69:31 respectively, by SEM-EDS.

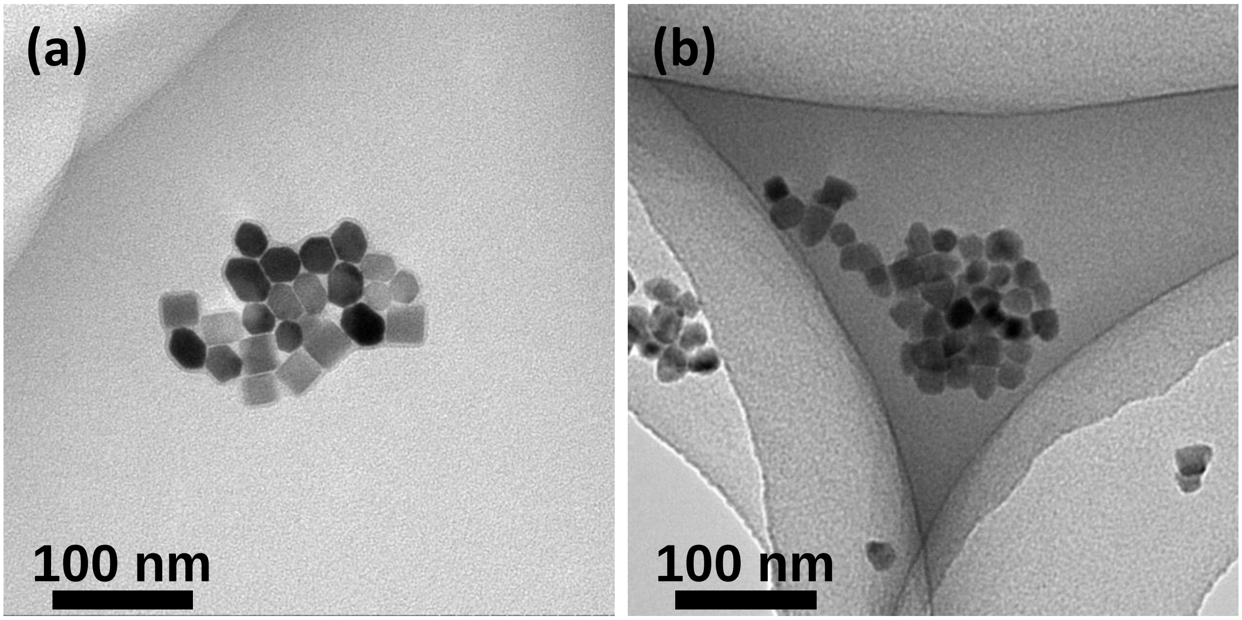

**Figure 4.2.** TEM images of (a) CATS and (b) CTS nanocrystals.

### *4.4.2 Crystal Structure of Nanocrystals and Pellets*

Figure 4.3 shows the XRD patterns of the CATS/CTS mixed nanocrystals referred as **Powder_0.1% CTS**, **Powder_1% CTS**, **Powder_3% CTS**, **Powder_5% CTS**, **Powder_10%**

**CTS**, and **Powder_100% CTS**. Rietveld refinement of the XRD patterns was performed with the FullPROF program[33] using wurtzite (WZ) and zinc blende (ZB) ZnS crystallographic information files.[34] Simulated patterns in which Cu, Sn, and Al ions randomly substitute Zn sites in the ZnS structure are shown as black lines. The primary crystal structure of all nanocrystals samples is WZ with small amount of ZB phase and nearly comparable in all of the samples. The lattice parameters for **Powder_0% CTS** and **Powder_100% CTS** are in range and appears CTS to be a wise choice as nanoinclusion.

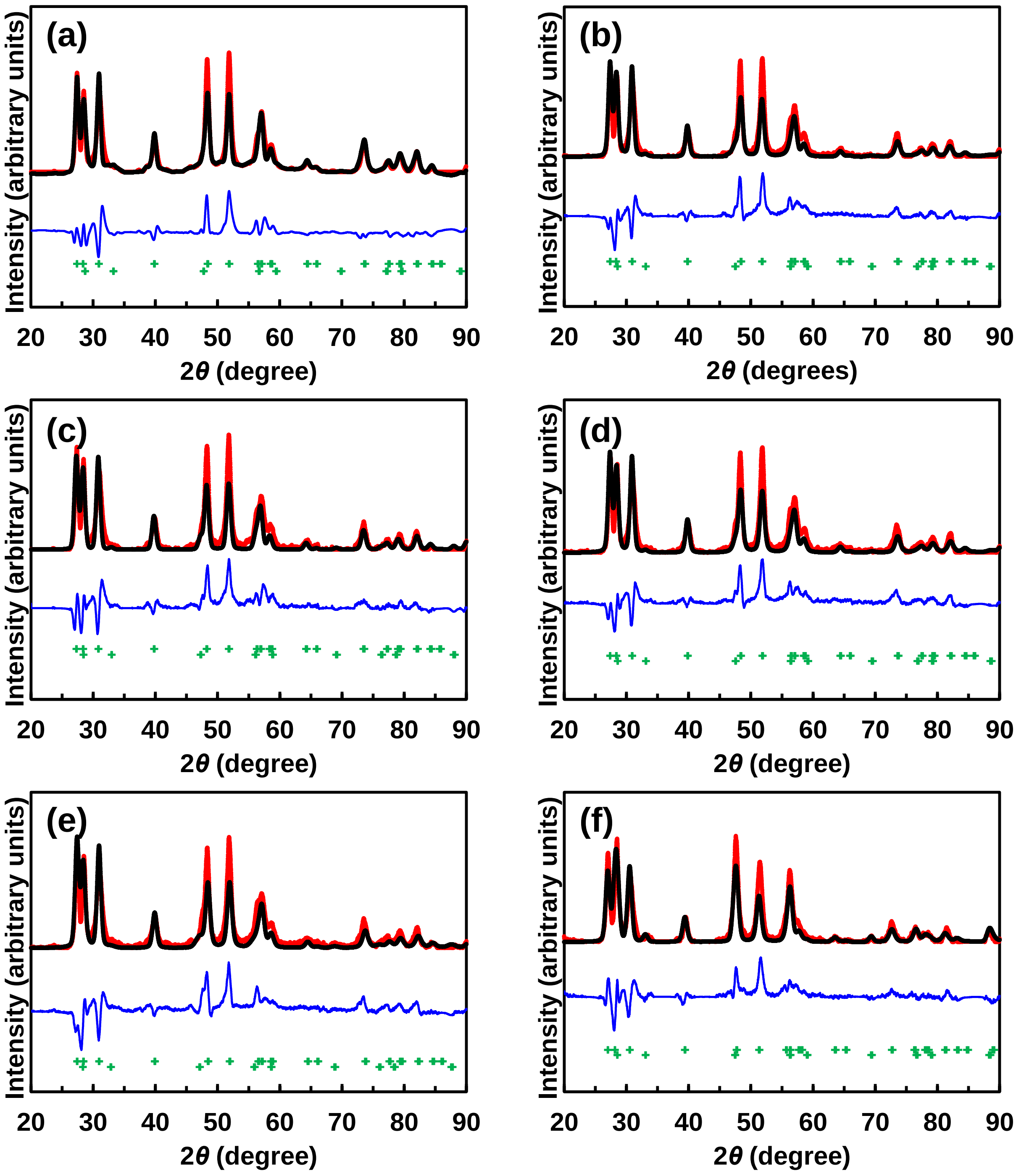

**Figure 4.3.** XRD Patterns of (a) **Powder_0.1% CTS**, (b) **Powder_1% CTS**, (c) **Powder_3% CTS**, (d) **Powder_5% CTS**, (e) **Powder_10% CTS**, and (f) **Powder_100% CTS**. The experimental patterns are shown by red lines, the Rietveld refined patterns using black lines and their difference by blue lines as well as the Bragg reflection positions shown as short green bars below the diffraction patterns.

Figure 4.4 shows the XRD patterns of CATS/CTS mixed nanobulk materials referred as **Pellet_0.1% CTS**, **Pellet_1% CTS**, **Pellet_3% CTS**, **Pellet_5% CTS**, **Pellet_10% CTS**, and **Pellet_100% CTS**. To perform quantitative phase-composition analysis of the pellets, Rietveld refinement of their XRD patterns was performed. Table 4.3 shows the weight percentage of the WZ and ZB phase in each pellet.

**Table 4.3.** WZ and ZB contents of CATS/CTS blended nanobulk materials.

| **Sample** | **WZ (wt%)** | **ZB (wt%)** |
|---|---|---|
| **Pellet_0% CTS** | 35 | 65 |
| **Pellet_0.1% CTS** | 24 | 76 |
| **Pellet_1% CTS** | 50 | 50 |
| **Pellet_3% CTS** | 58 | 42 |
| **Pellet_5% CTS** | 66 | 34 |
| **Pellet_10% CTS** | 76 | 24 |
| **Pellet_100% CTS** | 47 | 53 |

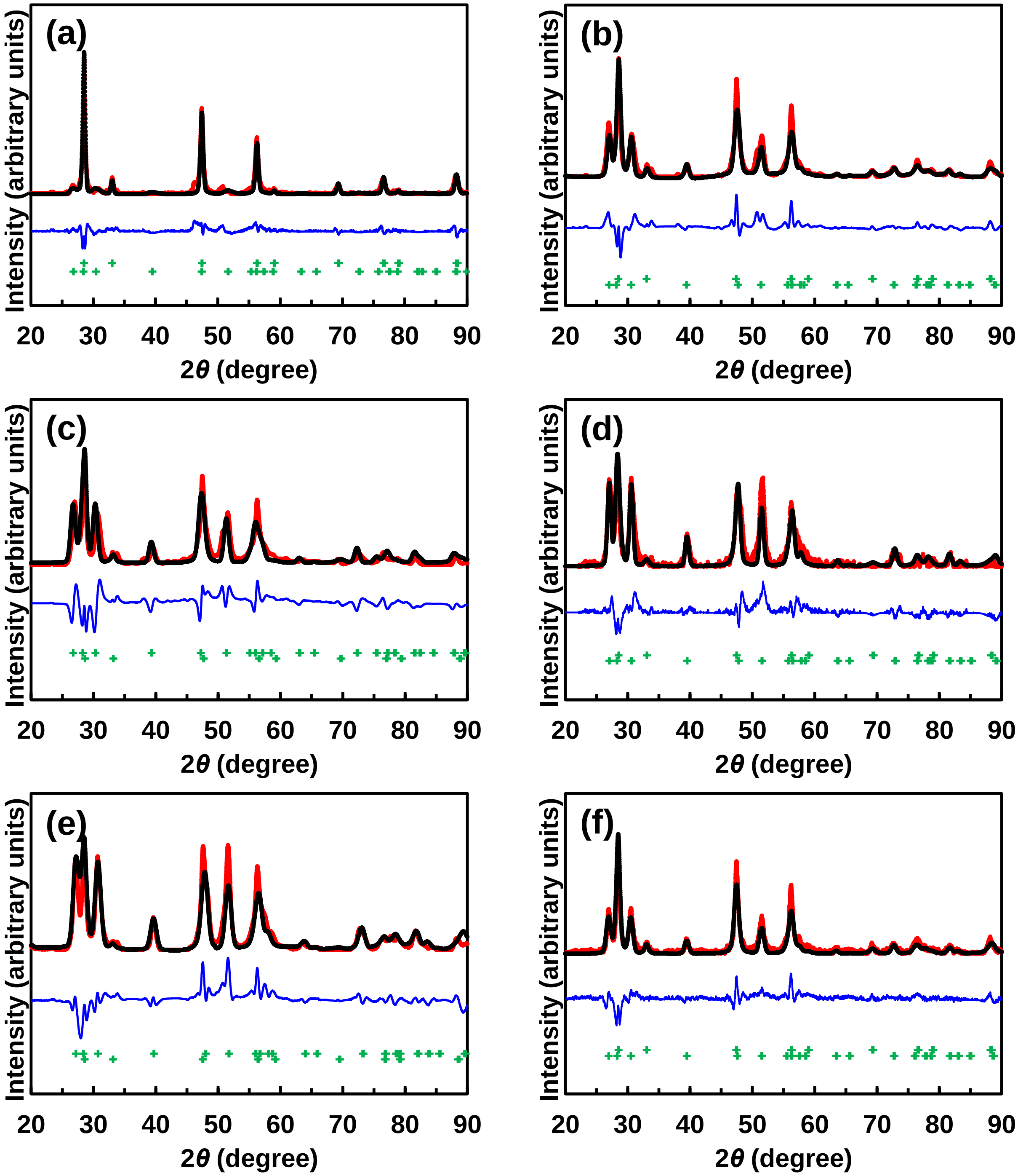

**Figure 4.4.** XRD Patterns of (a) **Pellet_0.1% CTS**, (b) **Pellet_1% CTS**, (c) **Pellet_3% CTS**, (d) **Pellet_5% CTS**, (e) **Pellet_10% CTS**, and (f) **Pellet_100% CTS**. The experimental patterns are shown by red lines, black lines represent the Rietveld refined patterns and their difference by blue lines as well as the Bragg reflection positions shown as short green bars below the diffraction patterns.

It was found that the pellets composed of CTS nanoinclusions with content equals or greater than 1 wt% CTS possess greater WZ phase content than the pristine samples. On the contrary, unlike others, the **Pellet_0.1%** CTS shows ZB as major phase. The measured densities of **Pellet_0% CTS**, **Pellet_0.1% CTS**, **Pellet_1% CTS**, **Pellet_3% CTS**, **Pellet_5% CTS**, **Pellet_10% CTS**, and **Pellet_100% CTS** were 4.356, 4.618, 4.44, 6.06, 5.50, 5.58, and 4.67 g·cm$^{-3}$, respectively.

The mean crystalline sizes ($D_{\mathrm{xrd}}$) were calculated using Scherrer's equation based on the most diffraction peak of the primary phase. The values of $D_{\mathrm{xrd}}$ for **Powder_0% CTS** and **Powder_100% CTS** are 9.1 and 9.9 nm respectively. The $D_{\mathrm{xrd}}$ values of **Pellet_0% CTS**, **Pellet_0.1% CTS**, **Pellet_1% CTS**, **Pellet_3% CTS**, **Pellet_5% CTS**, **Pellet_10% CTS**, and **Pellet_100% CTS** are calculated[35] to be 19.8, 16.2, 15.4, 16.1, 19.8, 19.2 and 18.5 nm respectively, indicates the increase in grain size upon sintering. Moreover, it is known that the nanoinclusions results the strained crystalline interfacial boundary; which increases the lattice strain ($\varepsilon$) of the resultant system.[21] The $\varepsilon$ was estimated using the Williamson-Hall method,[35] as shown in Figure 4.5. It was found that increment in CTS content as nanoinclusions leads to variation in the lattice strain as compared to the **Pellet_0% CTS** (pristine CATS). It was observed that the extent of lattice strain and content of relatively symmetrical crystalline phase (ZB) are inversely related for the given system.

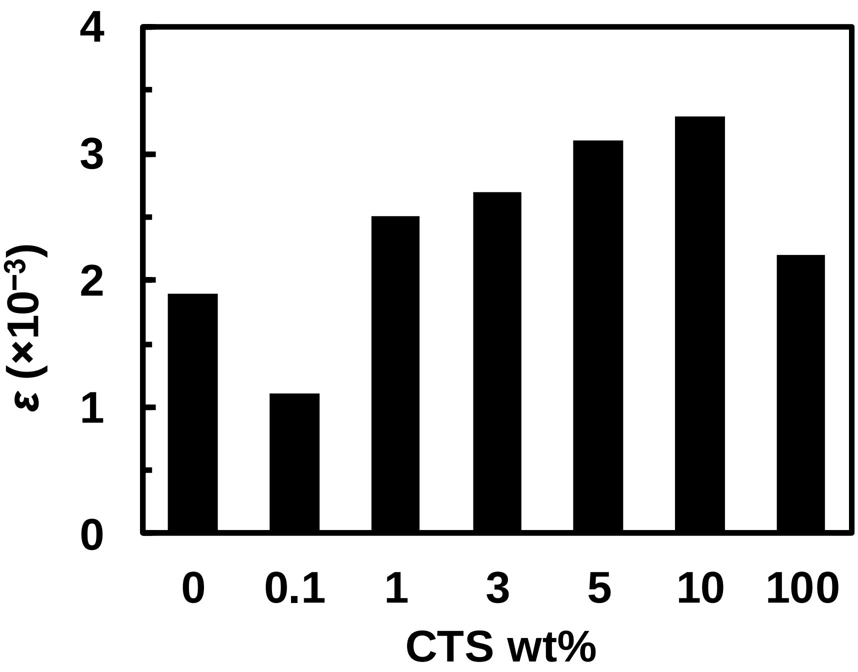

**Figure 4.5.** Lattice strain $\varepsilon$ plotted as a function of CTS wt%.

The Cu:Al:Sn atomic percentage of **Pellet_0% CTS**, **Pellet_0.1% CTS**, **Pellet_1% CTS**, **Pellet_3% CTS**, **Pellet_5% CTS**, **Pellet_10% CTS**, and **Pellet_100% CTS** were determined from SEM-EDS and summarized in Table 4.4.

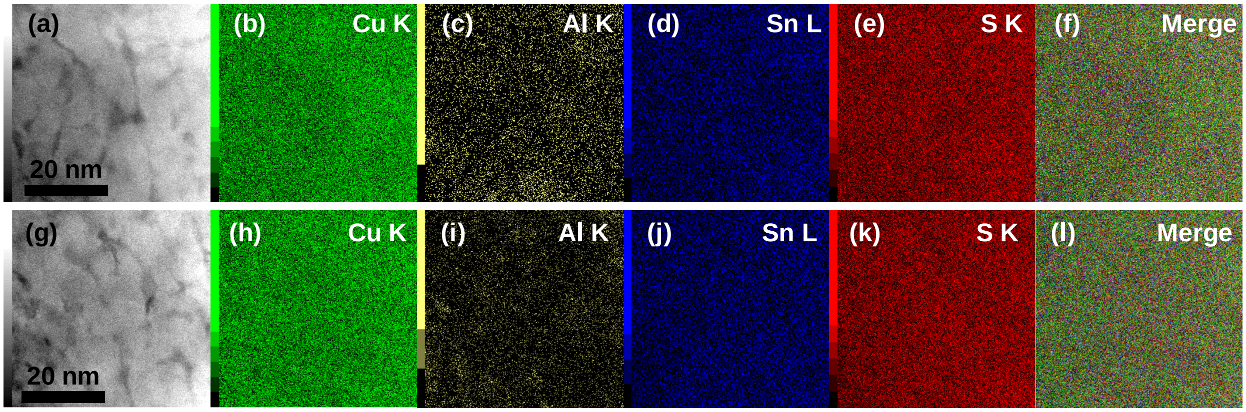

**Figure 4.6.** Cross-sectional HAADF-STEM and corresponding EDS elemental mapping images for Cu, Al, Sn, and S of the (a-f) **Pellet_1% CTS** and, (g-l) **Pellet_5% CTS** nanobulk materials.

**Table 4.4.** Atomic compositions for **Powder_0% CTS**, **Powder_0.1% CTS**, **Powder_1% CTS**, **Powder_3% CTS**, **Powder_5% CTS**, **Powder_10% CTS**, **Powder_100% CTS** and **Pellet_0% CTS**, **Pellet_0.1% CTS**, **Pellet_1% CTS**, **Pellet_3% CTS**, **Pellet_5% CTS**, **Pellet_10% CTS**, **Pellet_100% CTS** using SEM-EDS.

| **Sample** | **SEM-EDS** | | |
|---|---|---|---|
| | **Cu (at%)** | **Al (at%)** | **Sn (at%)** |
| **Powder_0% CTS** | 62 | 20 | 18 |
| **Pellet_0% CTS** | 61 | 22 | 17 |
| **Powder_0.1% CTS** | 63 | 19 | 18 |
| **Pellet_0.1% CTS** | 62 | 19 | 19 |
| **Powder_1% CTS** | 63 | 18 | 19 |
| **Pellet_1% CTS** | 64 | 17 | 19 |
| **Powder_3% CTS** | 63 | 19 | 18 |
| **Pellet_3% CTS** | 63 | 19 | 18 |
| **Powder_5% CTS** | 65 | 16 | 19 |
| **Pellet_5% CTS** | 66 | 15 | 19 |
| **Powder_10% CTS** | 66 | 16 | 18 |
| **Pellet_10% CTS** | 64 | 17 | 19 |
| **Powder_100% CTS** | 69 | 0 | 31 |
| **Pellet_100% CTS** | 68 | 0 | 32 |

The cross-sectional HAADF-STEM and EDS elemental mapping images of **Pellet_1% CTS** and **Pellet_5% CTS** are shown in Figure 4.6. The contrast of STEM-HAADF image is relatively uniform in both cases. The EDS elemental mapping images also confirm that the pellets are compositionally uniform. However, because the difference in composition between **Pellet_1% CTS** and **Pellet_5% CTS** is quite small, it was extremely difficult to visualize the CTS nanoinclusions in CATS system.

### *4.4.3 Thermoelectric Properties*

The TE properties of **Pellet_0% CTS**, **Pellet_0.1% CTS**, **Pellet_1% CTS**, **Pellet_3% CTS**, **Pellet_5% CTS**, **Pellet_10% CTS** and **Pellet_100 CTS** are shown in Figure 4.7. In Figure 4.7 (a), the $\sigma$ for **Pellet_0% CTS and Pellet_0.1% CTS** decreases with temperature, indicating their metallic behavior.[9] However, CTS-containing pellets (1wt% CTS onwards: **Pellet_1% CTS**, **Pellet_3% CTS**, **Pellet_5%**, **Pellet_10% CTS** and **Pellet_100 % CTS**) showed the increase in $\sigma$ with temperature, which indicates their semiconductor behavior. It is noteworthy that the $\sigma$ values of **Pellet_0% CTS** were one or two orders of magnitude higher than those of the other pellets, as well as other high-performance copper-sulfide-based TE materials including $Cu_{1.97}S$,[36] $Cu_{10}Ni_2Sb_4S_{13}$,[37] and $Cu_{26}V_2Sn_6S_{32}$.[38] Figure 4.7 (b) illustrates the temperature dependence of $S$. In general, $S$ depends inversely on $\sigma$, and therefore a decrease in $\sigma$ with increasing CTS content enhances $S$. In other words, the increased $S$ values for the CTS containing pellets over that of **Pellet_0% CTS** (CATS) may be owing to the lower value of $p$.

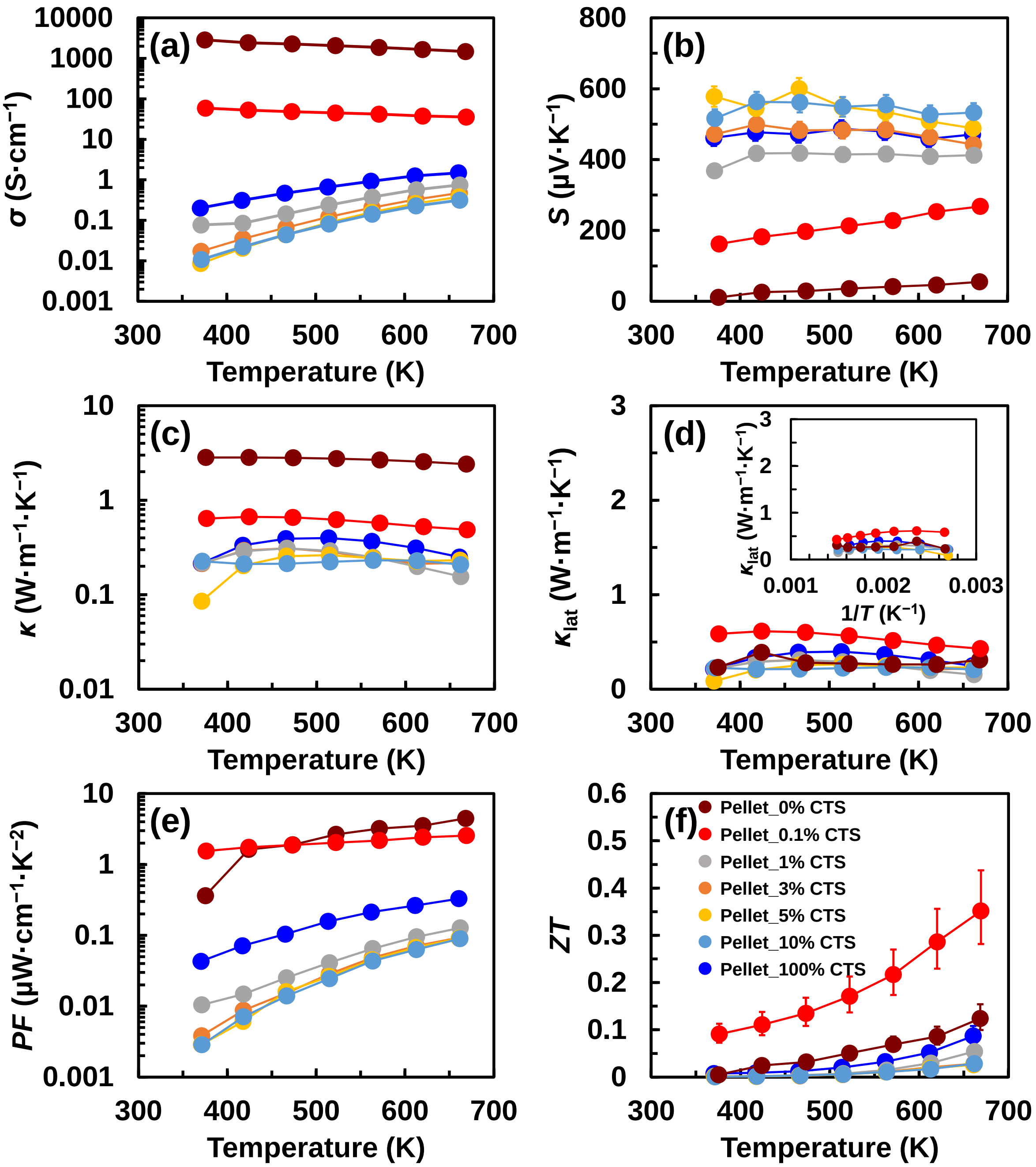

**Figure 4.7.** (a) Electrical conductivity *σ*, (b) Seebeck coefficient *S*, (c) total thermal conductivity *κ*, (d) lattice thermal conductivity $\kappa_{\text{lat}}$, (e) power function *PF*, and (f) dimensionless figure of merit *ZT* values of **Pellet_0% CTS** (brown circles), **Pellet_0.1% CTS** (red circles), **Pellet_1% CTS** (gray circles), **Pellet_3% CTS** (orange circles), **Pellet_5% CTS** (yellow circles), **Pellet_10% CTS** (sky blue circles) and **Pellet_100% CTS** (royal blue circles). The inset of (d) shows $\kappa_{\text{lat}}$ plotted with respect to the reciprocal of temperature.

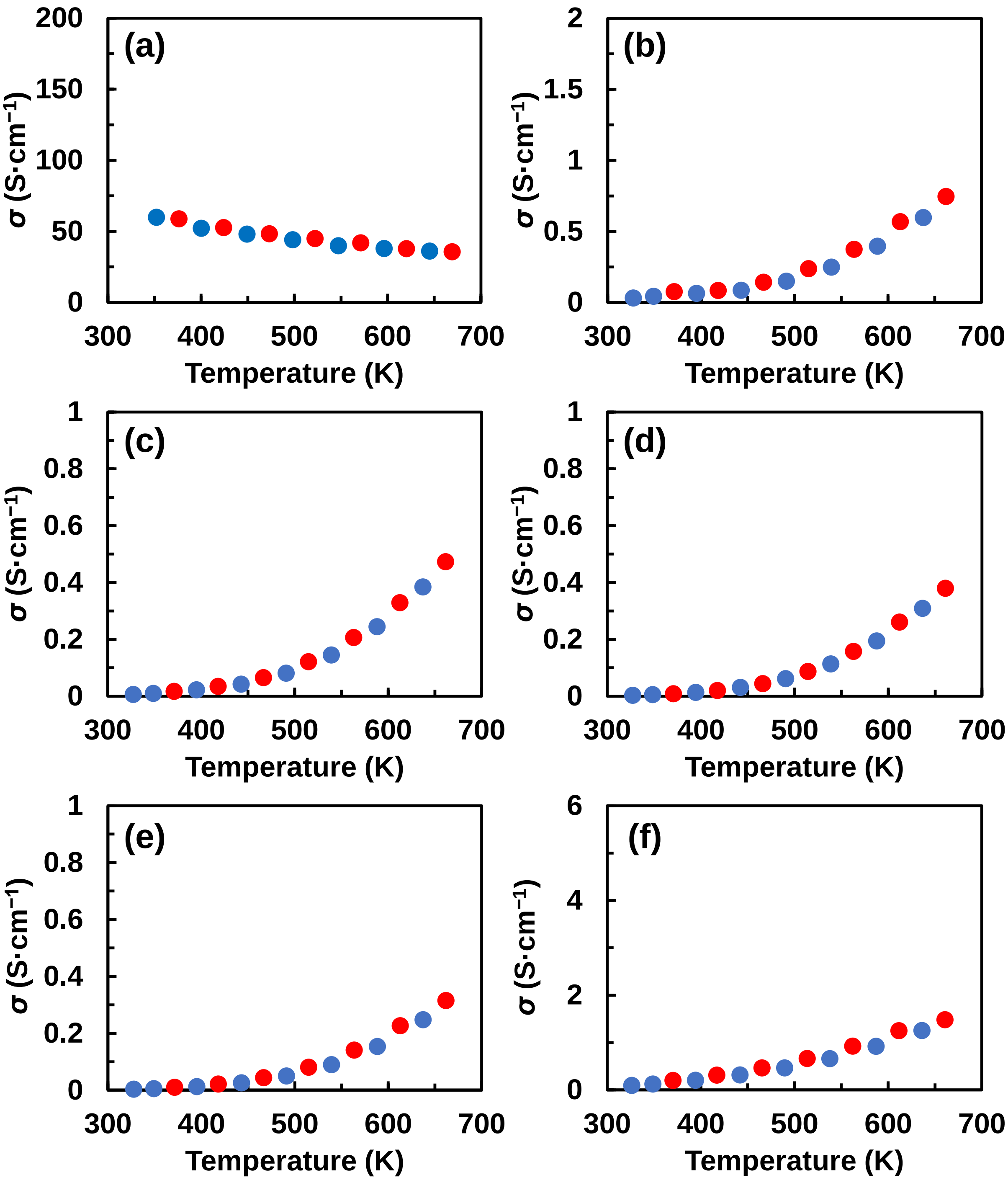

**Figure 4.8.** Electrical conductivities of (a) **Pellet_0.1% CTS**, (b) **Pellet_1% CTS**, (c) **Pellet_3% CTS**, (d) **Pellet_5% CTS**, (e) **Pellet_10% CTS**, and (f) **Pellet_100% CTS**. Red and blue circles represent data measured in heating and cooling cycles, respectively.

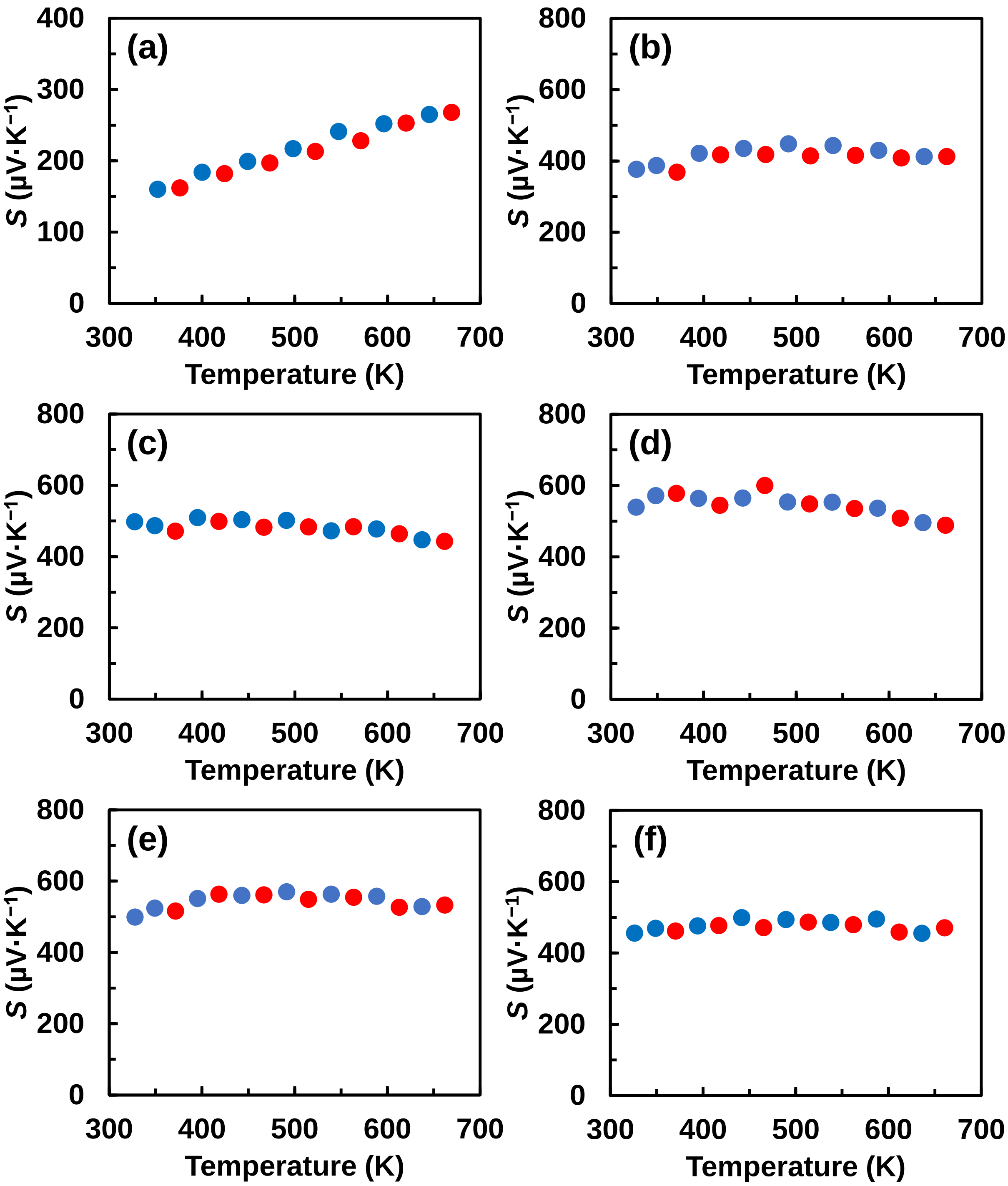

**Figure 4.9.** Seebeck coefficients of (a) **Pellet_0.1% CTS**, (b) **Pellet_1% CTS**, (c) **Pellet_3% CTS**, (d) **Pellet_5% CTS**, (e) **Pellet_10% CTS**, and (f) **Pellet_100% CTS**. Red and blue circles represent data measured in heating and cooling cycles, respectively.

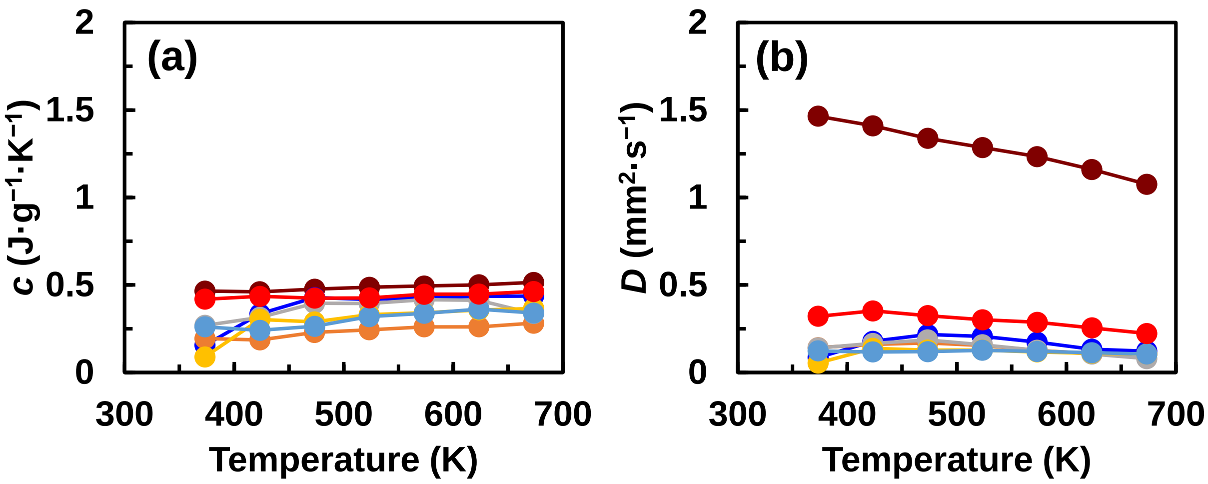

**Figure 4.10.** (a) Specific heat (*c*) and (b) Thermal diffusivity (*D*) of nanobulk materials.

In general, greater content of more ordered crystal phase yields more band degeneracy and thereby contribute towards enhancement in *S*.[39, 40] On the other hand, the nanoinclusions of CTS in the CATS system leads to change in the ordered phase structure in-line with the $\varepsilon$ as shown in Table 4.3 and Figure 4.5. Therefore, the exact reason for the enhancement variation is *S* can be attributed to either low *p* and/or electronic band structure properties of the material originating due to complex multiphasic (WZ and ZB) crystallographic system.

Figure 4.7 (c) displays the temperature dependence of $\kappa$, where the $\kappa$ values are less than 1.0 $\mathrm{W \cdot m^{-1} \cdot K^{-1}}$ for all pellets except **Pellet_0% CTS**. Figure 4.7 (d) shows $\kappa_{\mathrm{lat}}$ plotted as a function of temperature, where no apparent temperature dependence can be observed. This lack of temperature dependence is more evident in the inset of Figure 4.7 (d) indicates that the phonon scattering is dominated by defect scattering, which includes nanograins and lattice distortion caused by the nanoinclusions.[5] As mentioned earlier, the high $\kappa$ value of **Pellet_0% CTS** is owing to a high $\kappa_{\mathrm{car}}$ value. The efficient reduction of $\kappa_{\mathrm{car}}$ is evident with the suppression $\sigma$ for CTS containing pellets.

Note that $\sigma$ and $S$ were measured during both the heating and cooling cycle and the values were found to coincide in both cycle types, as shown in Figure 4.8 and Figure 4.9. The absence of any noticeable hysteresis shows the data reproducibility as well as the thermodynamic stability for all the samples. The specific heat and thermal diffusivity of all pellet samples are provided in Figure 4.10 (a) and (b) respectively.

Figure 4.7 (e) and (f) show the temperature dependence of $PF$ and $ZT$, respectively. Because of its high $\sigma$, **Pellet_0% CTS** exhibited the highest $PF$ among all pellets, though its $ZT$ value was 0.12 (at 668 K) owing to its high $\kappa$. Initially, **Pellet_1% CTS**, **Pellet_3% CTS**, **Pellet_5% CTS** and **Pellet_10% CTS** were fabricated and found that even though $S$ increased dramatically in the CTS containing pellets but certainly not enough to compensate the substantial reduction in $\sigma$ and thereby paving a way for $PF$ lower than the **Pellet_0% CTS**. Interestingly, as we decided to fabricate **Pellet_0.1% CTS**, we found that the $\sigma$ and $S$ were balanced with a better trade-off to yield a much higher $PF$ than other CTS containing pellets. Thereby, the contribution of suppressed $\kappa$ was found to be enough to increase the $ZT$ value. It is interesting to observe that the increase in the CTS nanoinclusions leads to gradual clamped down in the $\sigma$. To understand the reason for the variation of $\sigma$ with respect to CTS content, the activation energy $E_{\mathrm{a}}$ was estimated using the Arrhenius equation[41]

$$\sigma = \sigma_0 \exp\left(-\frac{E_{\mathrm{a}}}{k_{\mathrm{B}}T}\right), \tag{4.1}$$

where $k_B$ is the Boltzmann constant, and $T$ is the absolute temperature. Figure 4.11 (a) reveals that the CTS containing pellets exhibit a linear correlation between ln $\sigma$ and 1/$T$.

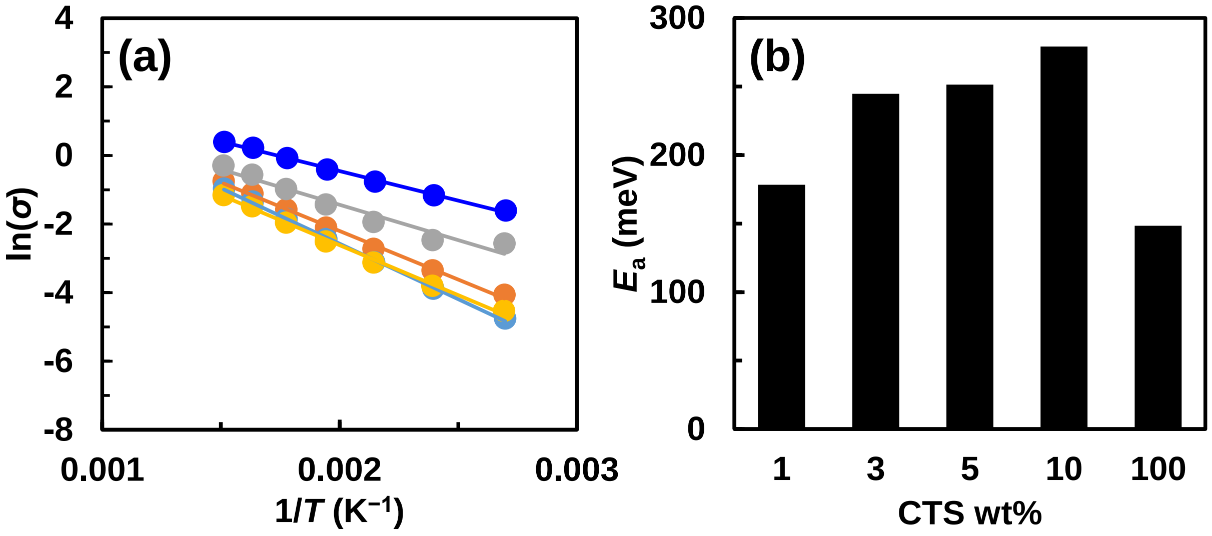

**Figure 4.11.** (a) Arrhenius plot and (b) activation energy $E_a$ plotted with respect to CTS wt% for **Pellet_1% CTS** (gray circles), **Pellet_3% CTS** (orange circles), **Pellet_5% CTS** (yellow circles), **Pellet_10% CTS** (sky blue circles) and **Pellet_100% CTS** (royal blue circles).

The values of $E_a$ were then plotted as a function of CTS wt% as shown in Figure 4.11 (b), exhibiting a correlation between $E_a$ and CTS wt%. Within the nanobulk samples (1 wt%, 3 wt%, 5 wt%, 10 wt% and 100 wt% CTS), minimum $E_a$ was observed for **Pellet_100% CTS**, indicating that it has the highest $\sigma$ among the samples. **Pellet_0% CTS and Pellet_0.1% CTS** were not included in the analyses primarily because its electronic nature was different (i.e., metallic) from the other pellets (i.e., semiconductor). Therefore, $p$ and carrier mobility ($\mu$) were estimated using the free electron model, in which the Fermi energy $E_F$ can be described as

$$E_F = \frac{\hbar^2 k_F{}^2}{2m} \tag{4.2}$$

where $\hbar$ is the Dirac constant, $k_F = (3\pi^2 n)^{1/3}$ is the wave number at the Fermi surface, and $n$ is the carrier concentration. We assumed that an acoustic phonon scattering of carriers is dominant at high temperature region. According to this assumption, $S$ can be described as below,

$$\sigma = A\varepsilon^{\gamma} \tag{4.3}$$

$$S = -\frac{\pi^2 {k_B}^2 T}{3e} \frac{\mathrm{d}\ln\sigma}{\mathrm{d}\varepsilon}\bigg|_{\varepsilon=E_F} = \frac{\pi^2 {k_B}^2}{6eE_F} T \tag{4.4}$$

where $A$ is the arbitrary constant, $\varepsilon$ is the energy, $\gamma$ is the scattering parameter, $k_B$ is the Boltzmann constant, and $e$ is the elementary charge. When the carrier scattering is dominated by acoustic phonon scattering, $\gamma = -1/2$. From Eqs. (4.2)−(4.4), the values of $p$ and $\mu$ were estimated as shown in Table 4.5.

**Table 4.5** $p$ and $\mu$ estimated from the values of $S$ and $\sigma$ (at 375 K).

| **Sample** | **$S$ (μV·K$^{-1}$)** | **$\sigma$ (S·cm$^{-1}$)** | **$p$ (cm$^{-3}$)** | **$\mu$ (cm$^2$·V$^{-1}$·s$^{-1}$)** |
|---|---|---|---|---|
| **Pellet_0% CTS** | 14 | 2801 | $8.5\times10^{20}$ | 21 |
| **Pellet_0.1% CTS** | 163 | 54 | $2.1\times10^{19}$ | 16 |

These results clearly show that the CTS nanoinclusions in CATS system leads to the lower $\sigma$ due to the suppressed $p$.

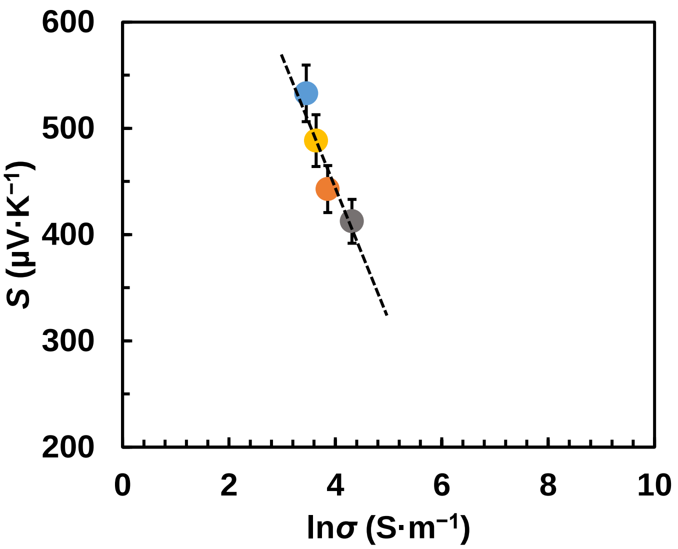

**Figure 4.12.** Seebeck coefficient plotted with respect to ln($\sigma$) for **Pellet_1% CTS** (gray circles), **Pellet_3% CTS** (orange circles), **Pellet_5% CTS** (yellow circles), and **Pellet_10% CTS** (sky blue circles).

On the other hand, in case of pellets with CTS content over 0.1 wt%, $S$ and ln$\sigma$ were plotted at 660 K (Figure 4.12) to understand the reason for lower $\sigma$ with increase in CTS content. The Jonker plot[42] shows a linear relationship between with $S$ and ln$\sigma$ and thereby suggests similar $\mu$ for all the blended pellets. In other words, the pellets showing decrease in $\sigma$ with increase in CTS content with similar $\mu$ could be attributed to the lower $p$. Therefore, this study represents an interesting methodology for gradual curtailment of the $\sigma$ in combination with the crystallographic phase content towards improvement of the $ZT$ value. The methodology may be extended to other similar systems, however, exploration of mechanistic aspect regarding origin and role of multiple crystallographic phase in electronic and thermal properties represents a stimulating and plausible opportunity for more advanced TE materials development.

## 4.5 Conclusions

A series of CTS nanoinclusion in CATS nanobulk TE materials were fabricated. The effect of CTS nanoinclusions content on the TE properties have been evaluated. CTS nanoinclusions, 1 wt% onwards, gradually increases the less ordered (WZ) crystal phase content in the nanobulk materials and leads to the formation of semiconductor material with WZ as major phase. The increase in CTS as nanoinclusions was found to contribute towards greater lattice strain. It was found that CTS nanoinclusions have suppressed the $\sigma$ substantially leading to significant reduction in $\kappa_{\text{car.}}$; on the other hand, $\kappa_{\text{lat}}$ was largely maintained or further curtailed. Despite reduction in $\kappa$ and increment in $S$, the $ZT$ value could not be enhanced owing to the overly curbed $\sigma$ with the CTS nanoinclusions. However, at 0.1 wt% CTS nanoinclusions a better trade-off between $\sigma$ and $S$ was achieved without compromising $\kappa$ and thus improved the $ZT$ value 3× than neat CATS system. The 0.1 wt% CTS containing sample possess greater ZB phase content than any other pellets under consideration and prevail the importance of symmetric crystal structure content in deciding the fate of TE properties. This research gives crucial insight from the viewpoint of crystallite phase type, content and methodology of blending process in understanding the behavior of material transport characteristics.

# References

(1) IRENA, REthinking Energy **2017**: Accelerating the global energy transformation. International Renewable Energy Agency, Abu Dhabi. (Weblink: https://www.irena.org/-/media/Files/IRENA/Agency/Publication/2017/IRENA_REthinking_Energy_2017.pdf?la=en&hash=38EF7869A341CC05ADC76C9B56BE7556BA5826E2).

(2) Wolf, M.; Hinterding, R.; Feldhoff. High Power Factor vs. High *ZT*—A Review of Thermoelectric Materials for High-Temperature Application. *Entropy* **2019**, *21*, 1058.

(3) Biswas, K.; He, J.; Blum, I. D.; Wu, C. I.; Hogan, T. P.; Seidman, D. N.; Dravid, V. P.; Kanatzidis. High-Performance Bulk Thermoelectrics with All-Scale Hierarchical Architectures. *Nature* **2012**, *489*, 414-418.

(4) Snyder, G. J.; Toberer, E. S. Complex Thermoelectric Materials. *Nat. Mater*. **2008**, *7*, 105-114.

(5) Kishore, R. A.; Priya, S. A Review on Low-Grade Thermal Energy Harvesting: Materials, Methods and Devices. *Materials* **2018**, *11*, 1433.

(6) Altenkirch, E. Elektrothermische Kälteerzeugung und reversible elektrische Heizung. *Phys. Z*. **1911**, 12, 920-924.

(7) Liu, M-. L.; Huang, Q-. F.; Chen, L-. D.; Chen, I-. W. A Wide-Band-Gap *p*-type Thermoelectric Material Based on Quaternary Chalcogenides of $Cu_2ZnSnQ_4$ (Q = S, Se). *Appl. Phys. Lett*. **2009**, *94*, 202103.

(8) Zhang, J.; Liu, R.; Cheng, N.; Zhang, Y.; Yang, J.; Uher, C.; Shi, X.; Chen, L.; Zhang, W. High-Performance Pseudocubic Thermoelectric Materials from Non-cubic Chalcopyrite Compounds. *Adv. Mater*. **2014**, *26*, 3848-3853.

(9) Liu, Q.; Zhao, Z.; Lin, Y.; Guo, P.; Li, S.; Pan, D.; Ji, X. Alloyed $(ZnS)_x(Cu_2SnS_3)_{1-x}$ and $(CuInS_2)_x(Cu_2SnS_3)_{1-x}$ Nanocrystals with Arbitrary Composition and Broad Tunable Band Gaps. *Chem. Commun*. **2011**, *47*, 964-966.

(10) Coughlan, C.; Ibanez, M.; Dobrozhan, O.; Singh, A.; Cabot, A.; Ryan, K. M. Compound Copper Chalcogenide Nanocrystals. *Chem. Rev*. **2017**, *117*, 5865-6109.

(11) Singh, A.; Geaney, H.; Laffir, F.; Ryan, K. M. Colloidal Synthesis of Wurtzite $Cu_2ZnSnS_4$ Nanorods and Their Perpendicular Assembly. *J. Am. Chem. Soc*. **2012**, *134*, 2910-2913.

(12) Zhou, W.; Shijimaya, C.; Takahashi, M.; Miyata, M.; Mott, D.; Koyano, M.; Ohta, M.; Akatsuka, T.; Ono, H.; Maenosono, S. Sustainable Thermoelectric Materials Fabricated by using $Cu_2Sn_{1-x}Zn_xS_3$ Nanoparticles as Building Blocks. *Appl. Phys. Lett*. **2017**, *111*, 263105.

(13) Yang, H.; Jauregui, L. A.; Zhang, G.; Chen, Y. P.; Wu, Y. Nontoxic and Abundant Copper Zinc Tin Sulfide Nanocrystals for Potential High-Temperature Thermoelectric Energy Harvesting. *Nano Lett*. **2012**, *12*, 540-545.

(14) Li, W.; Zhou, C.; Li, L. A First-Principles Theoretical Study on the Thermoelectric Properties of the Compound $Cu_5AlSn_2S_8$. *J. Electronic Mater*. **2015**, *45* (3), 1453-1458.

(15) Dwivedi, P.; Miyata, M.; Higashimine, K.; Takahashi, M.; Ohta, M.; Kubota, K.; Takida, H.; Akatsuka, T.; Maenosono, S. Nanobulk Thermoelectric Materials Fabricated from Chemically Synthesized $Cu_3Zn_{1-x}Al_xSnS_{5-y}$ Nanocrystals. *ACS Omega* **2019**, *4*, 16402-16408.

(16) Dresselhaus, M. S.; Chen, G.; Tang, M. Y.; Yang, R.; Lee, H.; Wang, D.; Ren, Z.; Fleurial, J.-, P.; Gogna, P. New Directions for Low-Dimensional Thermoelectric Materials. *Adv. Mater*. **2007**, *19*, 1043-1053.

(17) *Thermoelectrics Handbook: Macro to Nano*; $1^{st}$ Ed.; Rowe, D. M., Ed.; CRC Press: Boca Raton, FL, USA, **2006**; pp. 14-01–14-10.

(18) Zebarjadi, M.; Joshi, G.; Zhu, G.; Yu, B.; Minnich, A.; Lan, Y.; Wang, X.; Dresselhaus, M.; Ren, Z.; Chen, G. Power Factor Enhancement by Modulation Doping in Bulk Nanocomposites. *Nano Lett*. **2011**, *11*, 2225-2230.

(19) Li, H.; Su, X.; Tang, X.; Zhang, Q.; Uher, C.; Snyder, J.; Aydemir, U. Grain Boundary Engineering with Nano-Scale InSb Producing High Performance $In_xCe_yCo_4Sb_{12+z}$ Skutterudite Thermoelectrics. *J. Materiomics* **2017**, *3*, 273-279.

(20) Xiong, Z.; Chen, X.; Huang, X.; Bai, S.; Chen, L. High Thermoelectric Performance of $Yb_{0.26}Co_4Sb_{12}/y$GaSb Nanocomposites Originating from Scattering Electrons of Low Energy. *Acta Materialia* **2010**, *58*, 3995-4002.

(21) Nanobulk Thermoelectrics: Concepts Techniques and Modeling: *Nanoscale Thermoelectrics*; Wang, X.; Wang, Z. M. Ed.; Springer: Heidelberg, **2014**; pp. 141-183.

(22) Liu, H.; Zheng, Z.; Yang, D.; Ke, X.; Jaatinen, E.; Zhao, J-. C.; Zhu, H. Y. Coherent Interfaces between Crystals in Nanocrystal Composites. *ACS Nano* **2010**, *4*, 6219-6227.

(23) Bergman, D. J.; Fel, L. G. Enhancement of Thermoelectric Power Factor in Composite Thermoelectrics. *J. Appl. Phys*. **1999**, *85*, 8205-8216.

(24) Bergman, D. J.; Levy, O. Thermoelectric Properties of a Composite Medium. *J. Appl. Phys*. **1991**, *70*, 6821-6833.

(25) Brochin, F.; Lenoir, B.; Devaux, X.; Martin-Lopez, R.; Scherrer, H. Preparation and Transport Properties of Polycrystalline Bi and Bi-$SiO_2$ Nanocomposites. *J. Appl. Phys*. **2000**, *88*, 3269-3275.

(26) Girard, S. N.; He, J.; Li, C.; Moses, S.; Wang, G.; Uher, C.; Dravid, V. P.; Kanatzidis, M. G. In Situ Nanostructure Generation and Evolution within a Bulk Thermoelectric Material to Reduce Lattice Thermal Conductivity. *Nano Lett*. **2010**, *10*, 2825-2831.

(27) Biswas, K.; He, J.; Zhang, Q.; Wang, Q.; Wang, G.; Uher, C.; Dravid, V. P.; Kanatzidis, M. G. Strained Endotaxial Nanostructures with High Thermoelectric Figure of Merit. *Nat. Chem*. **2011**, *3*, 160-166.

(28) Poudeu, P. F. P.; Angelo, J. D.; Downey, A. D.; Short, J. L.; Hogan, T. P.; Kanatzidis, M. G. High Thermoelectric Figure of Merit and Nanostructuring in Bulk *p*-type $Na_{1-x}Pb_mSb_yTe_{m+2}$. *Angew. Chem. Int. Ed*. **2006**, *45*, 3835-3839.

(29) Zhou, W.; Dwivedi, P.; Shijimaya, C.; Ito, M.; Higashimine, K.; Nakada, T.; Takahashi, M.; Mott, D.; Miyata, M.; Ohta, M.; Miwa, H.; Akatsuka, T.; Maenosono, S. Enhancement of the Thermoelectric Figure of Merit in Blended $Cu_2Sn_{1-x}Zn_xS_3$ Nanobulk Materials. *ACS Appl. Nano Mater.* **2018**, *1*, 4819-4827.

(30) Dwivedi, P.; Miyata, M.; Higashimine, K.; Takahashi, M.; Zhou, W.; Ohta, M.; Maenosono, S. Effect of Gallium Substitution in $Cu_3Al_{1-x}Ga_xSnS_5$ Nanobulk Materials on Thermoelectric Properties. *Appl. Energy Mater*. **2020**, Manuscript ID: ae-2020-007307.

(31) Kumar, A.; Vermeulen, P. A.; Kooi, B. J.; Rao, J.; Eijck, L. V.; Schwarzmüller, S.; Oeckler, O.; Blake, G. R. Phase Transitions of Thermoelectric TAGS-85. *Inorg. Chem*. **2017**, *56*, 15091-15100.

(32) Ali, A.; Ashfaqa, J. A.; Tamseela, M.; Mahmooda, K.; Amina, N.; Hussain, S.; Ahmad, W.; Rehman, U.; Ikram, S.; Al-Othmany, D. S. Modulation of Structural, Optical and Thermoelectric Properties of Sol-Gel Grown CZTS Thin Films by Controlling the Concentration of Zinc. *Ceramics Int*. **2019**, *45*, 12820-12824.

(33) Rodríguez-Carvajal, J. Recent Advances in Magnetic Structure Determination by Neutron Powder Diffraction. *Physica B Condens*. **1993**, *192*, 55-69.

(34) Crystallography Open Database Home Page. http://www.crystallography.net/cod/ (accessed April 11, 2020).

(35) Williamson, G. K.; Hall, W. H. X-ray Line Broadening from Filed Aluminium and Wolfram. *Acta Metall*. **1953**, *1*, 22-31.

(36) He, Y.; Day, T.; Zhang, T.; Liu, H.; Shi, X.; Chen, L.; Snyder, G. J. High Thermoelectric Performance in Non-Toxic Earth-Abundant Copper Sulfide. *Adv. Mater*. **2014**, *26*, 3974-3978.

(37) Suekuni, K.; Tsuruta, K.; Kunii, M.; Nishiate, H.; Nishibori, E.; Maki, S.; Ohta, M.; Yamamoto, A.; Koyano, M. High-performance Thermoelectric Mineral $Cu_{12-x}Ni_xSb_4S_{13}$ Tetrahedrite. *J. Appl. Phys*. **2013**, *113*, 043712-043716.

(38) Suekuni, K.; Kim, F. S.; Nishiate, H.; Ohta, M.; Tanaka, H. I.; Takabatake, T. High-performance Thermoelectric Minerals: Colusites $Cu_{26}V_2M_6S_{32}$ (M = Ge, Sn). *Appl. Phys. Lett*. **2014**, *105*, 132107-132110.

(39) Sun, Y.; Thompson, S. E.; Nishida, T. *Strain Effects in Semiconductors*: *Theory and Applications*; Springer: New York, USA, **2010**; pp 23-50.

(40) Jonnard, P.; Capron, N.; Semond, F.; Massies, J.; Martinez-Guerrero, E.; Mariette. Electronic Structure of Wurtzite and Zinc-blende AlN. *Eur. Phys. J. B* **2004**, *42*, 351-359.

(41) Warnes, L. A. A. Electronic Materials; Springer: Boston, USA, **1990**; pp 84-117.

(42) Zhu, Q.; Hopper, M.; Ingram, B. J.; Mason, T. O. Combined Jonker and Ioffe Analysis of Oxide Conductors and Semiconductors. *J. Am. Ceram. Soc*. **2011**, 94, 187-193.

# Chapter 5

## General Conclusions

## 5.1 Summary

This thesis experimentally studied thermoelectric materials which allow direct conversion between heat and electricity. Through the series of experiments and detailed analysis, the settled objectives for this research could be concluded as achieved. The concluding remarks and the acquired achievements in this research as summarized below:

Beginning with Chapter 1, in the introduction, a brief background of thermoelectric effect has been discussed as an energy conversion technology for utilizing waste heat through the Seebeck effect. This chapter began with the importance of heat in the humankind followed by the outlook of the relationship between conversion efficiency and the dimensionless figure of merit *ZT* of thermoelectric materials has been explained. While, understanding the concept of *ZT* value, we come across a range of material transport characteristics; such as electrical conductivity, mobility, Seebeck coefficient, lattice and carrier thermal conductivity and so on. Then, we landed on the classical strategies to improve the *ZT* values in the thermoelectric materials; which briefly introduced nanostructuring through all-scale hierarchical architechturing, elemental substitution/doping and/or crystal type and phase structuring. Following this, thermoelectric materials classification based on application temperature has been introduced. An exhaustive series of materials have been discussed and understood the rational for exploring the thermoelectric materials derived from relatively earth-ubiquitous and less-toxic constituents. In this mind-churning process, copper sulfide-based semiconductor materials acquired our attention owing to their promising thermoelectric material characteristics. Especially, quaternary copper-zinc-tin-sulfide thermoelectric materials has gained momentum in last one decade; owing to their complex crystal structuring and fairly good Seebeck coefficient but low electrical conductivity. In this research we decided to counter the high lattice thermal conductivity through not only all-scale hierarchical architechuring but also introducing the copper-aluminium-tin-sulfide based material for the first time in thermoelectrics due to predictions of these system to possess very low lattice thermal conductivity. The prediction was true but didn’t throw light on the substantially enhanced electric conductivity leading to higher carrier thermal conductivity. The shortcomings of $Cu_3AlSnS_5$ (CATS) system were answered with the gradual substitution of Al by Ga, and by introducing nanoinclusions of $Cu_2SnS_3$ (CTS). We are the first to investigate the $I_3$-II/III-IV-$VI_{5\text{-}y}$ (I=Cu; II=Zn; III=Al/Ga; IV=Sn; VI=S; $y$ is to maintain electrical neutrality of the system) based materials in thermoelectrics. Various methodologies available for the nanocrystals synthesis have been discussed and out of all the one pot chemical method was shortlisted for this research due to their unprecedented control on the reaction reproducibility as well as scalability. As a result, copper-aluminium-tin-sulfide based nanobulk thermoelectric materials have been fabricated in this dissertation.

In Chapter 2, a series of nanocrystals were synthesized. Beginning from copper-zinc-tin-sulfur system with gradual replacement of Zn with Al using one-pot chemical methodology. The resulting nanocrystals of $Cu_3Zn_{1-x}Al_xSnS_{5-y}$ ($x$ = 0, 0.25, 0.5 and 1) were utilized for the further study. The ligand exchange was necessary to be performed for eliminating very surface long chain organics on the nanocrystals. The ligand exchange with relatively smaller entity. The absence of ligand exchange process may cause impact on the electrical transport characteristics. Thereafter, pulse electric current sintering technique was applied for the densification process to result the nanobulk materials, utilized for thermoelectric property determination.

All the pellets were found to exhibit *p*-type semiconductor behavior. Interestingly, the newer CZTS *i.e.* with composition of $Cu_3Zn_{1-x}Al_xSnS_{5-y}$ ($x$ = 0) exhibits the $ZT$ value at least 15× higher than the pristine nanostructured conventional $Cu_2ZnSnS_4$. Complete substitution of Zn by Al resulted

CATS; which possess at least quarter of the lattice thermal conductivity and enhanced electrical conductivity by an order. On one hand, the high electrical conductivity contributed towards quite good power factor; while the enhancement in carrier thermal conductivity leads to the modest *ZT* value of 0.12 at 668 K, still about 5× higher than neat $Cu_2ZnSnS_4$. If it is possible to reduce the carrier thermal conductivity of CATS while maintaining its relatively high power factor and ultra-low lattice thermal conductivity values by tuning the carrier concentration, CATS deserves to be revisited as a promising sustainable TE material.

An attempt of reducing the carrier thermal conductivity has been performed in the Chapter 3. The Al in CATS was gradually substituted with the Ga to result $Cu_3Al_{1-x}Ga_xSnS_5$ ($x = 0$, 0.25, 0.5, 0.75 and 1). It was found that the increase in Ga content leads to reduction in the charge carrier concentration yielding lower carrier thermal conductivity. However, reduction in charge carrier concentration accompanied with low electrical conductivity but enhanced in Seebeck coefficient. Interestingly, the content of more-ordered crystalline phase content (zinc blende; ZB) was found to be an important parameter showing strong positive correlation with the *ZT* value trend. The more ordered ZB phase content contribute positively towards enhanced charge mobility. At $x = 0.5$, the nanobulk thermoelectric material, $Cu_3Al_{0.5}Ga_{0.5}SnS_5$ exhibit *ZT* value 2× higher than neat CATS system *i.e.* 0.26 at 655 K.

The Chapter 4 explores the ability of nanoinclusions for reducing the electrical conductivity; while efficiently reducing/maintaining the lattice thermal conductivity in the given system. Furthermore, captivatingly, the strong trend between the increase in the ordered crystalline phase content leading to increment in the *ZT* value. It would be interesting to behavior of correlation between crystalline phase type, content with the material transport characteristics. CTS was selected as nanoinclusions owing to the similar lattice characteristics, well-defined particle morphology and comparable particle size. Nanobulk thermoelectric materials fabricated using 1wt%, 3wt%, 5wt% and 10wt% CTS in CATS nanocrystals. The addition of CTS leads to substantially low electrical conductivity leading to suppress the net thermal conductivity. On the structural aspects, the CTS addition, 1 wt% onwards, gradually developed the lattice strain in the system with the formation of less ordered crystalline phase (WZ) in dominant. In other words, it was observed highly strained system yielded lower *ZT* value composed of less-ordered crystalline phase. The observed behavior can be attributed to electron-phonon interaction along the interfaces between grains and inclusions. CTS nanoinclusions, 1 wt% onwards, gradually increases the less ordered (WZ) crystal phase content in the nanobulk materials and leads to the formation of semiconductor material with WZ as major phase. The increase in CTS as nanoinclusions was found to contribute towards greater lattice strain. It was found that CTS nanoinclusions have suppressed the electrical conductivity substantially leading to significant reduction in carrier thermal conductivity; on the other hand, lattice thermal conductivity was largely maintained or further curtailed. Pellets consisting 1wt% onwards CTS nanoinclusions overly curbed electrical conductivity and despite the reduction in thermal conductivity and increment in Seebeck coefficient, the *ZT* value could not be enhanced. However, at 0.1 wt% CTS nanoinclusions a better trade-off between electrical conductivity and Seebeck coefficient was achieved without compromising thermal conductivity and thus improved the *ZT* value 3x than neat CATS system. The 0.1 wt% CTS containing sample possess greater ZB phase content than any other pellets under consideration and prevail the importance of symmetric crystal structure content in deciding the fate of TE properties.

Nevertheless, the attributes driving the phase transformation in nanoinclusions systems towards less/more-ordered crystalline phase and the precise mechanistic details of electron-phonon interaction is yet not clear and needed to be investigated.

The results highlight the importance of co-ordination between the material crystalline structural traits and *ZT* value of $I_3$-III-IV-$VI_5$ based thermoelectric materials without using rare and/or highly toxic elements. This research provides an import insight in understanding the behavior of ZB-/WZ-rich nanobulk thermoelectric materials. The correlation observed among material structural traits it was observed that the apart from nanostructuring, the greater content of more-ordered crystalline phase plays an important in regulating the transport characteristics.

## 5.2 Future Prospects

This dissertation provides some interesting dimensions for extending the research for further increment in the figure of merit. On the basis of research work concluded in Chapter 2, $Cu_3Zn_{1-x}Al_xSnS_{5-y}$ ($x$ = 0, 0.25, 0.5, 0.75 and 1) nanocrystals were successfully synthesized and fabricated to nanobulk thermoelectric materials. In this chapter, it was realized that it would be interesting to investigate the effect of complete extremes of crystalline phases type on the thermoelectric properties for samples at $x = 0$ and $x = 1$. The further enhancement in the *ZT* value can be attempted through optimization of the charge carrier concentration by varying the ratio of Cu:M (M=Zn/Al/Ga) in the nanobulk materials fabrication. Furthermore, it is believed that $Cu_3Al_{1-x}Ga_xSnS_5$ still needs to be optimized in terms of precise Ga content as well as particle size to counterbalance the thermal and electrical transport properties to yield high *ZT* value.

The concept of nanoinclusions is very captivating and needs to optimize the size of the nanoinclusion material, mixing methodology and sintering conditions to yield the favored crystalline phase for enhancing the *ZT* value. In current research, the first glance of the results directs that the nanoinclusion results a dominance of wurtzite phase affecting the *ZT* value negatively. The multiphase material results interface between the phases and thereby it is challenging but interesting that whether the wurtzite phase content only or the interface between zincblende/wurtzite-prevails as stronger factor in controlling *ZT* value.

# Achievements

# Publications

1. **Dwivedi, P.**; Miyata, M.; Higashimine, K.; Takahashi, M.; Zhou, W.; Ohta, M.; Maenosono, S. Effect of Gallium Substitution in $Cu_3Al_{1-x}Ga_xSnS_5$ Nanobulk Materials on Thermoelectric Properties. *Appl. Energy Mater*. **2020**, *6*, 5784-5791.

2. **Dwivedi, P.**; Miyata, M.; Higashimine, K.; Takahashi, M.; Ohta, M.; Kubota, K.; Takida, H.; Akatsuka, T.; Maenosono, S. Nanobulk Thermoelectric Materials Fabricated from Chemically Synthesized $Cu_3Zn_{1-x}Al_xSnS_{5-y}$ Nanocrystals. *ACS Omega* **2019**, *4*, 16402-16408.

3. Fei, S.; Miyata, M.; Takahashi, M.; **Dwivedi, P.**; Zhou, W.; Ohta, M.; Maenosono, S. Thermoelectric Properties of Paracostibite Fabricated using Chemically Synthesized Co-Sb-S Nanoparticles as Building Blocks. *Appl. Phys. Lett*. **2020**, Submitted.

4. Singh, M.; **Dwivedi, P.**; Mott, D.; Higashimine, K.; Ohta, M.; Miwa, H.; Akatsuka, T.; Maenosono, S. Colloid Chemical Approach for Fabricating Cu-Fe-S Nanobulk Thermoelectric Materials by Blending $Cu_2S$ and FeS Nanoparticles as Building Blocks. *Ind. Eng. Chem. Res*. **2019**, *58*, 3688-3697.

5. Nakada, T.; Takahashi, M.; Shijimaya, C.; Higashimine, K.; Zhou, W.; **Dwivedi, P.**; Ohta, M.; Takida, H.; Akatsuka, T.; Miyata, M.; Maenosono, S. Gram-Scale Synthesis of Tetrahedrite Nanoparticles and Their Thermoelectric Properties. *Langmuir* **2019**, *35*, 16335-16340.

6. Zhou, W.; **Dwivedi, P.**; Shijimaya, C.; Ito, M.; Higashimine, K.; Nakada, T.; Takahashi, M.; Mott, D.; Miyata, M.; Ohta, M.; Miwa, H.; Akatsuka, T.; Maenosono, S. Enhancement of the Thermoelectric Figure of Merit in Blended $Cu_2Sn_{1-x}Zn_xS_3$ Nanobulk Materials. *ACS Appl. Nano Mater.* **2018**, *1*, 4819-4827.

## Conference Presentations

1. **Dwivedi, P.**; Miyata, M.; Higashimine, K.; Takahashi, M.; Zhou, W.; Ohta, M.; Maenosono, S. “Nanostructured Thermoelectric Materials Fabricated from Chemically Synthesized I-III-IV-VI Quaternary Compound Nanocrystals” Virtual Conference on Thermoelectrics (VCT 2020), July 21-23, 2020.
2. **Dwivedi, P.**; Miyata, M.; Higashimine, K.; Takahashi, M.; Ohta, M.; Kubota, K.; Takida, H.; Akatsuka, T.; Maenosono, S. "$Cu_3AlSnS_5$ Based Thermoelectric Materials with $Cu_2SnS_3$ Nanoinclusions" 日本化学会第100春季年会, 22-25 March 2020, 東京理科大学, 野田, 千葉.
3. **Dwivedi, P.**; Zhou, W.; Ohta, M.; Miyata, M.; Takida, H.; Kubota, K.; Akatsuka, T.; Maenosono, S. "Synthesis of $Cu_3Al_{1-x}M_xSnS_5$ (M = Metal) Nanocrystals as Building Blocks for Sustainable Thermoelectric Materials" 第70回コロイドおよび界面化学討論会 (Okinawa Colloids 2019), 3-8 November 2019, Bankoku Shinryokan, Nago, Okinawa.
4. **Dwivedi, P.**; Zhou, W.; Ohta, M.; Miyata, M.; Takida, H.; Akatsuka, T.; Maenosono, S. "Nanobulk Thermoelectric Materials Fabricated from Chemically Synthesized $Cu_3Al_{1-x}Zn_xSnS_5$ Nanocrystals" 38th Annual International Conference on Thermoelectrics and 4th Asian Conference on Thermoelectrics (ICT/ACT2019), 30 June - 4 July 2019, Hwabaek International Convention Center, Gyeongju, South Korea.
5. **Dwivedi, P.**; Zhou, W.; Ohta, M.; Miyata, M.; Miwa, H.; Akatsuka, T.; Maenosono, S. "Chemical Synthesis of Cu-Al-Sn-S Nanocrystals toward Sustainable Thermoelectric Materials" 日本化学会第99春季年会, 16-19 March 2019, 甲南大学, 神戸, 兵庫.
6. **Dwivedi, P.**; Zhou, W.; Ohta, M.; Miyata, M.; Miwa, H.; Akatsuka, T.; Maenosono, S. "Nanobulk Thermoelectric Materials Composed of Chemically-Synthesized Cu-Al-Sn-S

Nanocrystals" 第15回日本熱電学会学術講演会, 13-15 September 2018, 東北大学, 仙台, 宮城.

7. Fei, S.; **Dwivedi, P.** 太田 道広, 赤塚 威夫, 宮田 全展, 前之園 信也 "Co-Sb-S系N型熱電ナノ粒子の化学合成と評価" 令和1年度北陸地区講演会と研究発表会, 29 November 2019, 金沢大学角間キャンパス, 石川.
8. 沼野 公佑, Singh, M. 中田 豪, **Dwivedi, P.** 太田 道広, 瀧田 大, 赤塚 威夫, 前之園 信也" サステイナブル熱電材料創製に向けたCu-Fe-S系ナノ粒子の化学合成と評価"令和1年度北陸地区講演会と研究発表会, 29 November 2019, 金沢大学角間キャンパス, 石川.
9. Fei, S.; **Dwivedi, P.**; Miyata, M.; Ohta, M.; Akatsuka, T.; Maenosono, S. "Chemical Synthesis of Co-Sb-S Nanoparticles and Fabrication of Nanostructured N-type CoSbS Thermoelectric Materials" 第70回コロイドおよび界面化学討論会 (Okinawa Colloids 2019), 3-8 November 2019, Bankoku Shinryokan, Nago, Okinawa.
10. Numano, K.; Singh, M.; **Dwivedi, P.**; Ohta, M.; Takida, H.; Akatsuka, T.; Maenosono, S. "Chemical Synthesis of Cu−Fe−S Nanoparticles towards Sustainable N-type Thermoelectric Materials" 第70回コロイドおよび界面化学討論会 (Okinawa Colloids 2019), 3-8 November 2019, Bankoku Shinryokan, Nago, Okinawa.
11. Zhou, W.; **Dwivedi, P.**; Higashimine, K.; Miyata, M.; Ohta, M.; Takida, H.; Akatsuka, T.; Maenosono, S. "Structure-Property Relations in Thermoelectric Nanobulk Materials Fabricated from $Cu_2SnS_3$ Nanoparticles" 38th Annual International Conference on Thermoelectrics and 4th Asian Conference on Thermoelectrics (ICT/ACT2019), 30 June - 4 July 2019, Hwabaek International Convention Center, Gyeongju, South Korea.

12. 沼野 公佑, Singh, M. 中田 豪, **Dwivedi, P.** 太田 道広, 三輪 大, 赤塚 威夫, 前之園 信也 "サステイナブル熱電材料創製に向けたCu-Fe-S系ナノ粒子の化学合成と評価"日本化学会第99春季年会, 16-19 March 2019, 甲南大学, 神戸, 兵庫.
13. 費 舒杰, 中田 豪, 周 薇, **Dwivedi, P.** 太田 道広, 赤塚 威夫, 前之園 信也"Co-Sb-S熱電ナノ粒子の化学合成と構造解析"日本化学会第99春季年会, 16-19 March 2019, 甲南大学, 神戸, 兵庫.
14. Nakada, T.; Shijimaya, C.; Higashimine, K.; Takahashi, M.; Zhou, W.; **Dwivedi, P.**; Ohta, M.; Miwa, H.; Akatsuka, T.; Miyata, M.; Maenosono, S. "Sustainable Thermoelectric Materials Fabricated by using Chemically-Synthesized Tetrahedrite Nanoparticles as Building Blocks" 日本化学会第99春季年会, 16-19 March 2019, 甲南大学, 神戸, 兵庫.
15. Zhou, W.; **Dwivedi, P.**; Higashimine, K.; Miyata, M.; Ohta, M.; Miwa, H.; Akatsuka, T.; Maenosono, S. "Structure-Property Relations in Thermoelectric Nanobulk Materials Fabricated from $Cu_2Sn_{1-x}Zn_xS_3$ Nanoparticles" 日本化学会第99春季年会, 16-19 March 2019, 甲南大学, 神戸, 兵庫.
16. Zhou, W.; **Dwivedi, P.**; Shijimaya, C.; Ito, M.; Higashimine, K.; Nakada, T.; Takahashi, M.; Mott, D.; Miyata, M.; Ohta, M.; Miwa, H.; Akatsuka, T.; Maenosono, S. "Improvement of Thermoelectric Performance of $Cu_2Sn_{1-x}Zn_xS_3$ Nanobulk Materials Fabricated by a Bottom-up Approach" 第69回コロイドおよび界面化学討論会, 18-20 September 2018, 筑波大学, つくば, 茨城.
17. Zhou, W.; **Dwivedi, P.**; Shijimaya, C.; Ito, M.; Higashimine, K.; Nakada, T.; Takahashi, M.; Mott, D.; Miyata, M.; Ohta, M.; Miwa, H.; Akatsuka, T.; Maenosono, S. "Enhancement of

Thermoelectric Figure of Merit in Blended $Cu_2Sn_{1-x}Zn_xS_3$ Nanobulk Materials" 第15回日本熱電学会学術講演会, 13-15 September 2018, 東北大学, 仙台, 宮城.

18. 中田 豪, 四十万谷 智子, 東嶺 孝一, 高橋 麻里, 周 薇, **Dwivedi, P.**; Mott, M.; 太田 道広, 赤塚 威夫,三輪 大, 小野 博信, 宮田 全展, 前之園 信也" サステイナブル熱電変換材料に向けたテトラヘドライトナノ粒子の合成と評価" 第15回日本熱電学会学術講演会, 13-15 September 2018, 東北大学, 仙台, 宮城
19. Zhou, W.; Shijimaya, C.; **Dwivedi, P.**; Nakada, T.; Takahashi, M.; Mott, D.; Koyano, M.; Ohta, M.; Miwa, H.; Akatsuka, T.; Ono, H.; Maenosono, S. "Thermoelectric Properties of Mixed Phase $Cu_2Sn_{1-x}Zn_xS_3$ Heterostructured Nanoparticle Material" Asian Symposium on Nanoscience and Nanotechnology 2018, 12-14 May 2018, Takeda Building, The University of Tokyo, Tokyo.
20. Zhou, W.; Shijimaya, C.; **Dwivedi, P.**; Nakada, T.; Takahashi, M.; Mott, D.; Koyano, M.; Ohta, M.; Miwa, H.; Akatsuka, T.; Ono, H.; Maenosono, S. "Nanostructured Thermoelectric Material Composed of Heterogeneous $Cu_2Sn_{1-x}Zn_xS_3$ Nanoparticles" ナノ学会第 16回大会, 10-12 May 2018, 東京大学武田先端知ビル, 東京.

## Patent

1. "熱電変換材料用粉体、熱電変換材料、及び熱電変換材料の製造方法", 赤塚 威夫, 久保田 是史, 三輪 大, 前之園 信也, 小矢野 幹夫, 周 薇, マニンダ シン, **ドウィヴェディ プラティバ**, 特開2020-010010.